https://ntrs.nasa.gov/search.jsp?R=19650023904 2020-03-17T01:24:37+00:00Z

Final Report
T-82028-6

Technical Report

THE EFFECT OF NUCLEATION OF SURFACE SLIP ON THE FLOW AND FRACTURE OF BERYLLIUM

GPO PRICE $ _____

CSFTI PRICE(S) $ _____

Hard copy (HC) _____

Microfiche (MF) _____

ff 653 July 65

by

A. Lawley
J. F. Breedis
K. U. Snowden

July 1965

Prepared for

NATIONAL AERONAUTICS AND SPACE ADMINISTRATION

Contract No. NASr-145

N65-33505
ACCESSION NUMBER

PAGES

CODE

NASA CR OR TMX OR AD NUMBER

17
CATEGORY

THE FRANKLIN INSTITUTE RESEARCH LABORATORIES
BENJAMIN FRANKLIN PARKWAY AT 20TH STREET, PHILA. 3, PA.

Final Report
F-B2028-1

Technical Report

THE EFFECT OF NUCLEATION OF SURFACE SLIP ON THE FLOW AND FRACTURE OF BERYLLIUM

A. Lawley
J. F. Breedis
K. U. Snowden

July 1965

Prepared for

NATIONAL AERONAUTICS AND SPACE ADMINISTRATION

Contract No. NASr-145

THE FRANKLIN INSTITUTE RESEARCH LABORATORIES

BENJAMIN FRANKLIN PARKWAY AT 20TH STREET, PHILA. 3, PA.

FOREWORD

This report covers research conducted for the National Aeronautics and Space Administration under Contract NASr-145. The report consists of three main areas of research activity namely: (i) fatigue studies of single crystal beryllium (ii) microstrain behavior of single crystal beryllium (iii) effect of thermal-mechanical and surface treatments on the flow and fracture of beryllium. Dr. A. Lawley and Dr. J. F. Breedis were responsible for the fatigue and microstrain studies, while Dr. K.U. Snowden directed the studies on thermal-mechanical and surface effects. F. Wilhelm, J. A. Zeiger, and W. D. Hepfer assisted at various periods of time throughout the investigation.

Alan Lawley

Alan Lawley, Manager
Physical Metallurgy

Approved by:

H. Conrad
Technical Director

J.R. Feldmeier
Director of Laboratories

TABLE OF CONTENTS

FOREWORD i

SECTION I - FATIGUE STUDIES OF SINGLE CRYSTAL BERYLLIUM

ABSTRACT 1

I. INTRODUCTION 2

II. EXPERIMENTAL PROCEDURE 3

III. EXPERIMENTAL RESULTS 7

IV. DISCUSSION AND SUMMARY 28

REFERENCES 33

SECTION II - THE MICROSTRAIN BEHAVIOR OF SINGLE CRYSTAL BERYLLIUM

ABSTRACT 35

I. INTRODUCTION 36

II. EXPERIMENTAL PROCEDURE 38

III. RESULTS 41

IV. DISCUSSION 54

V. SUMMARY 58

REFERENCES 59

SECTION III - THE EFFECT OF THERMAL, MECHANICAL, AND SURFACE TREATMENTS ON THE FLOW AND FRACTURE OF BERYLLIUM

ABSTRACT 61

I. INTRODUCTION 62

II. EXPERIMENTAL PROCEDURE 63

III. EXPERIMENTAL RESULTS 64

DISCUSSION 84

SUMMARY 86

TABLE OF CONTENTS (CONT.)

REFERENCES. 88

APPENDIX A - GROWTH OF BERYLLIUM SINGLE CRYSTALS. A1

APPENDIX B - PREPARATION OF ELECTRON MICROSCOPE SPECIMENS B1

REFERENCES. B3

APPENDIX C - HIGH RESOLUTION DARK FIELD MICROSCOPY USING A PHILIPS 100B ELECTRON MICROSCOPE C1

ABSTRACT. C1

INTRODUCTION. C1

CONSTRUCTION. C2

OPERATION C5

REFERENCE C7

APPENDIX D - THE EFFECT OF CONCURRENT AND INDEPENDENT YIELDING MECHANISMS ON ANELASTIC BEHAVIOR D1

LIST OF FIGURES

Fig. No.		Page
1-1	The Geometry and Dimensions of the Beryllium Single Crystal Specimens (a) bend fatigue (b) compression fatigue (c) tensile fatigue.	4
1-2	(a) Optical Micrograph of the Slip Band Structure at the Surface of the Bend Fatigue Crystal near the Grip. Basal Slip Orientation x200. (b) Surface Replica from Region Close to Grip.	8
1-3	Persistent Markings of Closely Spaced Pits Parallel to the Trace of the (0001) Plane. S is the direction of shadowing. $\sim 6\mu$ Electropolished from the Outer Bend Surface.	9
1-4	Dislocation Substructure Close to the Bend Surface in a Crystal Oriented for Basal Slip in Bend Fatigue. Plane of Foil is $(\bar{2}113)$.	10
1-5	Light and Dark Field Micrographs of the Dislocation Substructure Following Axial Compression Fatigue. Crystal Oriented for Basal Slip. Foil Plane is (0001) in a, b, c, and (0110) in d. Operative Reflections are: $11\bar{2}0$, $\bar{1}100$, $10\bar{1}0$, $\bar{2}110$, in a, b, c, d, respectively	13
1-6	Optical Micrographs of the Surface Slip Structure in Bend Fatigue-Prism Slip Orientation. (a) as Fatigued (b) and (c) Fatigued and Electropolished to a depth $\sim 5\mu$. 5×10^6 Cycles at a Resolved Stress of 22,950 psi. All Magnifications X300	16
1-7	Optical Micrographs of the Surface Slip Structure in Bend Fatigue-Prism Slip Orientation. (a) and (b) as Fatigued (c) and (d) Fatigued and Electropolished to a depth $\sim 2\mu$. 3×10^5 Cycles at a Resolved Stress of 8250 psi. Magnifications: (a) X 480 (b) X 480 (c) X 100 (d) X 480.	17
1-8	Replication of Bend Fatigue-Prism Slip Crystal After Removal of $\sim 5\mu$ from Bend Surface. Note that the Rows of Pits Show Dark Contrast Towards the Direction of Shadowing. 5×10^6 Cycles at Resolved Stress of 22,950 psi.	18
1-9	Surface Replica Electron Micrographs Showing Persistent Prism Plane Slip Traces. Crystal Fatigued 3×10^5 Cycles in Simple Bending at a Resolved Stress of 8150 psi, and Electropolished to a Depth $\sim 2\mu$.	19

LIST OF FIGURES (CONTD.)

Fig. No.		Page
1-10	Dislocation Substructure Close to the Bend (Tension) Surface in a Crystal Oriented for Prism Slip in Bend Fatigue. Plane of Foil is $(\bar{4}\bar{1}50)$. Crystal Given 5×10^6 Cycles at a Resolved Stress of 22,950 psi.	20
1-11	(a) Optical Micrograph Showing Prism and Basal Plane Slip. Axial Tensile Fatigue in Crystal Oriented for prism slip. X300. (b) Corresponding Slip Strucure by Surface Replication.	20
1-12	Dislocation Substructure Following Axial Tensile Fatigue in Crystal Oriented for Prism Slip. (a) Plane of Foil $(0\bar{1}10)$, Operative Reflection $\bar{2}110$. (b) Plane of Foil (0001).	21
1-13	Sequence of Recovery Events in Crystal Originally Deformed in Bend Fatigue. Basal Slip Orientation. Plane of Foil $(\bar{2}113)$, with $[01\bar{1}0]$ the line of intersection of the basal plane with the foil surface.	23
1-14	Recovered Structure in Crystal Originally Deformed in Bend Fatigue - Prism Slip Orientation.	24
1-15	Dislocation Substructure Close to the Bend Surface in a Crystal Oriented for Basal Slip in Bend Fatigue. Plane of Foil is $(\bar{2}113)$. (a) as Fatigued (b) fatigued + 1 hour at 100°C (c) and (d) Fatigued + 1 hour at 300°C. Crystal Annealed in Bulk Condition Prior to Thinning	26
1-16	Dislocation Substructure Close to the Bend (Tension) Surface in a Crystal Oriented for Prism Slip in Bend Fatigue. Plane of Foil is $(\bar{4}\bar{1}50)$. (a) as Fatigued (b) Fatigued + 1 hour at 100°C. (c) Fatigued + 1 hour at 200°C (d) Fatigued + 1 hour at 300°C. Crystals Annealed in Bulk Condition Prior to Thinning	27
2-1	Method of Specimen Gripping and Measurement of Strain	39
2-2	Sets of Closed Hystersis Loops at Pre-strains of 0.0019 and 0.087 Single Crystal Strained in Tension.	42
2-3	Plot of the Irreversible Work Against Forward Plastic Strain, and Stress Amplitude. Crystal Prestrained 0.0146 (shear) in Tension.	44

LIST OF FIGURES (CONTD.)

Fig. No.		Page
2-4	Representative Shear Stress-Shear Strain Curve in Tension. Initial Orientation of Stress Axis Shown in Stereographic Triangle. Experimantally Determined Firction Stress (T_f) is Included for Comparison.	45
2-5	Cyclic Compression of Single Crystal at Constant Strain Amplitude. Numbers Refer to Order of Cycling	47
2-6	Cyclic Work-Hardening Curve and Tensile Curve, Versus Cumulative Glide Strain, for Basal Slip Orientation.	48
2-7	A Set of Closed Hystersis Loops Obtained After a Total Pre-strain of 0.40 (shear) in Cyclic Compression.	50
2-8	Plot of Irreversible Work Against Forward Plastic Strain and Stress Amplitude. Crystal Prestrained 0.40 (shear) in Cyclic Compression	51
2-9	Dislocation Substructure Following Axial Cyclic Compression. Crystal Oriented for Basal Slip (a) Plane of Foil is (0001) with $11\bar{2}0$ the Operative Reflection in Bright-Field. (b) Plane of foil is $(01\bar{1}0)$ with $\bar{2}110$ the Operative Reflection in Dark-Field.	53
3-1	Microstrain jig with specimen in position	65
3-2	Stress-strain behavior in the microstrain region for QMV-N50 beryllium in the conditions indicated	66
3-3	Measurement of the frictional stress σ_f	68
3-4	Effect of specimen condition on the stress and strain at fracture of two batches of hot-pressed QMV-N50, and secondary refined Pechiney beryllium.	71
3-5	Stress-strain curves to fracture for material in conditions indicated	72
3-6	Stress-strain curves to fracture for material in the conditions indicated	73
3-7	Effect of grease coating on the stress-strain curve to fracture	74
3-8	Tensile and cyclic hardening curves for specimens in the annealed condition.	75

LIST OF FIGURES (CONTD.)

Fig. No.		Page
3-9	The fracture surface of the as-received material. X250.	76
3-10	The fracture surface of the material which had been strain cycled prior to testing. X500.	76
3-11	Surface of specimen sprayed with carborundum particles under pressure. X375.	78
3-12	Dislocation configurations in tensile strained as-received beryllium, 40,000: 1	80
3-13	Tensile strained as-received beryllium. Long straight dislocations terminating at a subboundary. Kinked dislocations are arrowed. 40,000: 1	80
3-14	Low angle boundaries (arrowed) and small regions giving rise to contrast effects. Specimen strain-cycled prior to tensile straining. 40,000: 1	81
3-15	Dislocation tangles and dislocation loops (arrowed). Specimen strain-cycled prior to tensile straining. 40,000: 1.	81
3-16	Short isolated dislocations in specimen strain-cycled prior to tensile straining. 40,000: 1	82
3-17	Long parallel dislocation-pairs in annealed and deformed beryllium 40,000: 1	83
3-18	Rows of dislocations making low angle boundaries (arrowed) in annealed beryllium. 40,000: 1.	84
A-1	Schematic Representation of the Apparatus used to Grow Beryllium Single Crystals by the Vertical Floating-Zone Technique.	A2
B-1	Schematic Representation of the Knuth System of Electro-polishing for Beryllium.	B2
C-1	(a) Construction of Brass Former for Tilt Coils. Dimensions in Millimeters. (b) Winding for Vertical or Horizontal Coils.	C3
C-2	Wiring Diagram for Power Supply and Tilt Coils	C4
C-3	Stacking Faults in Stainless steel. (a) Bright Field. (b) Dark Field. Original Magnification x 40,000.	C7
D-1	Schematic Representation of Two Independent Yielding Mechanisms Controlled by Frictional Stress τ_1 and τ_2.	D2

LIST OF TABLES

Table		Page
1-1	CRYSTALLOGRAPHIC CODE FOR FATIGUE CRYSTALS.	5
2-1	SUMMARY OF THE FRICTIONAL STRESS VALUES	46
3-1	THE EFFECT OF SPECIMEN CONDITION ON THE STRESS AND STRAIN AT FRACTURE.	77

SECTION I

FATIGUE STUDIES OF SINGLE CRYSTAL BERYLLIUM

ABSTRACT

33505

Transmission electron microscope studies have been made of the dislocation arrangements in zone-refined Pichiney beryllium oriented for basal or prism slip following fatigue at room temperature. Fatigue modes include (i) reverse bending at 1800 cpm (ii) low frequency (~ 2 cpm) uniaxial tension or compression cycling. The surface slip structure in bend fatigue was examined optically and also by using high resolution silicon monoxide replicas.

A persistent slip structure develops to a depth ~ 6μ in both basal and prism slip orientations and bend fatigue. The persistent markings correspond to closely spaced depressions or pits on the crystal surface and are parallel to (0001) for basal slip, or (0001) and ($0\bar{1}10$) in prism slip. The basal slip bend fatigue substructure is characterized by a high density of prismatic loops elongated in a direction perpendicular to each of the three $a/3 < \bar{2}110 >$ slip vectors; a majority of these loops are elongated perpendicular to the favored $a/3 [\bar{2}110]$ slip vector. The loops have a Burgers vector $1/6 <11\bar{2}3>$ or $1/3 <11\bar{2}0>$ so that they do not contain stacking faults. Axial fatigue gives rise to a relatively uniform dislocation substructure of edge and screw components and prismatic dislocation loops on the operative slip plane.

After prolonged examination in the electron microscope, recovery of the bend fatigue substructure occurs with a significant lowering of the dislocation density. In order to obtain similar effects in foils following axial fatigue, it is necessary to heat the foil in the microscope above 100°C. Annealing experiments (100°C to 300°C for 1 hour periods) on bulk crystals, oriented for basal or prism slip in bend fatigue serve to show that the recovery effects following bend fatigue are restricted to thin foils.

I. INTRODUCTION

The deformation behavior of beryllium under conditions of cyclic loading has been largely neglected. Our current knowledge of fatigue in this material is restricted to a small number of conventional S-N plots for commercial grades. Wallace and Wallace[1] report an endurance limit ~ 31,000 psi for polycrystalline hot pressed and warm extruded material in axial tension-compression. In the temperature range 550°C to 650°C, the hot-pressed and extruded beryllium shows no true endurance limit up to 10^8 cycles (Vickers[2]), and the fractures are intergranular. More recently, Klein et al[3] have obtained improved bend fatigue strength (endurance limit ~ 40,000 psi) in QMV beryllium sheet which was produced by vacuum hot working.

Several studies have been aimed at an understanding of plastic flow in beryllium through direct observation of glide dislocation configurations. These include the examination of both polycrystalline[4,5] and single crystal[4,6] beryllium covering a wide range of purities. No studies of this nature have been reported involving cyclic loading; in fact, only a limited number of electron microscope observations have been made on fatigued hexagonal close-packed metals, and these refer to magnesium[7] and zinc[8]. In these instances, the deformation structure is similar to that of the face-centered cubic metals copper and nickel[9] following fatigue. Dense bundles of elongated edge dipoles are observed in the active slip plane with a direction of elongation $\langle 10\bar{1}0 \rangle$ normal to the Burgers vector. There is a relative absence of dislocations having a large screw component, and the dislocation density between bundles is extremely low.

In the present investigation high purity single crystals of beryllium, oriented for basal or prism plane slip, have been plastically deformed under conditions of bending and axial fatigue. The associated dislocation configurations and surface slip structures are compared with those reported by Damiano and Herman[6] for material of comparable purity deformed in simple tension. Recovery behavior of the fatigue structure has been examined in both thin foils and bulk material.

II. EXPERIMENTAL PROCEDURE

a. Specimen Preparation: Single crystals of beryllium were grown from 0.5" dia. Pechiney secondary refined vacuum-cast and extruded stock using the floating zone melting technique developed by Spangler et al[10]. Crystals received three zone passes, and specific orientations were obtained by seeding. All the necessary shaping operations were performed by low energy, spark discharge machining. Prior to fatigue testing, specimens were given a final electropolish in a solution of 50 parts ethylene glycol, 5 parts concentrated nitric acid, 1 part concentrated sulphuric acid, and 1 part concentrated hydrochloric acid, using a potential of 15 volts. The geometry and dimensions of the specimens are illustrated in Figure 1-1. For compression fatigue, the specimens were cylinders of height 0.58" and diameter 0.30". The crystallographic code for the Planes A and B, and the angle Φ is given in Table 1-1. The shape of the bend fatigue specimen is such that the bending stress is approximately constant along the length of the crystal.

b. Fatigue Testing: Bend fatigue tests were made in a Sonntag SF-2-U machine at 1800 cpm. Crystals oriented for basal slip were subjected to reverse bending about a mean zero stress so that the upper and lower surfaces (Figure 1-1a) were alternately in tension and compression. For the prism slip orientation, compressive stresses lead to twinning on $\{10\bar{1}2\}$ planes. Accordingly, the crystals were fatigued in simple bending whereby the upper surface is subjected to only cyclic tensile stress, and the lower surface to only cyclic compressive stress. For the two crystal orientations studied, the load was increased incrementally to a level at which the resolved shear stress on the basal or prism slip system at the bend surface exceeded the stress required for plastic flow. These critical resolved shear stresses (in tension) are $\sim$ 860 psi and $\sim$ 7900 psi for basal and prism slip respectively. As a guide to the behavior of single crystal beryllium in cyclic bending, crystals of each orientation were subjected to $\sim 5 \times 10^6$ cycles without fracture at a resolved shear stress level approximately three times that required for basal or prism slip.

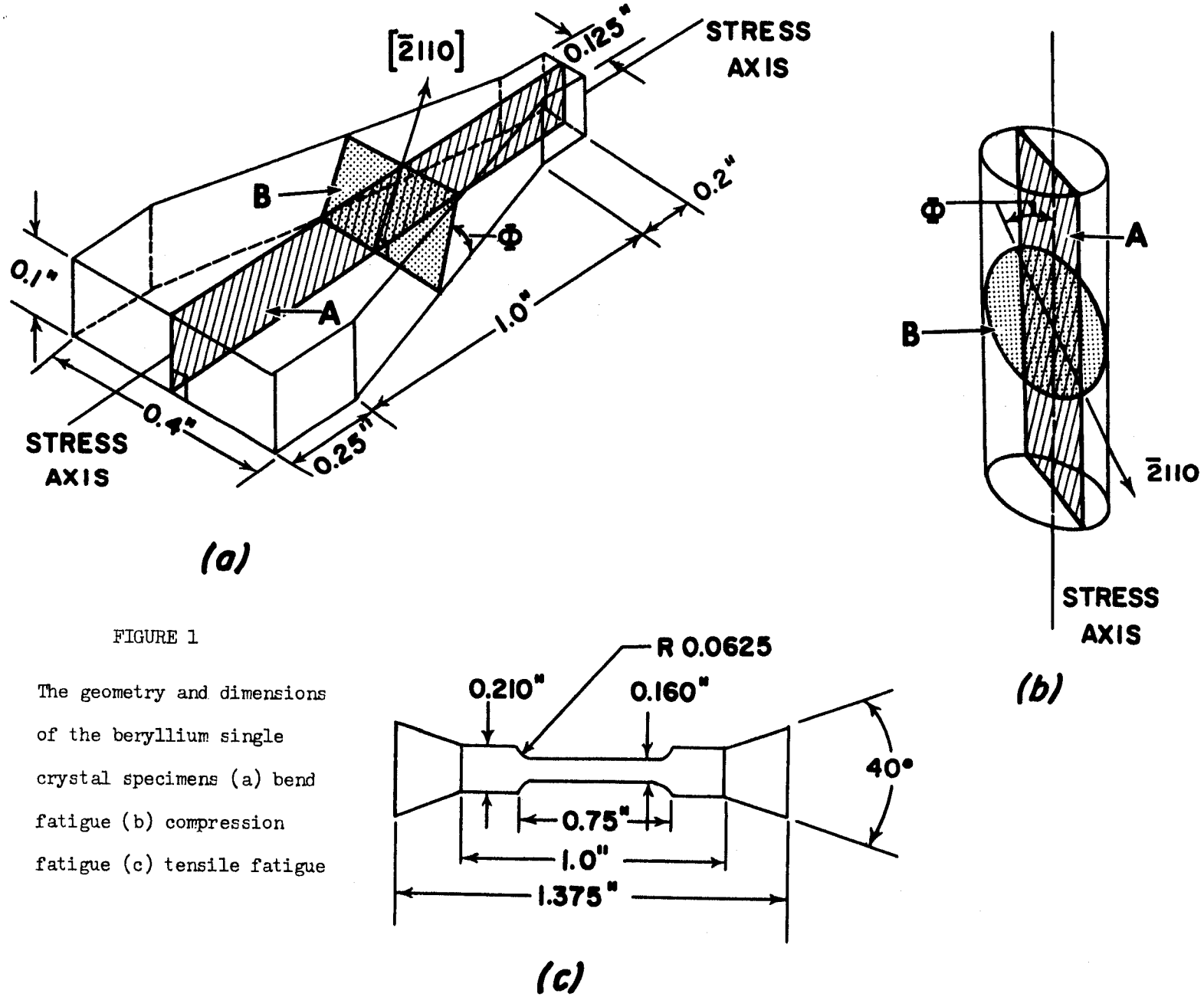

FIGURE 1

The geometry and dimensions of the beryllium single crystal specimens (a) bend fatigue (b) compression fatigue (c) tensile fatigue

Fig. 1-1 - The Geometry and Dimensions of the Beryllium Single Crystal Specimens (a) bend fatigue (b) compression fatigue (c) tensile fatigue.

Table 1-1

CRYSTALLOGRAPHIC CODE FOR FATIGUE CRYSTALS

Fatigue Mode	Plane Code (A)	Plane Code (B)	ϕ	Favored Slip System
Reverse Bend	$(0\bar{1}10)$	(0001)	43°	(0001) 1/3 $[\bar{2}110]$
Simple Bend	(0001)	$(0\bar{1}10)$	48°	$(0\bar{1}10)$ 1/3 $[\bar{2}110]$
Cyclic Compression	$(0\bar{1}10)$	(0001)	70°	(0001) 1/3 $[\bar{2}110]$
Cyclic Tension	(0001)	$(0\bar{1}10)$	48°	$(0\bar{1}10)$ 1/3 $[\bar{2}110]$

Low frequency ($\sim$ 2 cpm) tensile and compressive axial fatigue tests were made in a straining jig located between the fixed and moving crosshead of a standard Instron machine. Details of the complete assembly are described elsewhere[11]. It should be emphasized that the jig was designed for studies of the microplastic strain region in materials ($\Delta\ell/\ell \simeq 10^{-6}$), so that extremely accurate alignment of the specimen axis and stress axis is possible. The compression and tension fatigue damage was induced under conditions of constant strain amplitude at the macroscopic yield stress. In both compression and tension fatigue, the resolved glide strain on the basal and prism slip systems, respectively was 0.0015 per cycle for a total of 45 cycles.

c. Electron Microscopy: Initially, the fatigued crystals were examined under the light microscope for slip lines. High resolution replicas were then prepared from the original as-fatigued bend surface or after electropolishing to a controlled depth using the method of Grube and Rouze[12]. A water soluble agent, Victawet 35B, is first evaporated onto the beryllium surface followed by evaporation of SiO. In this way the replicas can be removed from the surface by immersion in distilled water. Replicas were shadowed with tungsten oxide prior to examination in the electron microscope.

Thin foils suitable for transmission electron microscopy were prepared from slices of selected orientation using the jet polishing technique

followed by a final electropolish in the ethylene glycol-acid solution. The slices were cut from the bulk crystal using the low energy, spark discharge method. The foils were examined in transmission in a Philips 100B electron microscope operating at either 80 KV or 100 KV. Selected area electron diffraction was used to index directions in the plain of the foil; as a further check on orientation, a standard back reflection x-ray Laue photograph was taken with the foil in the microscope holder, prior to examination in the microscope. Burgers vectors were studied using specific diffraction contrast conditions.

III. EXPERIMENTAL RESULTS

The experimental observations are conveniently summarized under three groupings, namely (a) the basal slip condition in bend and axial fatigue (b) the prism slip condition in bend and axial fatigue (c) recovery of the fatigue substructure.

a. Crystals Oriented for Basal Slip

Bend Fatigue Observations: Consideration is given first to the crystals of basal slip orientation fatigued in the reverse bend mode. A representative light micrograph and electron micrograph of the replicated as-fatigued surface are illustrated in Figure 1-2. Geometrically, the surface of observation in both the micrographs corresponds to the point of emergence of edge dislocations having a Burgers vector $\frac{1}{3}[\bar{2}110]$ (refer to Figure 1-1). Thus, the slip traces are parallel to $[01\bar{1}0]$ which is the line of intersection of the basal plane and the surface of observation. Slip has occurred over the entire gauge section, and in the central region away from either grip is on a relatively fine scale. In regions adjacent to the grips, deeper slip steps are frequently observed, indicating that stress concentrations exist in these regions. From a detailed examination of the surface replicas, no activity on other systems such as those involving the prism plane was observed.

Further insight into the detail of the slip structure is obtained by electropolishing to controlled depths below the outer bend surface. In Figure 1-3, electron micrographs of the replicated surface are shown after removal of $\sim 6\mu$ layer from the bend surface; this crystal was given 2×10^6 cycles at a stress of 3460 psi. From the known direction of shadowing of the replicas, the rows of persistent markings are found to correspond to closely spaced depressions or pits on the crystal surface, parallel to the trace of the (0001) slip plane. After this examination, a further 4μ was removed from the bend surface, at which depth there was no evidence of any persistent slip structure.

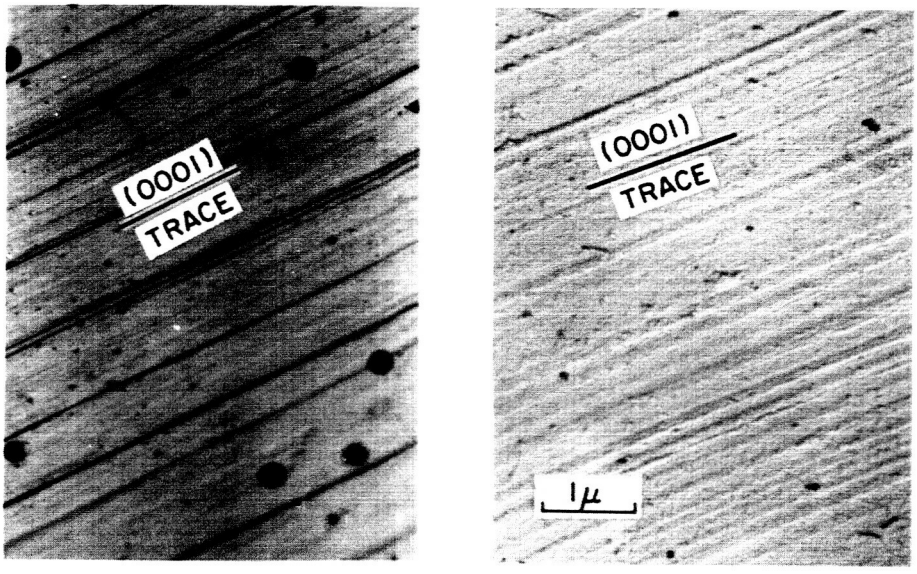

(a) (b)

Fig. 1-2 - (a) Optical Micrograph of the Slip Band Structure at the Surface of the Bend Fatigue Crystal near the Grip. Basal Slip Orientation. X200.
(b) Surface Replica from Region Close to Grip.

Preparation of transmission foils by the jet polishing technique allows for observation at varying depths below the surface of maximum bending stress. In this way, it was determined that the bend fatigue damage is confined to a depth <50μ from the outer surface. Distinct differences exist in the dislocation substructure from region to region. The configurations in Figure 1-4 summarize these variations. In each of the micrographs, the plane of the foil is very nearly $(\bar{2}113)$ with the basal plane at an inclination of 43° from the foil plane. By the use of selected diffraction contrast conditions, it was established that many of the dislocations visible in Figure 1-4a do not belong to the preferred $(0001)\ \frac{1}{3}\ [\bar{2}110]$ slip system. Specifically, strong contrast conditions exist using the $[01\bar{1}0]$ reflection, a reflection for which (g.b)s is zero when the Burgers vector is $\frac{1}{3}\ [\bar{2}110]$.

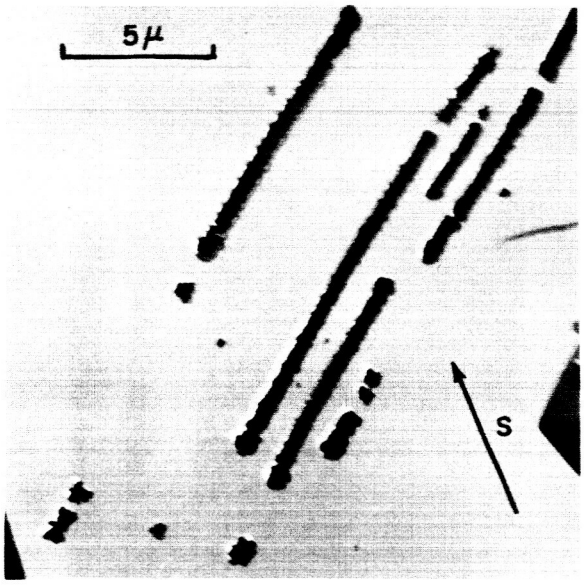

(a)

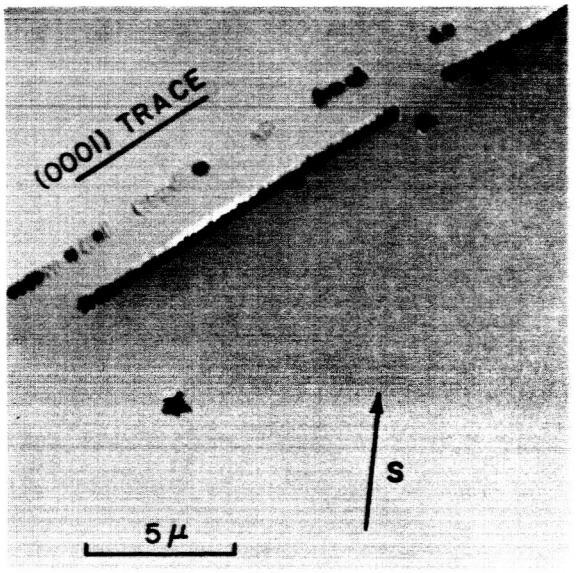

(b)

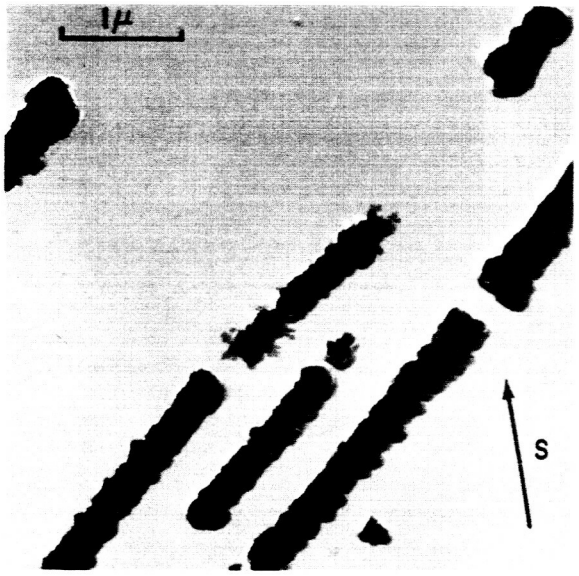

(c)

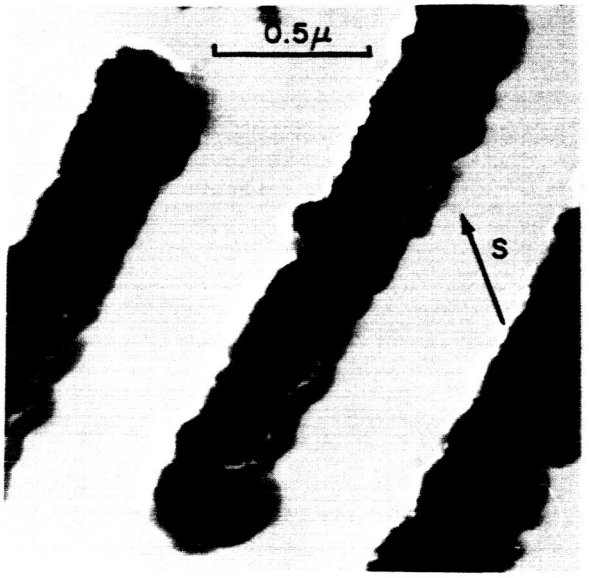

(d)

Fig. 1-3 - Persistent Markings of Closely Spaced Pits Parallel to the Trace of the (0001) Plane. S is the direction of shadowing. ~ 6μ Electropolished from the Outer Bend Surface.

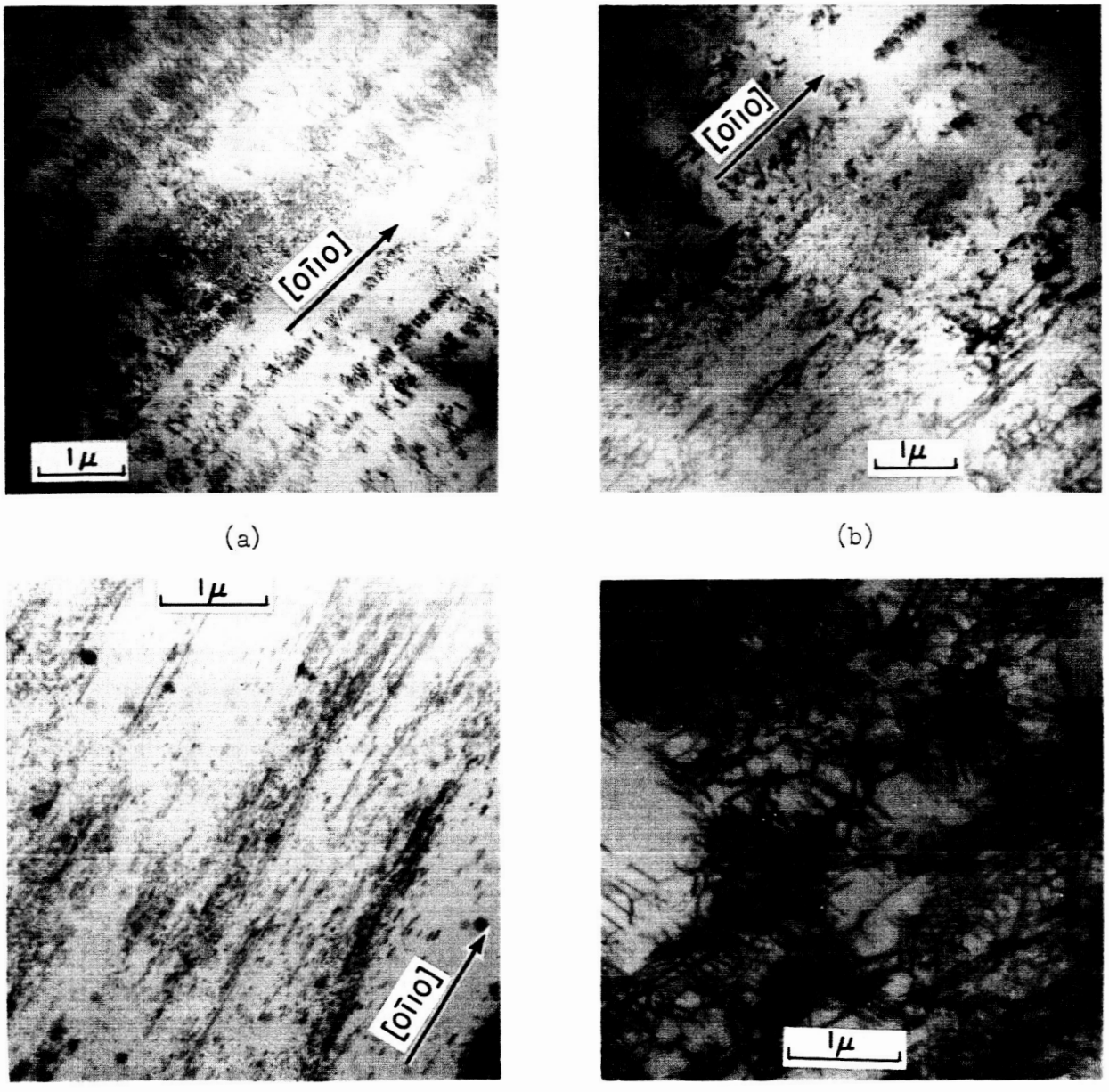

Fig. 1-4 - Dislocation Substructure Close to the Bend Surface in a Crystal Oriented for Basal Slip in Bend Fatigue. Plane of Foil is (2$\bar{1}$13).

This implies the presence of dislocations on the basal plane having a Burgers vector of either $\frac{1}{3}[1\bar{2}10]$ or $\frac{1}{3}[11\bar{2}0]$.

The slip band structure in Figure 1-4(a) is considered to arise from a rearrangement of the original fatigue substructure on thinning. It is seen that essentially all the dislocations (whose Burgers vectors do not necessarily correspond to the primary slip direction) are arranged with a minimum length through the foil on the inclined (0001) slip plane. The foil thickness in this case, as determined from the projected dislocation lengths, varied from $\sim 1000\text{Å}$ in the center of the micrograph to $\sim 4000\text{Å}$ in the upper left-hand corner. Recovery processes actually observed in thin foils in the electron microscope are considered in detail in a subsequent section.

Dislocation loops are seen in Figures 1-4b and 1-4c. In projection, the loops are nearly circular or highly elongated along the $[01\bar{1}0]$ direction. The projected shape of the small loops is compatible with their lying on planes inclined to the foil surface, and containing the $[0\bar{1}10]$ direction. Two such planes are the (0001) plane and the $(\bar{2}110)$. Since these planes are equally inclined ($\sim 45°$) to the foil surface, it would be necessary to perform a tilting experiment to distinguish between these possibilities. For an average loop diameter of 250 Å, the loop density approaches 10^{15} cm^{-3}.

The dislocation networks depicted in Figure 1-4d constitute a fourth type of dislocation substructure. The networks form extensive boundaries and presumably lie on the basal plane. In agreement with earlier observations[4,6], the nodes within the networks are not visibly extended. This is consistent with the supposed relatively high stacking fault energy of beryllium.

Axial Fatigue Observations: The axial compression fatigue specimens oriented for basal slip were given a total glide strain of 0.07. Thin foils were prepared from slices cut parallel to the basal plane, and also parallel to the $(01\bar{1}0)$ prism plane which contains the preferred shear direction $[\bar{2}110]$. In each instance, the foils were obtained from interior

regions of the fatigued crystals. In contrast to bend fatigue damage, only minor variations in the dislocation substructure occur from region to region; Figure 1-5a may be considered representative of the dislocation structure existing on the basal plane after axial compression fatigue. Characteristic features include: three-fold nodes, angular dislocations by virtue of pinning effects, and a broad spectrum of dislocation loop shapes and sizes. Elongated loops have a direction of elongation along one of the three possible $\langle 10\bar{1}0\rangle$ directions in the basal plane.

The operative reflection ($g = 11\bar{2}0$) in Figure 1-5a gives rise to diffraction contrast for all dislocations having Burgers vectors of the form $\frac{1}{3}\langle 11\bar{2}0\rangle$. The dark field micrographs, Figures 1-5b and 1-5c, use two prism plane reflections. These produce conditions of zero contrast intensity for all line and loop dislocations having a Burgers vector in the reciprocal lattice plane normal to the respective prism plane directions. Therefore, line dislocations in the basal plane having a vector $\frac{1}{3}[11\bar{2}0]$ or $\frac{1}{3}[1\bar{2}10]$ can be made extinct using either the $\bar{1}100$ or $10\bar{1}0$ reflections, respectively. Comparison of the bright field micrograph Figure 1-5a ($g = 11\bar{2}0$) with the pertinent dark field micrographs (1-5b and 1-5c) makes it clear that the line dislocations marked (A) become extinct using the $\bar{1}100$ reflection, Figure 1-5b. Dislocations marked (B) are extinct with the $10\bar{1}0$ reflection, Figure 1-5c. Since $\Sigma b_i = 0$, and there are only two independent Burgers vectors in the basal plane, the leg (C) of the node ABC must be $\pm\frac{1}{3}[\bar{2}110]$. The elongated dislocation loop marked (1) is extinct only when the $10\bar{1}0$ reflection is operative; this is also the direction of elongation, suggesting that the Burgers vector is either $\frac{1}{3}[1\bar{2}10]$, or a lattice vector out of the basal plane but normal to this prism direction. In the former case, the loop would be an edge dipole. The small, nearly circular dislocation loops are extinct when using one of the three possible prism reflections. For example, the cluster marked (2) is extinct only when using the $\bar{1}100$ reflection. By a similar argument as that used for the elongated loop (1), the Burgers vector of these loops can be either $\frac{1}{3}[11\bar{2}0]$, or be out of the plane of the loop but still normal to the $[\bar{1}100]$ direction. It is certain that both the

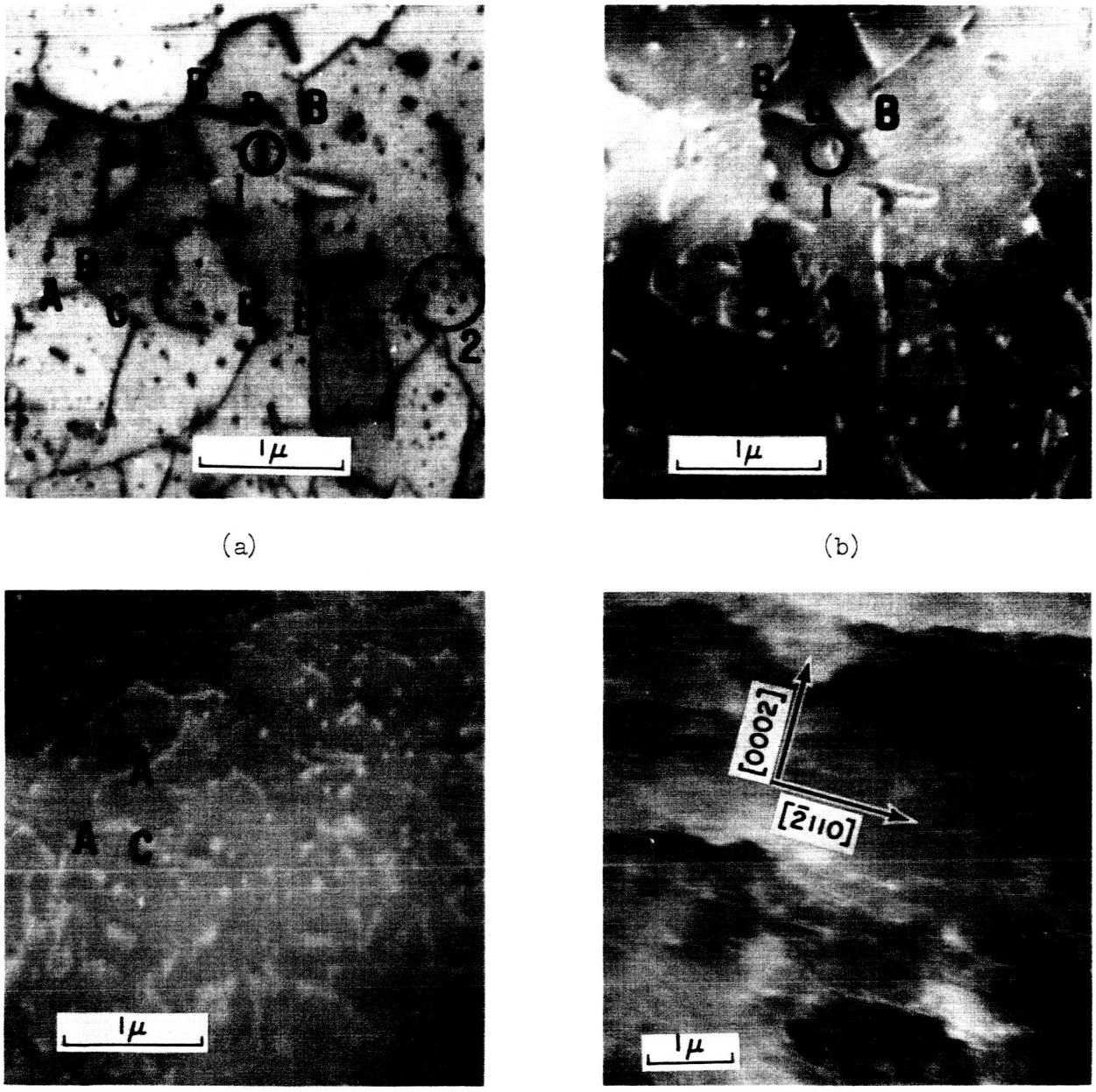

Fig. 1-5 - Light and Dark Field Micrographs of the Dislocation Substructure Following Axial Compression Fatigue. Crystal Oriented for Basal Slip. Foil Plane is (0001) in a, b, c, and (0110) in d. Operative Reflections are: 1120, 1100, 1010, 2110, in a, b, c, d, respectively.

elongated and circular loops do not have a Burgers vector $\frac{1}{2}$ [0001], since they appear in strong contrast when using reflections from planes normal to the basal plane.

The observations on loops in the bend fatigue-basal slip crystal could not distinguish whether the plane of the loop was (0001) or ($\bar{2}$110). However, since 'open' loops are seen in the foils having a basal plain orientation (Figure 1-5a,b,c), the {$\bar{2}$110} planes are eliminated as these lie perpendicular to the basal plane. Thus, the most likely plane for the loop is the basal plane. As a further check on the loop plane slices were taken parallel to the prism plane containing the shear direction [$\bar{2}$110]. Therefore, the actual basal slip plane is viewed end-on, and any dislocation loops in this plane should appear as short single lines. The slices were taken from part of the same crystal as that represented by the micrographs in Figures 1-5a through 1-5c. A dark field micrograph of the prism plane slice where the $\bar{2}$110 reflection is responsible for contrast is included as Figure 1-5d. The bands of high dislocation density on the micrograph correspond to the basal plane trace. The large numbers of nearly circular dislocation loops seen clearly in the basal plane slices are no longer resolvable, indicating that they do in fact lie on the basal plane.

b. Crystals Oriented for Prism Slip

Bend Fatigue Observations: Bend fatigue crystals oriented for prism slip on the (0$\bar{1}$10) 1/3 [$\bar{2}$110] system were subjected to fatigue in simple bending in the range 3×10^5 to 5×10^6 cycles with resolved shear stresses up to 23,000 psi. The slip structure and dislocation configurations were then examined on the tension surface.

The fatigue damage on the surfaces subjected to maximum bending stress was characterized by the formation of a pronounced duplex slip structure, and by a distinct brownish dislocation, the intensity of which increased with increasing number of cycles. The discoloration was confined to the two surfaces through which edge dislocations having the 1/3 [$\bar{2}$110] Burgers vector emerge. The intense slip bands are associated with the

preferred prism slip system, but there is ample evidence of cross slip on the basal plane where the resolved shear stress is very small. This surface structure is illustrated in Figure 1-6 for a crystal given 5×10^6 cycles at a resolved shear stress of 22,950 psi. The duplex slip structure is accompanied by the appearance of fracture lines which run across the bend surface; the overall direction of these fissures corresponds to [0001], the direction of intersection of the prism plane with the bend surface. The structure shown in Figure 1-7 is that obtained on a crystal subjected to 3×10^5 cycles at a lower stress (8250 psi). It should be noted that no surface discoloration developed under conditions of bend fatigue when the slip was confined to the basal plane. As in the bend fatigue basal slip crystals, repeated polishing and replication has revealed the presence of persistent slip bands to a depth of at least 5u. From the known direction of shadowing, all the persistent slip traces correspond to intrusions on the surface of the crystal; as in basal slip-bend fatigue, the intrusions are in the form of rows of closely spaced pits. For the crystal fatigued 5×10^6 cycles at the high resolved shear stress (22.950 psi) on the $(0\bar{1}10)$ $1/3$ $[\bar{2}110]$ slip system, the persistent bands are seen on both the prism and basal planes, Figure 1-8. On crystals given a lower number of cycles at a lower resolved shear stress on the prism slip plane, the persistent slip bands are seen only on the prism plane trace, Figure 1-9.

The transmission electron micrographs prepared close to the tension surface after bend fatigue are characterized by the presence of relatively long straight dislocations; the projected direction of these dislocations in the plane of the foil coincides with the basal plane trace, Figure 1-10. These micrographs (and the corresponding micrographs of the recovered structure, considered in a subsequent section) are of particular interest in that the operating reflection was 0002, so that g.b is zero for all three $a/3$ $\langle\bar{2}110\rangle$ slip vectors. Under these conditions, all screw dislocations are invisible, but edge dislocations give some contrast intensity due to displacements in a direction normal to the slip plane[13]. This means that dislocations such as those visible in Figure 1-10 have a large edge component, and must be in the basal plane which in this orientation is perpendicular to the plane of the foil.

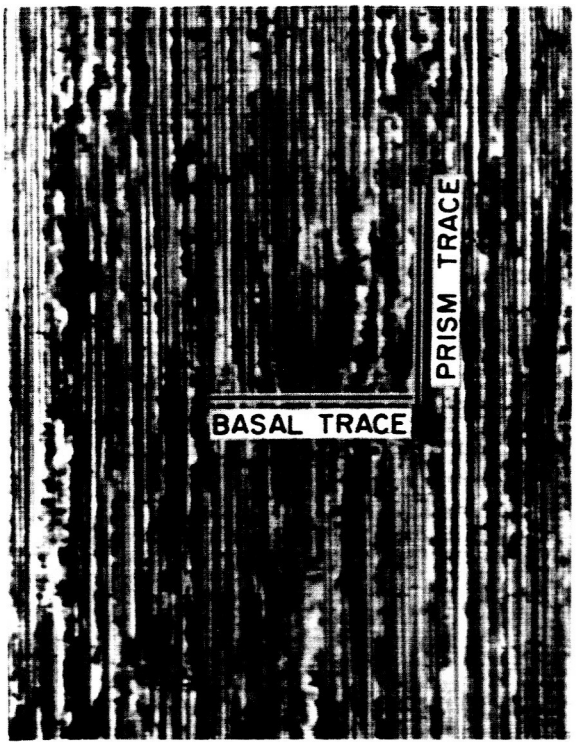

(a)

(b)

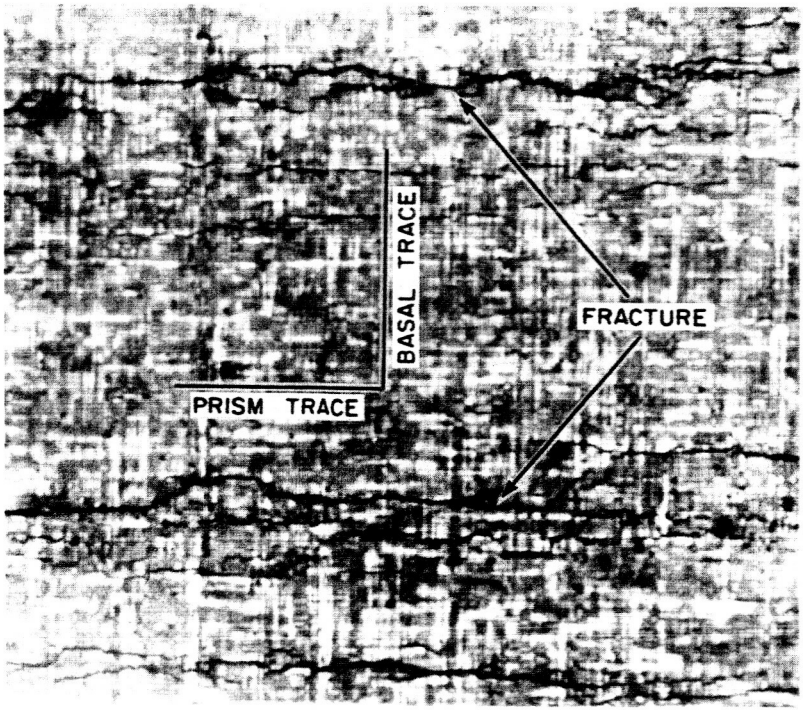

(c)

Fig. 1-6 - Optical Micrographs of the Surface Slip Structure in Bend Fatigue-Prism Slip Orientation. (a) as Fatigued (b) and (c) Fatigued and Electropolished to a depth ~ 5μ. 5 x 10^6 Cycles at a Resolved Stress of 22,950 psi. All Magnifications X300.

(a)

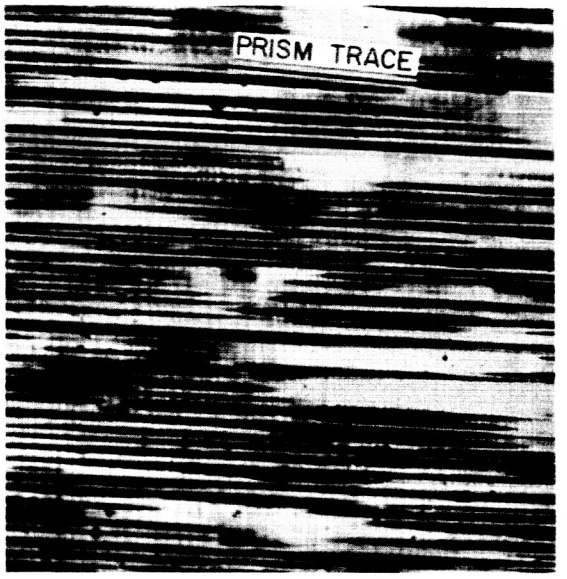

(b)

(c)

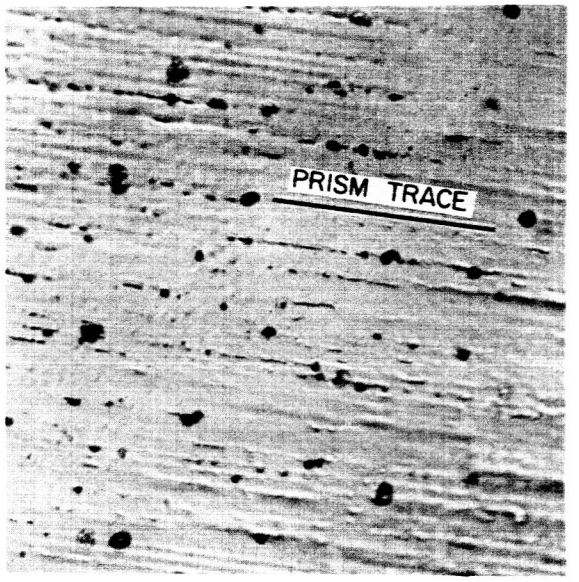

(d)

Fig. 1-7 - Optical Micrographs of the Surface Slip Structure in Bend Fatigue-Prism Slip Orientation. (a) and (b) as Fatigued (c) and (d) Fatigued and Electropolished to a depth ~ 2μ. 3 x 10^5 Cycles at a Resolved Stress of 8250 psi. Magnifications: (a) X 480 (b) X 480 (c) X 100 (d) X 480.

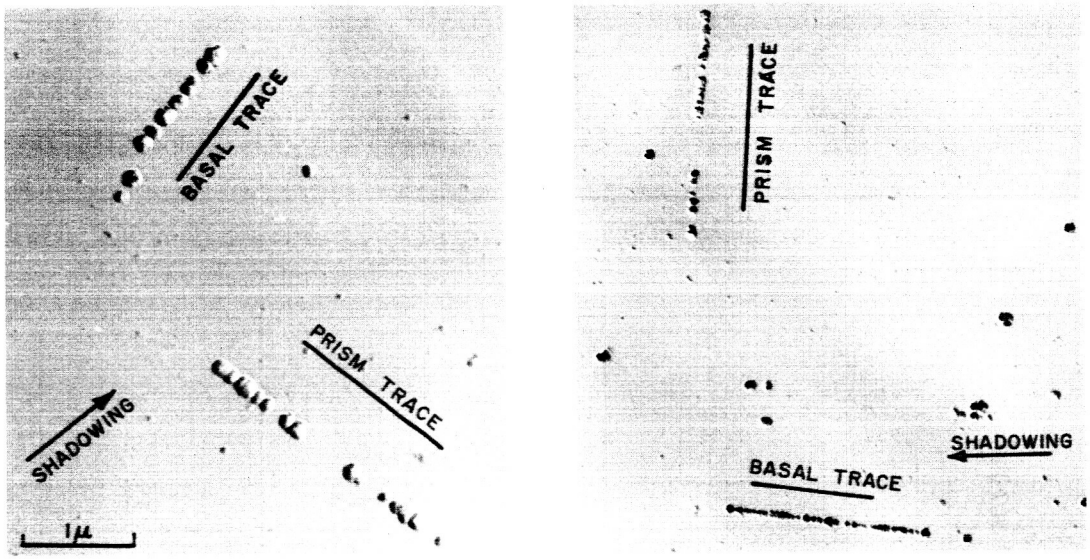

(a) (b)

Fig. 1-8 - Replication of Bend Fatigue-Prism Slip Crystal After Removal of ~ 5μ from Bend Surface. Note that the Rows of Pits Show Dark Contrast Towards the Direction of Shadowing. 5×10^6 Cycles at Resolved Stress of 22,950 psi.

Axial Fatigue Observations: The axial fatigue specimens oriented for prism slip were given a total glide strain of 0.07. In this instance, the thin foils were prepared from slices cut parallel to the $(01\bar{1}0)$ prism plane, and also parallel to the basal plane which contains the $[\bar{2}110]$ shear direction. In contrast to the long straight prism slip bands seen after bend fatigue, the slip structure following fifty cycles of low frequency tension fatigue is characterized by relatively short prism slip traces, and connecting cross-slip traces on the basal plane (Figure 1-11a). The fine details of the intense prism slip bands are resolved by replication of this surface (Figure 1-11b). Damiano and Herman[6] have observed similar but less intense slip structures in identically oriented crystals after a comparable amount of shear strain in simple tension.

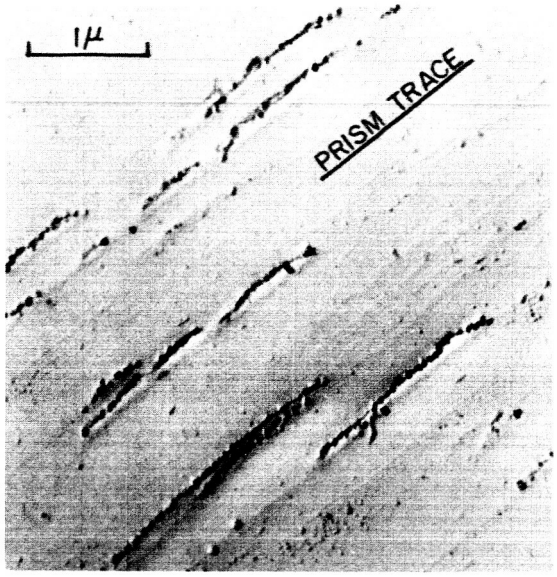

(a)

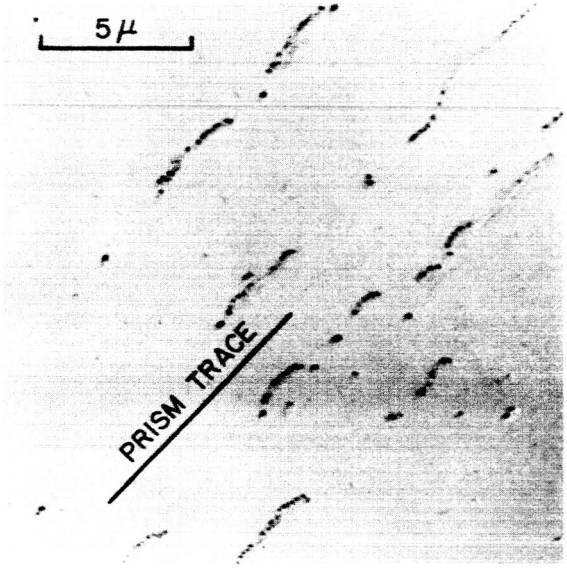

(b)

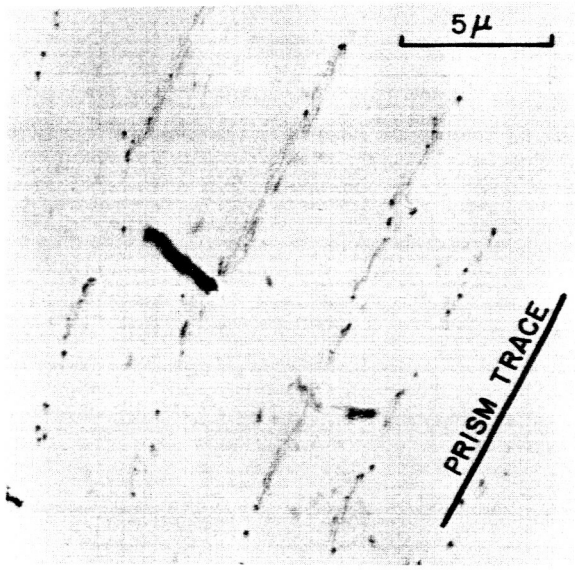

(c)

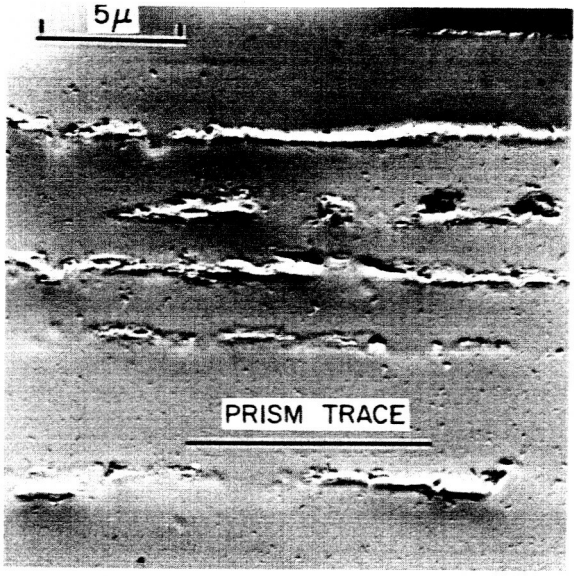

(d)

Fig. 1-9 - Surface Replica Electron Micrographs Showing Persistent Prism Plane Slip Traces. Crystal Fatigued 3×10^5 Cycles in Simple Bending at a Resolved Stress of 8150 psi, and Electropolished to a Depth $\sim 2\mu$.

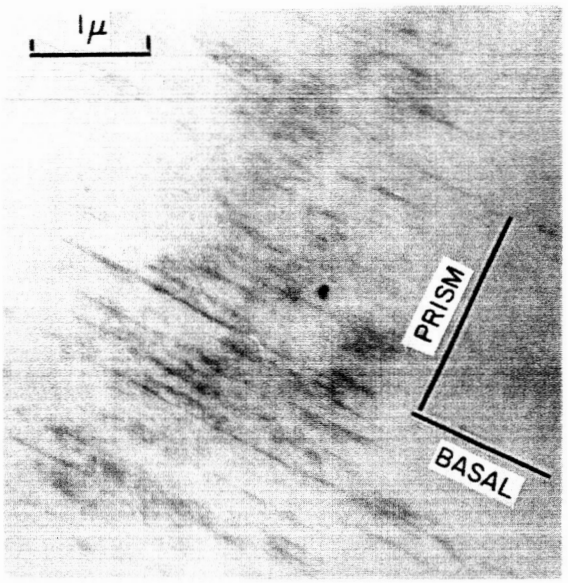

Fig. 1-10 - Dislocation Substructure Close to the Bend (Tension) Surface in a Crystal Oriented for Prism Slip in Bend Fatigue. Plane of Foil is $(\bar{4}150)$. Crystal Given 5×10^6 Cycles at a Resolved Stress of 22,950 psi.

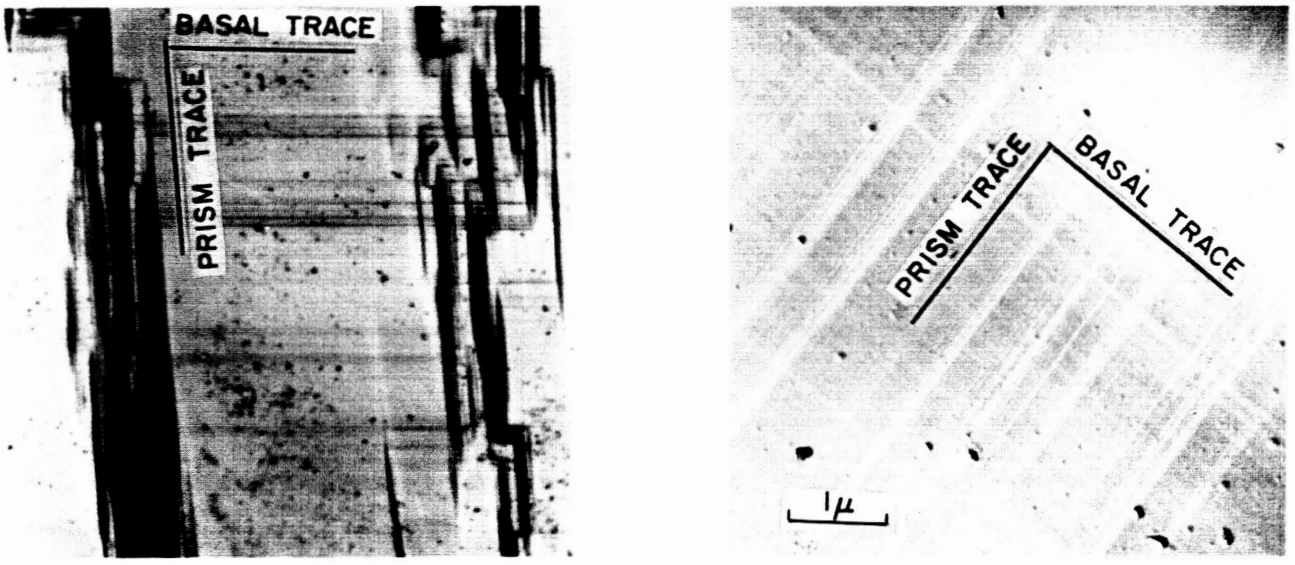

(a) (b)

Fig. 1-11 - (a) Optical Micrograph Showing Prism and Basal Plane Slip. Axial Tensile Fatigue in Crystal Oriented for prism slip. X300. (b) Corresponding Slip Structure by Surface Replication.

Figure 1-12a,b illustrates the fatigue damage on the operative prism plane, and on the basal plane, following axial tensile cycling. It was observed that in the prism plane foil orientation open dislocation loops were absent. The appearance of the dislocation substructure on the basal plane (Figure 1-12b) is similar to that observed after axial compression fatigue on crystals oriented for basal slip only, Figure 1-5a. The long lengths of the dislocations visible in Figure 1-12b demonstrate clearly that slip has occurred on the basal plane; in this case this is the cross-slip

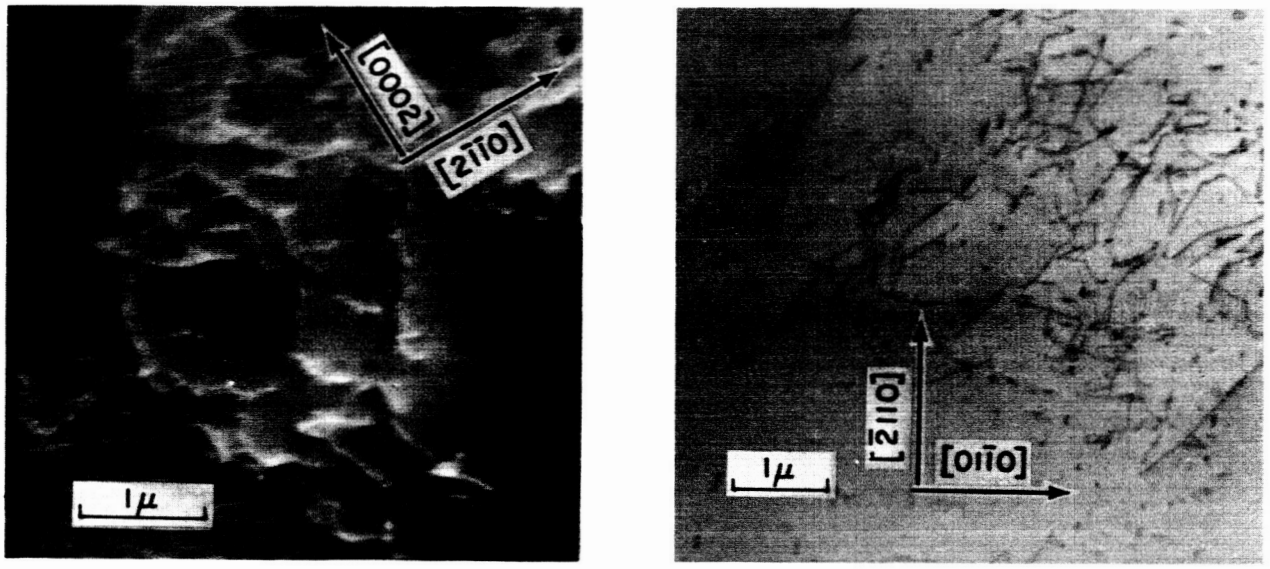

(a) (b)

Fig. 1-12 - Dislocation Substructure Following Axial Tensile Fatigue in Crystal Oriented for Prism Slip. (a) Plane of Foil (0$\bar{1}$10), Operative Reflection $\bar{2}$110. (b) Plane of Foil (0001).

plane which has a low resolved component of shear stress. None of the open dislocation loops (arrowed) seen on the basal plane slice can lie on any of the possible prism planes of type {10$\bar{1}$0} or {11$\bar{2}$0}, since these are perpendicular to the plane of the foil. Many of the loops are elongated in the [01$\bar{1}$0] direction which is normal to the operative Burgers vector, $\frac{1}{3}$ [$\bar{2}$110]. The substructure seen on the prism plane (Figure 1-12a) arises from the interaction of glide dislocations on the two systems; in common with other multiple slip conditions, this results in a complex dislocation network.

c. Recovery of the Fatigue Substructure

(i) Recovery in Thin Foils in the Electron Microscope:

After prolonged examination of a bend fatigue crystal (basal slip orientation) in the electron microscope ($\sim$ 30 minutes), a most interesting sequence of events was observed which constitutes recovery in the transmission foil. The dislocation substructure of the fatigued state (Figure 1-4a) gave way to the sequence of configurations shown in Figure 1-13a through 1-13d. Dislocations are frequently seen to move over distances of several microns on the basal plane, inclined at $\sim 43°$ to the plane of the foil. This motion gives rise to persistent traces of dark spots parallel to the line of intersection of the basal plane with the upper and lower foil surfaces (Eq. A in Figure 1-13a). Instances of dislocation motion are also evident in which the displacement is not confined to the basal plane. Under these circumstances, the point of emergence of the moving dislocation line describes a wavy path (Eq. B in Figure 1-13a). This form of configuration can be rationalized in terms of successive glide on the basal plane, and cross slip of the screw component of a $\{10\bar{1}0\}$ prism plane having a common $\langle\bar{2}110\rangle$ slip direction. It has been established (Figures 1-4 and 1-5) that all three $\langle\bar{2}110\rangle$ Burgers vectors do in fact operate in the basal plane. The prominent dislocation loops generally increase in size with only small lateral movement, although examples of decreasing size leading to disappearance of the loop have been found. Consideration of Figure 1-13 shows that the loops marked 1 through 8 increase in size with increasing time of exposure in the electron microscope. Loops 1 and 2 eventually combine, and loops 3, 4, 6 and 8 have moved completely out of the foil. The loss of a loop from the foil is accompanied by a 'ghost' image which lasts for several minutes. In terms of the time scale, once the sequence of events had started, individual loops changed size and moved out of the foil in a matter of seconds. A period $\sim$ 5 minutes was required to complete the recovery process such that the foil was completely devoid of glide dislocations and prismatic loops. Several such foils were found to recover in this way on prolonged examination in the electron microscope.

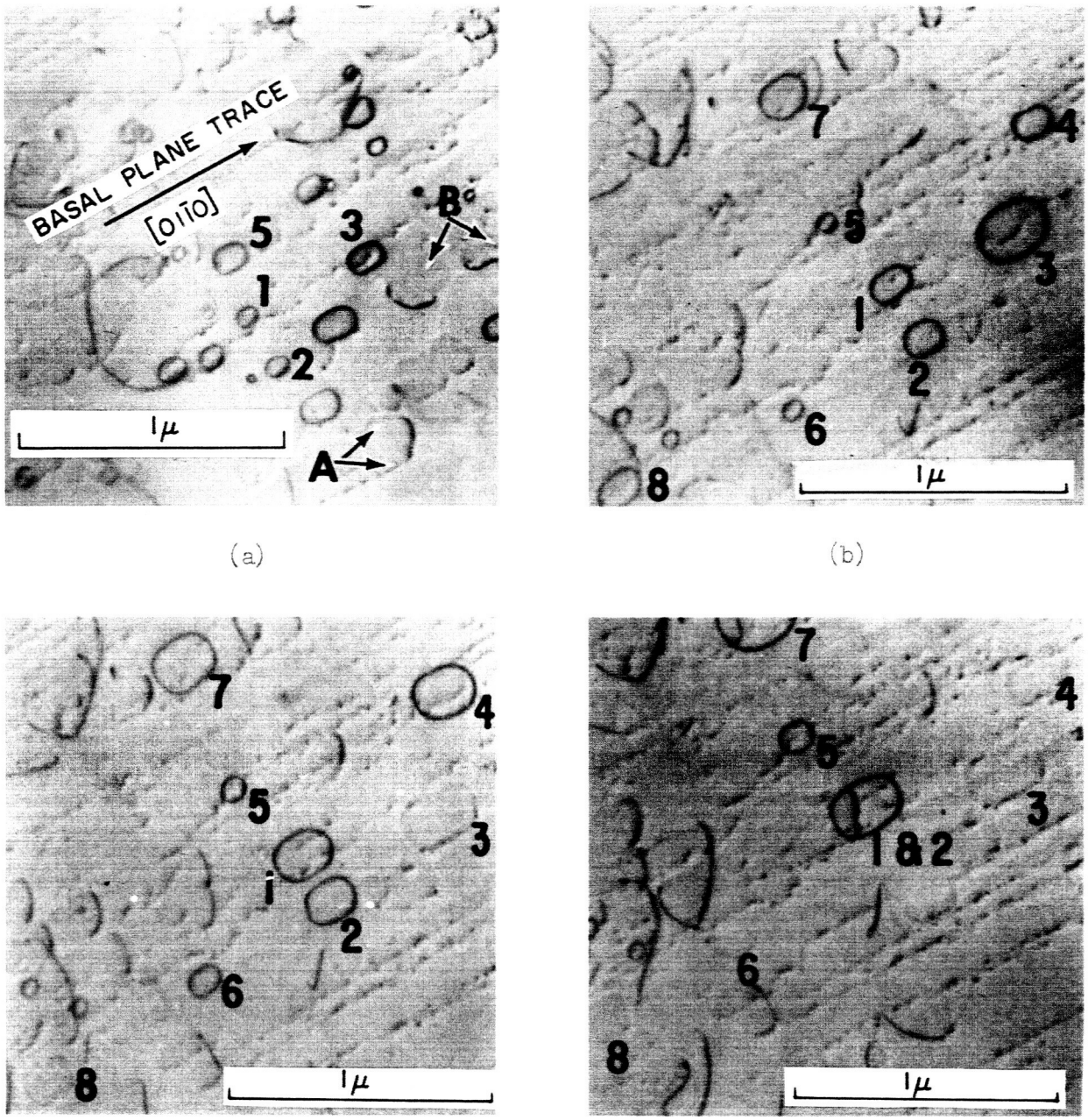

Fig. 1-13 - Sequence of Recovery Events in Crystal Originally Deformed in Bend Fatigue. Basal Slip Orientation. Plane of Foil ($\bar{2}$113), with [0110] the line of intersection of the basal plane with the foil surface.

A similar recovery process occurred in foils prepared from the bend fatigue crystal oriented for prism plane slip, Figure 1-14; the process involves similar times of exposure in the electron microscope followed by comparable rates of prismatic loop motion. The loops definitely do not lie on the basal plane since this is normal to the foil. If the projected loop shapes seen in Figure 1-14 are due to circular loops lying on a plane inclined to the foil surface, the plane has to be one of the pyramidal planes of the beryllium lattice.

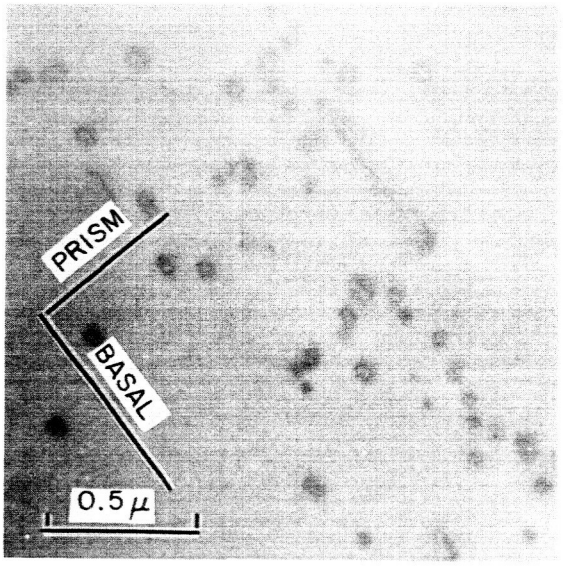

Fig. 1-14 - Recovered Structure in Crystal Originally Deformed in Bend Fatigue - Prism Slip Orientation.

It was not possible to promote recovery in the crystals subjected to axial fatigue deformation, even though the times and intensity of exposure in the electron microscope were increased. However, a foil from one of the axial compression fatigue crystals, oriented for basal slip, was set in a heating stage inside the electron microscope. In the temperature range 100-200°C, rapid motion of glide dislocations was observed along with the annihilation or growth of prismatic loops. Above ~ 300°C the overall dislocation density became extremely low.

(ii) Recovery in Bulk Crystals:

Since recovery of the bend fatigue substructure occurs in thin foils after prolonged observation in the electron microscope, the question arises as to whether (i) this phenomenon is restricted to thin foils, or (ii) does recovery also take place to this extent in bulk fatigued beryllium at relatively low annealing temperatures as a consequence of the extremely localized and intense deformation in the surface layers? In order to answer this question, further crystals oriented for basal and prism plane slip were cycled in bend fatigue. Pieces of the bulk fatigue crystals were then annealed for 1 hour at temperatures of 100°C, 200°C, and 300°C (a separate specimen of each orientation was used at each temperature). After annealing in the bulk condition, thin foils were prepared close to the original bend surface.

Representative micrographs prepared close to the bend surface in the basal slip orientation are assembled in Figure 1-15. It is clear that annealing the bulk fatigued crystal for 1 hour at 100°C does not bring about the recovery processes seen directly in thin foils of the fatigued material in the electron microscope (the temperature of the foil while under examination in the microscope is estimated to be $\sim$ 80°C). Although annealing at 100°C in bulk fatigued crystals has no effect on substructure, a similar treatment at 300°C gives rise to a rearrangement of dislocations and a lowering of the dislocation loop density, Figure 1-15c,d.

The most predominant feature of the as-fatigued substructure is the high density of prismatic dislocation loops elongated in a direction perpendicular to the favored a/3 $[\bar{2}110]$ slip direction. Similar loops are present, elongated in a direction perpendicular to the other two a/3 $\langle\bar{2}110\rangle$ slip vectors, but the density of these is much lower. These sets of loops provide strong evidence for the jogging of screw dislocations by cross-slip from the basal to the prism plane.

Similar conclusions on the recovery behavior are to be drawn from the annealing experiments on bulk crystals following bend fatigue in the prism slip orientation. The corresponding sequence of micrographs is given in Figure 1-16a,b,c,d.

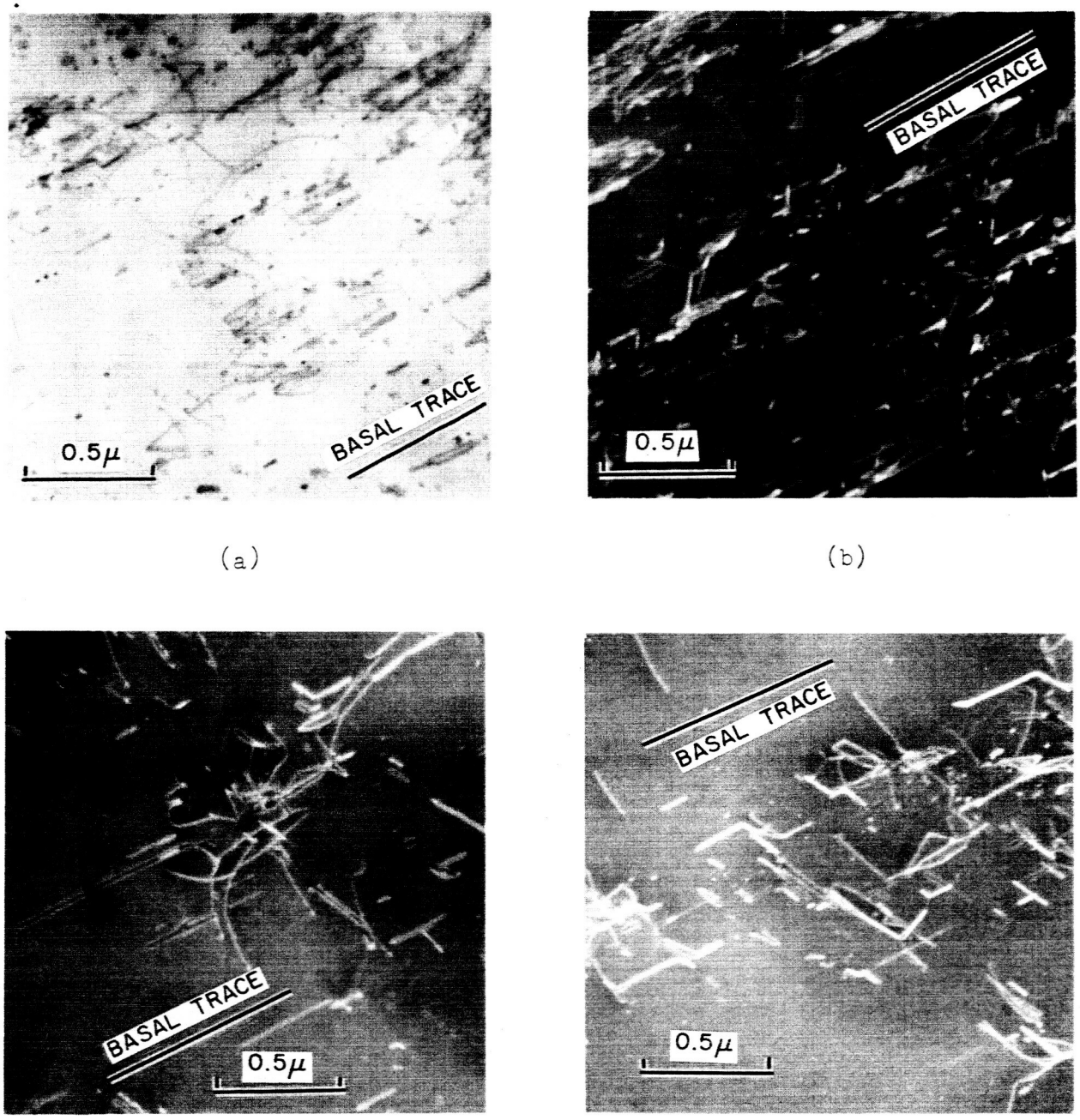

(a) (b)

(c) (d)

Fig. 1-15 - Dislocation Substructure Close to the Bend Surface in a Crystal Oriented for Basal Slip in Bend Fatigue. Plane of Foil is (2113). (a) as Fatigued (b) fatigued + 1 hour at 100°C (c) and (d) Fatigued + 1 hour at 300°C. Crystals Annealed in Bulk Condition Prior to Thinning.

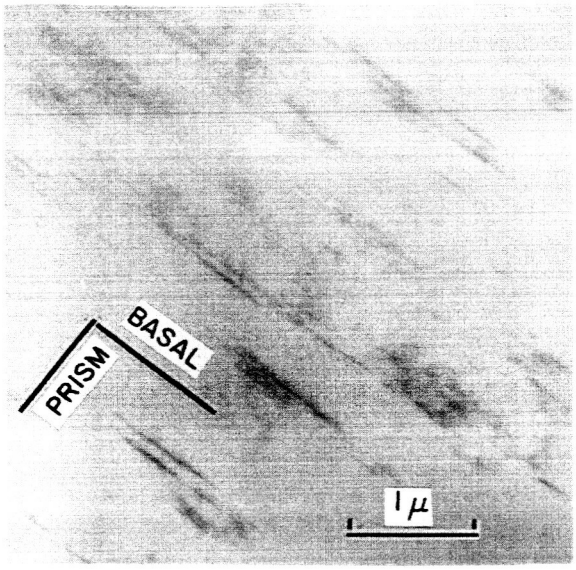

(a)

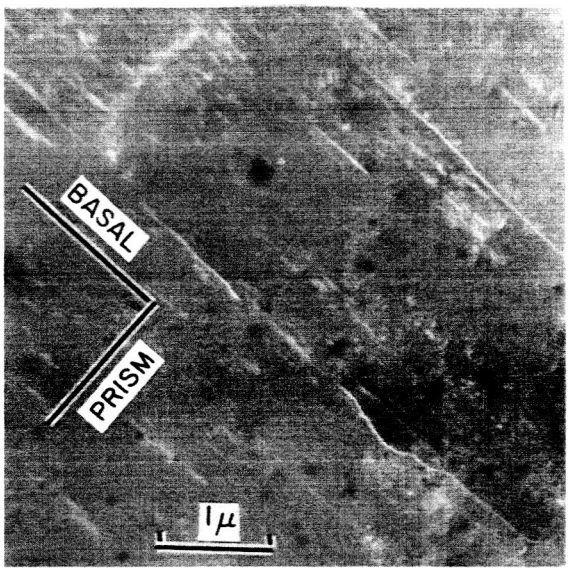

(b)

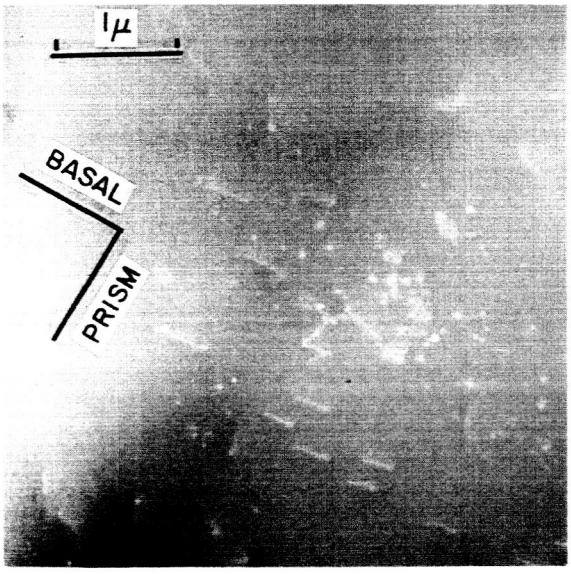

(c)

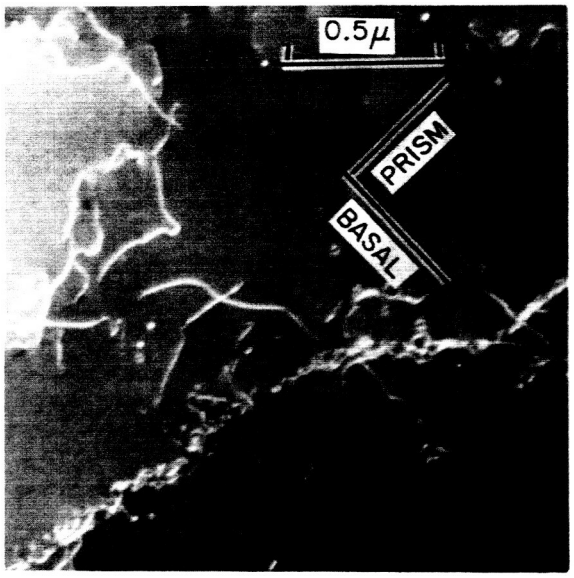

(d)

Fig. 1-16 - Dislocation Substructure Close to the Bend (Tension) Surface in a Crystal Oriented for Prism Slip in Bend Fatigue. Plane of Foil is $(4\bar{1}50)$. (a) as Fatigued (b) Fatigued + 1 hour at 100°C. (c) Fatigued + 1 hour at 200°C (d) Fatigued + 1 hour at 300°C. Crystals Annealed in Bulk Condition Prior to Thinning.

IV. DISCUSSION AND SUMMARY

(a) Reliability of the Observation

In considering the dislocation substructure following bend and axial fatigue, it is important to be aware of any possible dislocation rearrangement processes. These may occur during the preparation of the foil, or in the course of the observations in the electron microscope, as has been established for the bend fatigue foils. The extent to which the configurations are modified during thinning depends on the material. For aluminum, it is necessary to prepare foils $> 2000\text{Å}$ in thickness in order to avoid rearrangement[14] while the corresponding value in molybdendum[15] is $\gtrsim 800\text{Å}$. Experience with tapered foils of beryllium has shown that modification during thinning can occur in areas of the foil $\lesssim 4000\text{Å}$ in thickness, as shown in Figure 1-4a. A majority of the foils examined were of this thickness and, except where specifically noted, the dislocation configurations are considered to be representative of the bulk fatigued substructure without rearrangement. The stability of the substructure in the foil within the microscope, is obviously related to the magnitude of the energy stored in the lattice by virtue of the fatigue damaged. Specimens prepared from the surface layers of crystals subjected to bend fatigue are most susceptible to recovery processes due to the high level of strain in these regions. In comparison, a uniform distribution and lower level of strain exists following the axial fatigue tests. Recovery processes are less likely to occur in these cases at ambient temperature; heating of the foils in the electron microscope to temperatures $\gtrsim 100°C$ did in fact promote recovery.

(b) Dislocation Configurations

(i) Fatigue Substructure: A characteristic manifestation of fatigue damage is the existence of a high density of dislocation loops. This observation has been made in several of the close-packed metals; e.g. aluminum, copper, nickel, gold, zinc and magnesium.[7,9] The current fatigue substructures found in high purity beryllium are no exception to this pattern.

The available evidence strongly suggests that the loops formed during fatigue lie on the basal plane. Possible Burgers vectors associated with these loops are: the partial vectors $\frac{1}{2}$ [0001] (Frank dislocation) and $\frac{1}{6}\langle 20\bar{2}3\rangle$ (Frank-Shockley composite dislocation); and the perfect vectors $\frac{1}{3}\langle 11\bar{2}3\rangle$ and $\frac{1}{3}\langle 11\bar{2}0\rangle$. The diffraction contrast experiments have eliminated $\frac{1}{2}$ [0001] since the loops appear in contrast in foils having a basal plane orientation and using reflections from planes normal to the basal plane. Further, the $\frac{1}{6}\langle 20\bar{2}3\rangle$ partial vector is eliminated since the loops are extinct using reflections of the type $10\bar{1}0$. Thus, the loop vector is either $\frac{1}{6}\langle 11\bar{2}3\rangle$ or $\frac{1}{3}\langle 11\bar{2}0\rangle$ which means that in either case the loops do not give rise to a stacking fault. It is not possible to verify the absence or presence of fringes indicative of faulting in the inclined loops since the extinction distances in beryllium approach half the total foil thickness. For example, the extinction distance is $\sim$ 1500Å using the 0002 reflection.

(ii) Recovered Substructure: Extensive recovery was observed at ambient temperatures in the electron microscope in foils prepared from bend fatigue crystals of both orientations. In the case of basal bend fatigue (Figure 1-13), the large dislocation loops appear to belong to one specific set of crystal planes. From their projected shapes, the loops could be either on the (0001) plane or on the $(\bar{2}110)$ plane. The former appears to be more likely since it is difficult to envision why only one of the three possible $\{11\bar{2}0\}$ planes should be favored as the loop plane. The observation of a closed loop 'ghost' image after the disappearance of the actual loop (e.g. at the location of loops 3,4 and 8 in Figure 1-13b,c,d), is best explained in terms of a combination of climb and prismatic glide; this requires that the loops have a Burgers vector out of the plane of the loop.

Since the extinction distances in beryllium are of the same order of magnitude as the foil thickness, fringes are not expected, even in large faulted loops, should these be present. However, the appearance of the loop image does give an indication of the nature of the loop. Thus, the small loops constituting the recovered structure of the prism slip crystal (Figure 1-14) show two distinct forms of image contrast, namely light

or dark inside the loop. This could arise from differences in the depth of each inclined loop from the foil surfaces, provided the loops are faulted. In comparison, the absence of any variation of image intensity inside the large loops of the recovered structure of the basal slip crystal (Figure 1-13) points to their being perfect. These loops are believed to lie on the (0001) plane. For a better understanding of the recovery mechanism, a unambiguous determination of the loop vectors for both crystal orientations is necessary. This is possible with the use of specific diffraction contrast conditions for image formation in the electron microscope.

The annealing experiments (100°C to 300°C for 1 hour periods) on bulk crystals, oriented for basal or prism slip in bend fatigue, serve to show that the recovery effects described above occur only in thin foils. Recovery effects of this nature do not occur in foils prepared from beryllium fatigued by axial (tensile or compressive) cycling; the reason for this difference lies in the uniform distribution of fatigue damage throughout the crystal in axial cycling.

(iii) Mechanism of Loop Formation: The occurrence of dislocation loops having a direction of elongation normal to each of the three possible $\frac{1}{3}\langle\bar{2}110\rangle$ vectors (Figures 1-5a,b,c and 1-12b) can be accounted for by the model of Johnston and Gilman[16] in which a moving screw dislocation becomes jogged by cross slip. Motion of the jog will then give rise to either rows of vacancies or interstitials or of two edge segments of opposite sign depending on the height of the jog. Whether or not the coalescence of point defects to form prismatic loops can occur will depend on the point defect mobility in the beryllium at the fatigue temperature (300°K). Insufficient data are available in the literature to allow for a quantitative assessment of the interstitial atom mobility. However, by comparison with other close packed metals, and taking into account the relatively high Debye temperature (1160°K) it is estimated that interstitials are relatively mobile at ambient temperature. Thus, if trails of interstitials are formed at the small jogs these will coalesce to give interstitial loops. An estimate of the vacancy mobility can be made from a knowledge of the activation energy for self-diffusion in Beryllium (Lee et al[17], Naik et al[18]). This activation

energy is approximately 1.7eV, and if it is assumed that approximately one half of this energy represents the activation energy for vacancy migration, the calculated jump frequency is sufficient to expect some coalescence of vacancy trails into vacancy loops at ambient temperatures.

Larger jog heights of several atomic spacings give rise to trails of plus-minus edge dislocation dipoles. These may reduce their energy by pinching off to form small circular loops, or they may have their spacing reduced or be terminated by the segments of the original screw dislocation moving together again. This has been observed directly by Damiano and Herman[6], and there are several instances of this form of configuration in the present study.

The cause of the jogs is not completely clear. Although the glide dislocations intersect the grown in dislocation networks, the jogs formed in this way are glissile since the Burgers vectors of the stationary and moving dislocations are parallel and in the basal plane[6]. It is possible that in a metal such as beryllium 'obstacles' are present in the lattice in the form of submicroscopic precipitates or impurities and that these give rise to sessile jogs on moving screw dislocations. Repulsive stresses from screw dislocations on parallel planes may be sufficient to promote cross-slip.

(c) A Comparison with Simple Tension

Axial fatigue for the basal slip orientation produces a uniform dislocation substructure with no apparent predominance of edge or screw component. This is in strong contrast to the substructure developed in simple tension (Damiano and Herman[6]) for crystals of identical orientation. In stage I of the tensile test long edge pairs and edge dipoles are present, suggesting that the screws are highly mobile on the basal plane. At higher strains (stage II), the presence of numerous edge boundaries is associated with the onset of rapid work hardening. Differences also exist between the tensile and axial fatigue substructure in crystals oriented for prism slip. The tensile substructure, viewed on the prism plane, shows a predominance of screw dislocations (stage I); it is considered that the latter intersect

the grown in networks and become jogged, thereby impeding motion. In stage II, complex interactions give rise to tangled masses of dislocations. The fatigue substructure observed on the prism plane is somewhat similar to that developed in stage II of the tensile test; however, this does not appear to be derived from a structure consisting initially of predominantly screw dislocations. Since the prism slip is accompanied by cross-slip on the basal plane, a tangled dislocation configuration is to be expected if no recovery processes take place.

REFERENCES

1. Wallace, W. P., and Wallace, R. M., Light Metal Age, Vol. 13, 19 (1955).

2. W. Vickers, Trans. AIME., 230, 1535 (1964).

3. Klein, J. G., Perelman, L. M., and Bever, W. W., Brush Beryllium Co. Rep. No. WADS-TR58478 (Part 1), (1958).

4. Wilhelm, F., and Wilsdorf, H. G. F., Franklin Institute Report on Air Force Contract No. AF 33(616)-7065, March 1963.

5. Walters, G. P., van der Walt, C. M., and Makin, M. J., Conference on Physical Metallurgy of Beryllium, USAEC, Gatlinburg, Tennessee, May 1963.

6. Damiano, V. V., and Herman, M., Materials Science Research, Vol. II, Plenum Press, New York 1964.

7. Segall, R. L., Electron Microscopy and Strength of Crystals, p. 515 Interscience, New York 1963.

8. Berghezan, A., Fordeux, A., and Amelinckx, S., Acta Met. 9, 464 (1961).

9. Segall, R. L., Partridge, P. G., and Hirsch, P. B., Phil. Mag., 6, 1493, (1961).

10. Spangler, G. E., Herman, M. and Arndt, E. J., Dept. of Navy, Bureau of Naval Weapons, Contract No. W61-0221-d (1961).

11. Breedis, J. F., Lawley, A., and Zeiger, J., NASA Contract No. NASr-145, April (1964).

12. Grube, W. L., and Rouze, S. R., Proc. ASTM, 52, 573 (1952).

13. Howie, A., Direct Observation of Imperfections in Crystals Interscience, New York p. 269 (1962).

14. Wilsdorf, H. G. F., and Schmitz, J., J. Appl. Phys., 33, 1750 (1962).

15. Lawley, A., and Gaigher, H. L., Phil. Mag., 8, 1713 (1963).

16. Johnston, W. G. and Gilman, J. J., J. Appl. Phys. 31, 632 (1960).

17. Lee, C. H., Drew, J. B., Spangler, G. E., and Herman, M., Second Int. Conference on Beryllium Tech. Franklin Institute, Phila., Pa. Oct. 1964, Sponsored by AIME (This Volume).

REFERENCES (CONT.)

18. Naik, M. C. Dupouy, J. M., and Adda, Y., Second Int. Conference on Beryllium Tech. Franklin Institute, Phila., Oct. 1964, Sponsored by AIME (This Volume).

SECTION II

THE MICROSTRAIN BEHAVIOR OF SINGLE CRYSTAL BERYLLIUM

ABSTRACT

The room temperature microstrain behavior of zone-refined single crystal beryllium has been examined as a function of prestrain. Crystals oriented for basal slip were deformed in simple tension (prestrains ≤ 0.09) and by low frequency cyclic compression (prestrains $\leq .40$). The friction stress was determined from the energy dissipated in generating closed hysteresis loops as a function of forward plastic strain and maximum stress amplitude. The corresponding dislocation substructures were characterized by transmission electron microscopy. The friction stress τ_f associated with forward plastic strain amplitudes $\lesssim 5 \times 10^{-5}$ is low and in the range 0.02 - 0.13 $Kg.mm^{-2}$, with no effect of prestrain; a large fraction of τ_f is due to dislocation-impurity interaction so that the actual lattice friction stress on the basal plane is extremely small. Closed hysteresis loops exist at stress amplitudes up to the macroscopic flow stress level with corresponding forward plastic strain amplitudes as high as 2×10^{-3}. A second and much higher friction stress $\tau_{f(2)} \sim 1$ $Kg.mm^{-2}$ is effective at these strain amplitudes. Cyclic compression eliminates the region of easy glide (Stage I) in beryllium and raises the flow stress. Differences in behavior in tension and cyclic compression, and the independence of τ_f with prestrain, can be understood from a knowledge of the associated dislocation substructures.

I. INTRODUCTION

This study is concerned with the details of reversible flow and small permanent plastic strains occurring in single crystal beryllium below the macroscopic yield stress. Apart from attempting to understand the dislocation mechanism(s) that controls deformation, interest in the microstrain region of beryllium is intensified since the material has a potential application in precision inertial instruments. A knowledge of the stress levels which give rise to small permanent strains, gives a useful measure of dimensional stability.

Bonfield et al have studied the microscopic yield stress (defined as the stress required to cause a permanent strain of 2×10^{-6} in/in) in polycrystalline QMV-N50 hot-pressed beryllium as a function of surface condition[1], and dislocation substructure[2,3]. Recently, Ruckman and White[4] have made similar measurements on cast and extruded beryllium in various stages of heat treatment and surface condition. Bonfield and Li[5] extended their studies on polycrystalline QMV-N50 material to include a determination of the friction stress as a function of dislocation substructure; a friction stress of 0.28 $Kg.mm^{-2}$ was obtained for fully annealed beryllium. Although a large increase in friction stress with increasing prestrain was reported, Lawley and Meakin[6] have shown that their analysis is inconsistent with that required for hysteresis loops in the anelastic region; a definite increase in friction stress with prestrain was not established. From theoretical considerations, and also from the observation that dislocations tend to lie parallel to crystallographic directions, irrespective of purity, Wilhelm and Wilsdorf[7,8] concluded that the frictional force on moving dislocations in beryllium was high. To date, Bonfield and Li's work on QMV-N50 beryllium constitutes the only direct measurement of the friction stress.

The present paper is concerned with a study of the friction stress in high-purity single crystal beryllium using the analysis of closed hysteresis loops. Crystals oriented for single slip were prestrained by varying amounts

in tension and cyclic compression, and the corresponding dislocation configurations examined by transmission electron microscopy. This dual approach has allowed for a more detailed understanding of the process of basal slip in beryllium, the differences in substructure produced by tensile and cyclic loading, and has also provided an interesting comparison with the microstrain behavior of other close-packed metals.

II. EXPERIMENTAL PROCEDURE

(a) Specimen Preparation: Single crystals were grown from 0.5" dia. Pechiney secondary refined vacuum cast and extruded stock using the floating zone melting technique developed by Spangler et al[9]. This grade of beryllium contains ~ 1200 ppm by weight BeO, and a total < 400 ppm by weight metallic impurities. The crystals were given three zone passes, and oriented by seeding for single slip on the (0001) 1/3 $[\bar{2}110]$ system (Schmid factor 0.476). Specimens were shaped and cut to size by spark-discharge machining. The gauge lengths and gauge diameters in tension were 0.75" and 0.080" respectively; in cyclic compression the corresponding dimensions were 0.435" and 0.150". After spark machining, the specimens were electropolished to remove the surface damage from spark machining (a solution of 200 cc ethylene glycol, 20cc nitric acid, 4cc sulphuric acid, 4cc hydrochloric acid was used at a potential of 15 volts), and then annealed at 1000°C for two hours under vacuum.

(b) Microstrain Testing: The method of specimen gripping and strain measurement is shown in Figure 2-1. This assembly formed part of the complete straining jig which was located between the fixed and moving cross heads of a standard Instron machine. Design of the jig was such that strict alignment of specimen axis and stress axis is maintained during testing. For compressive loading, hardened steel balls (D) were held against the conical ends of the specimen (F).

Specimen elongation was measured by a Sanborn dc differential transformer (model 24 dc DT-050B12) which comprised a transducer (A) and core mounted on a micrometer screw (B), attached to the shoulders of the specimen by the parallel arms (C). Direct current outputs from the transducer and the Instron load cell were fed to a Moseley x-y recorder (Model 2D-2A). At maximum sensitivity, one inch of traverse on the x or y axis corresponds to a load of 9.3 pounds and an elongation of 4.9×10^{-6} inches, respectively.

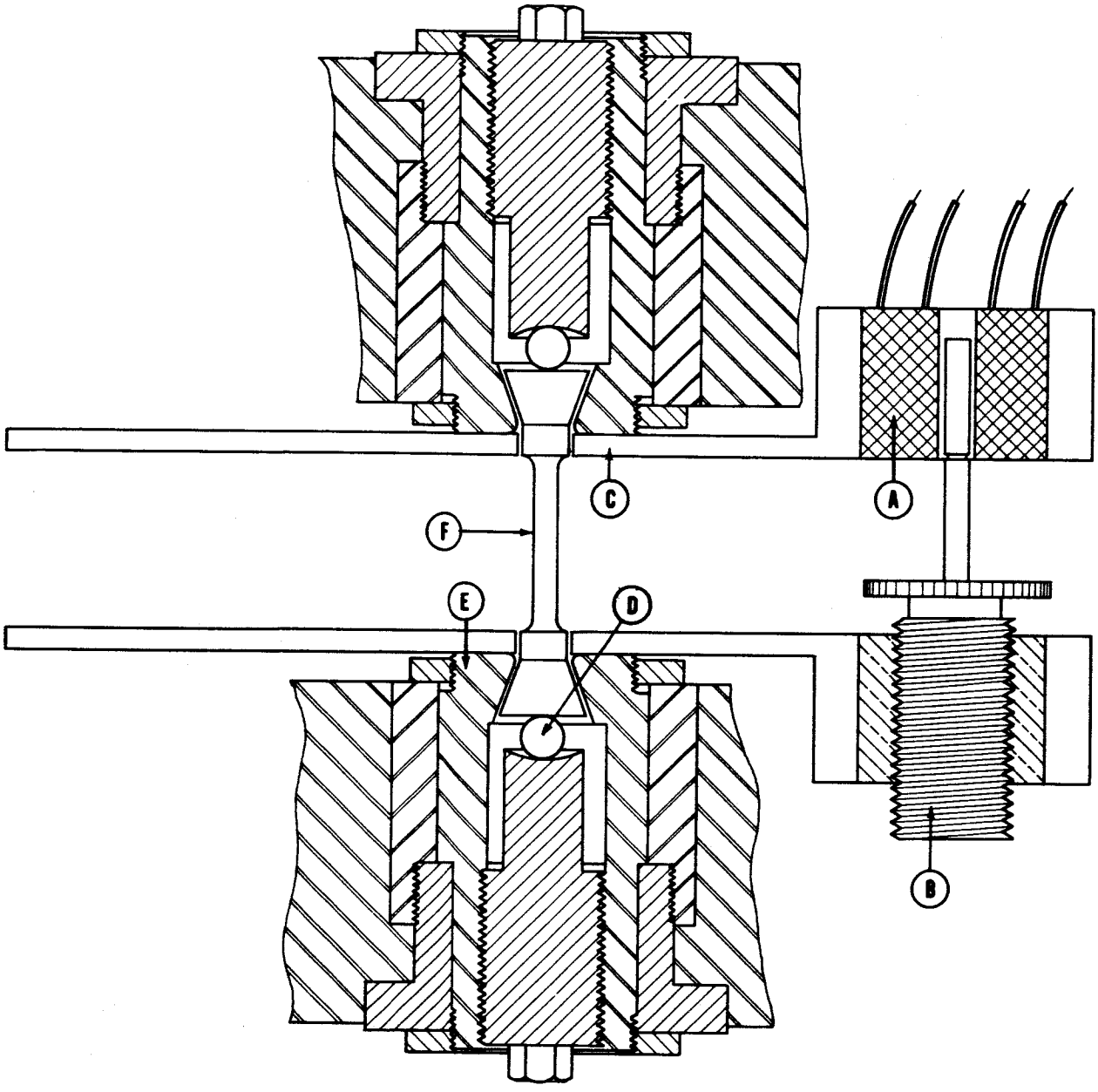

Fig. 2-1 - Method of Specimen Gripping and Measurement of Strain

In studying the anelastic behavior at a given pre-strain, a series of hysteresis loops was obtained at increasing levels of stress amplitude. To study the effect of pre-strain, the specimen was mounted in the jig, strained to the desired level, and a series of hysteresis loops then recorded. The procedure was then repeated on the same crystal for increasing increments of prestrain, without removal of the specimen. The load-elongation characteristics of the testing equipment were examined using steel specimens having a size and geometry identical to that of the beryllium crystals. Under these conditions, and for the entire load range covered in the experiments, no anelastic loops were observed.

III. RESULTS

(1) Tensile Deformation

The hysteresis characteristics and friction stress were examined at various pre-strains in the range 0.00018 to 0.087 shear. Typical sets of hysteresis loops are illustrated in Figure 2-2 for pre-strains of 0.0019 and 0.087. Closed loops are discernible above a resolved stress amplitude ~ 0.3 Kg.mm^{-2}; the loops remain closed for stress amplitudes up to $\sim 90\%$ of the macroscopic flow stress. Reproducibility of the hysteresis loops was verified by repeated loading and unloading to the same stress amplitude. Elastic modulus, determined from the slope of the elastic line at stresses below that at which closed loops form (Figure 2-2), is $\sim 35{,}000$ Kg.mm^{-2}. This is in good agreement with the value of 31,000 Kg.mm^{-2} calculated for this crystal orientation using the published elastic coefficients of beryllium[10].

The friction stress determination is based on the analysis of closed hysteresis loops. The energy ΔW dissipated in generating a closed loop is related to the maximum forward plastic strain γ_p (see Figure 2-2) by the relation:[11,12]

$$\Delta W = 2\tau_f \gamma_p \qquad (2\text{-}1)$$

τ_f is the friction stress responsible for the dissipation of energy, and is taken to be 1/2 the slope of the line generated by plotting ΔW against γ_p. The derivation of Equation (2-1) requires that the extrapolation of the best line fit at low strains ($\lesssim 5 \times 10^{-5}$) passes through the origin. The implications of a positive intercept on the strain amplitude axis, and an associated high friction stress, are discussed later. It is worth pointing out that the terms loop width and forward plastic strain are both used in the literature, and lead to confusion. The theory requires that the forward plastic strain be used in determining the friction stress. It is a simple

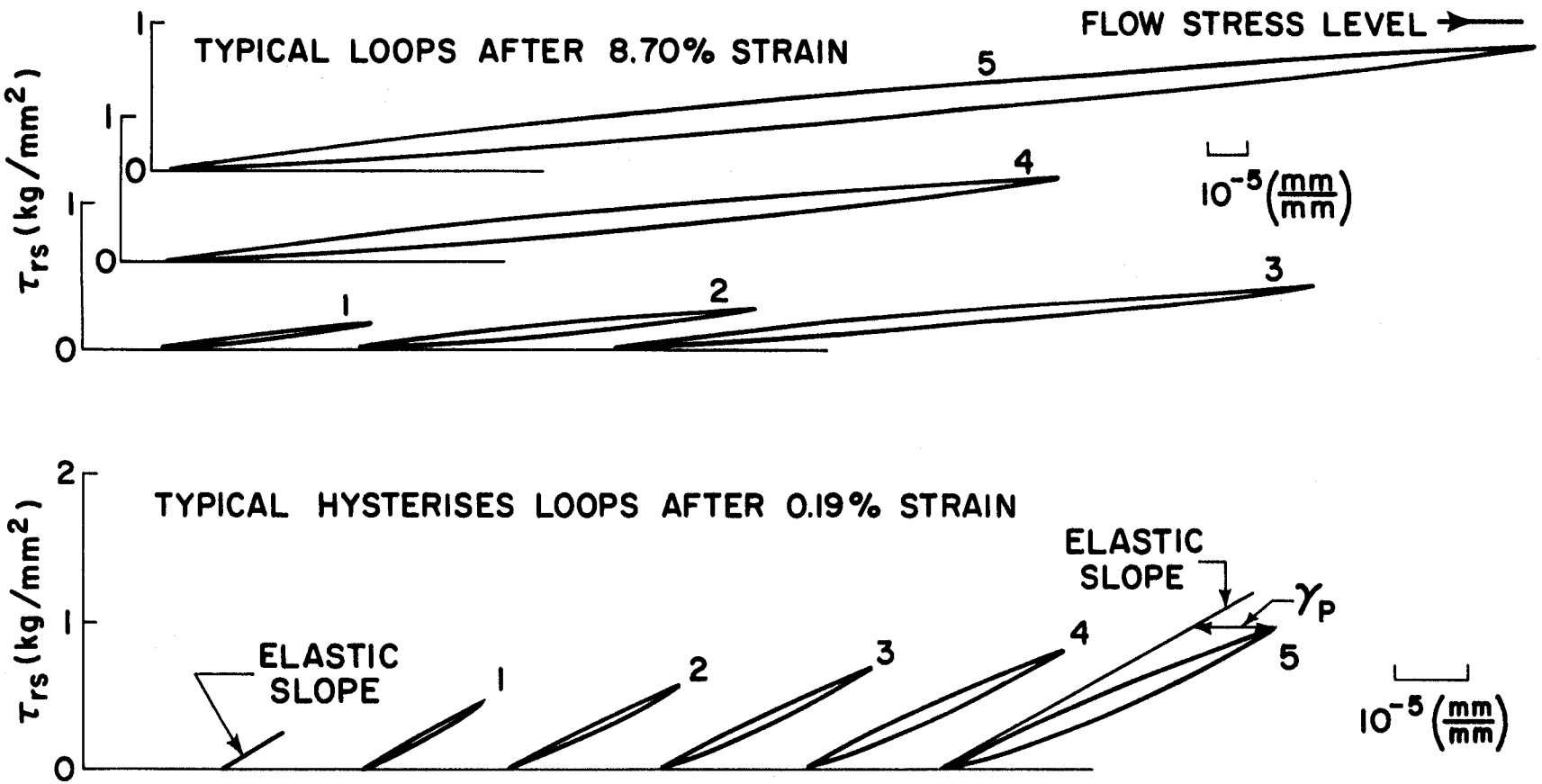

Fig. 2-2 - Sets of Closed Hysteresis Loops at Pre-strains of 0.0019 and 0.087. Single Crystal Strained in Tension.

exercise to show that if the stress amplitude exceeds $4\tau_f$, then the maximum forward plastic strain is greater than the maximum loop width. Consequently, for $\tau > 4\tau_f$, a plot of loop area against loop width will give an erroneously high friction stress.

A representative plot of loop area against forward plastic strain is given in Figure 2-3 for a crystal pre-strained 0.0146. From the slope of the line extrapolation through the origin, the value of τ_f is 0.02 $Kg.mm^{-2}$. Similar plots are obtained from the sets of hysteresis loops at all the imposed pre-strains; the corresponding frictional stresses are in the range 0.02 to 0.13 $Kg.mm^{-2}$, with no apparent dependence on pre-strain, Table 2-1.

It is also possible to determine the friction stress from an examination of the form of the anelastic loops. Upon unloading and reloading, forward plastic strain will occur at a stress $2\tau_f$, so that the minimum stress for the production of a visible hysteresis loop is $2\tau_f$. An estimate of τ_f can therefore be made either by direct inspection of the anelastic loops, or more accurately, by plotting loop area against stress amplitude and extrapolating to zero loop area. This plot at 0.0146 pre-strain is included in Figure 2-3, and gives a value for τ_f of 0.03 $Kg.mm^{-2}$; the consistency of the two approaches is apparent from the two sets of friction stress measurements listed in Table 2-1.

In terms of the macroscopic stress-strain curve, the friction stress constitutes $\sim 10\%$ of the flow stress, Figure 2-4. The macroscopic resolved shear stress-shear strain curve is for primary slip on the (0001) 1/3 $[2\bar{1}\bar{1}0]$ system. The critical resolved shear stress for basal slip (~ 0.9 $Kg.mm^{-2}$) is consistent with the stress levels reported by Spangler et al[13] for three zone-pass secondary refined Pechiney beryllium. Extensive analytical studies involving independent determinations at four laboratories (London and Herman[14]) have shown that the impurity content of the zonedmaterial is approximately 30 ppm, on an atomic basis. The non-metals carbon, nitrogen, oxygen, and fluorine contribute approximately half of this total.

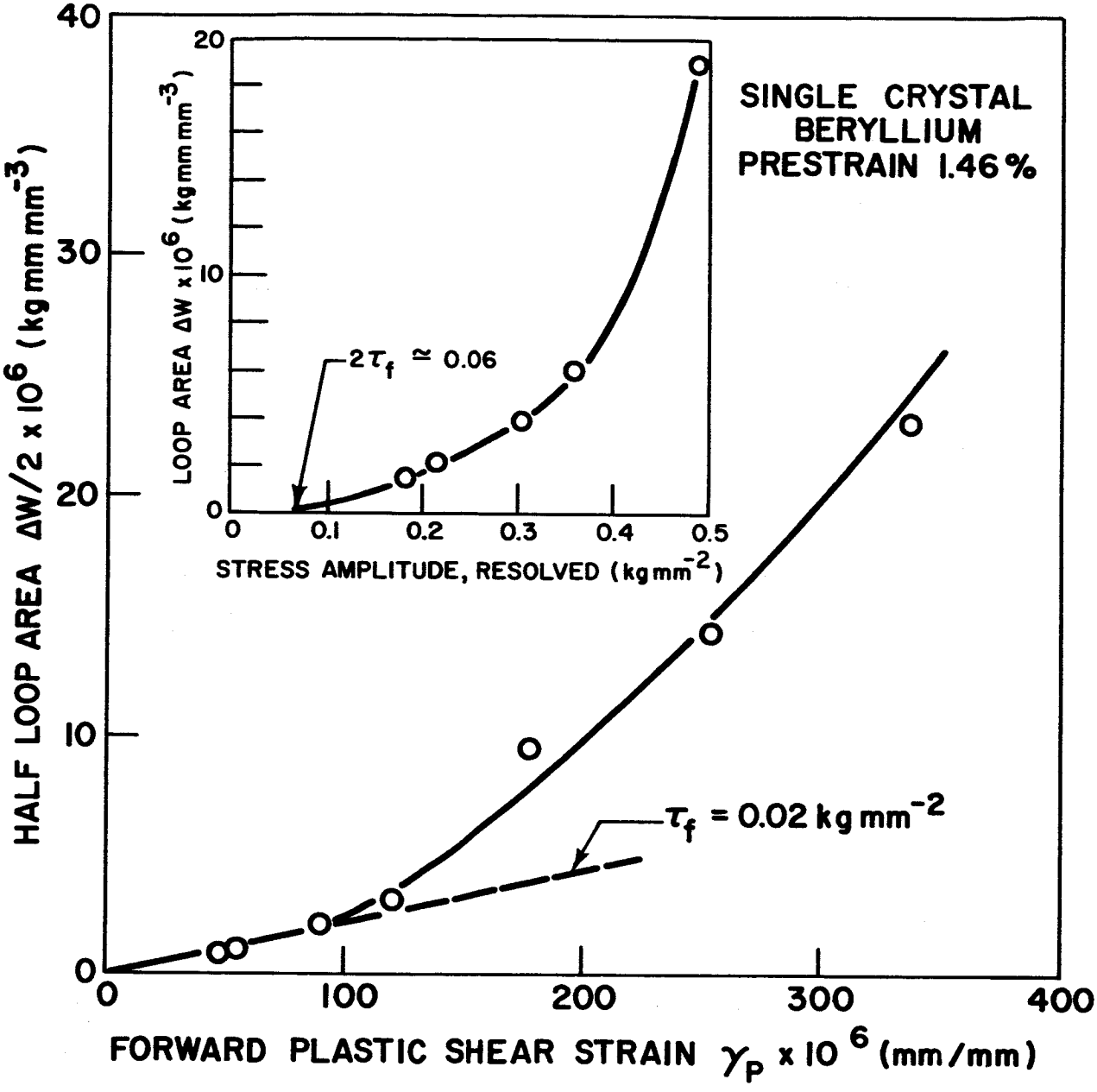

Fig. 2-3 - Plot of the Irreversible Work Against Forward Plastic Strain, and Stress Amplitude. Crystal Prestrained 0.0146 (shear) in Tension.

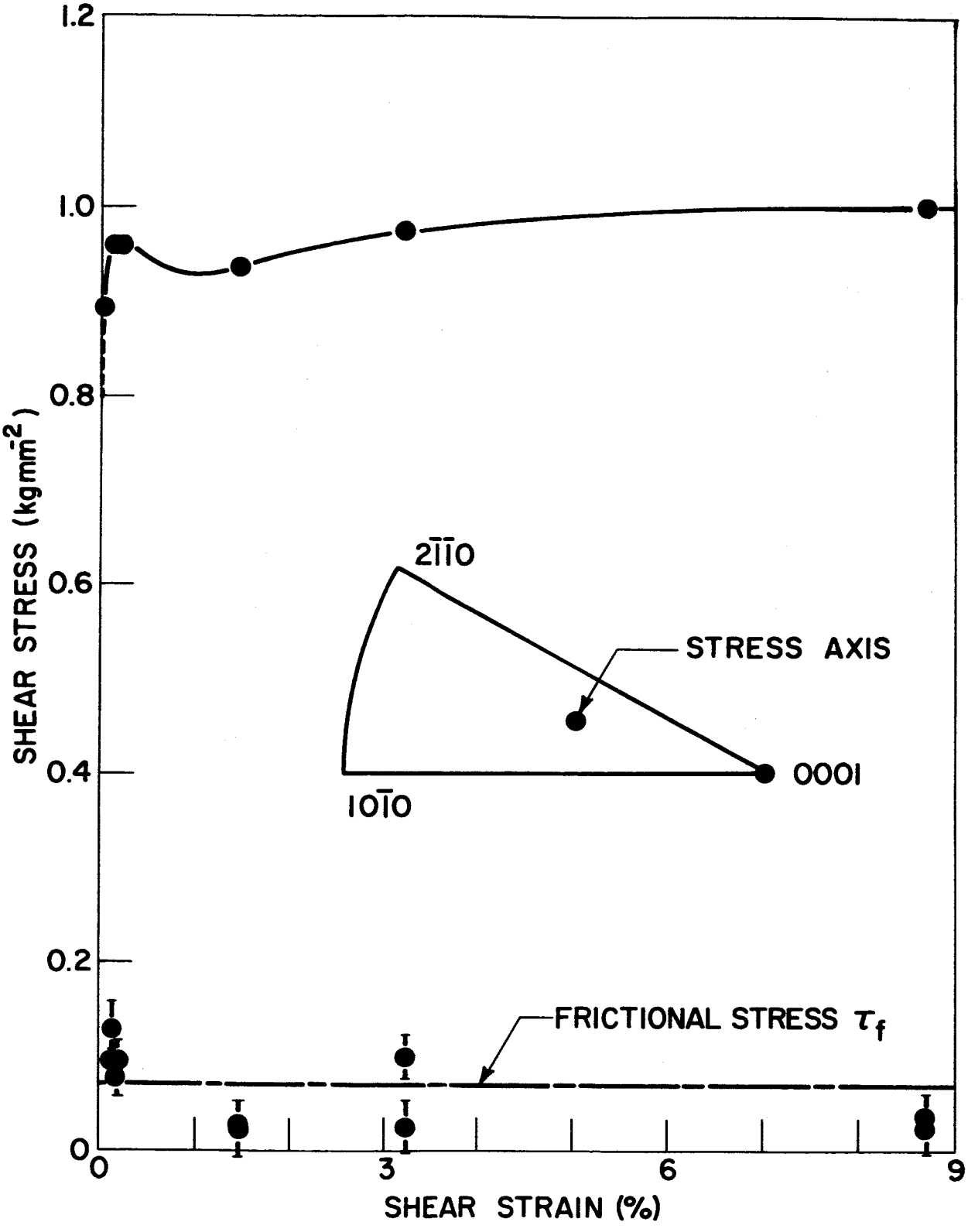

Fig. 2-4 - Representative Shear Stress-Shear Strain Curve in Tension. Initial Orientation of Stress Axis Shown in Stereographic Triangle. Experimantally Determined Friction Stress (τ_f) is Included for Comparison.

Table 2-1

SUMMARY OF THE FRICTIONAL STRESS VALUES

Pre-Strain % (Shear)		τ_f • Kg.mm^{-2} (Slope Method)*	τ_f Kg.mm^{-2} (Intercept Method)**
0.018	Tension	0.130	1.10
0.194		0.096	0.08
1.46		0.022	0.03
3.3		0.025	0.10
8.7		0.020	0.04
40 (Cyclic Compression)		0.080	0.10

*Slope given by: $\frac{\Delta W}{2\gamma_p}$

**Intercept on stress amplitude axis at $\Delta W = 0$

(2) Cyclic Compression

The cyclic compression tests were performed at a low frequency ~ 5 cycles min^{-1}. Prior to a determination of the friction stress from closed hysteresis loops, crystals were given a total pre-strain 0.40 by cycling at a constant glide strain amplitude of 0.008 per cycle. Changes in the size and shape of these open loops are illustrated in Figure 2-5, with each loop (superimposed upon a single origin) symmetrical. The slope of the nearly horizontal position of each loop remains essentially constant, but the extent of the region of constant slope decreases with increased hardening after 5 cycles. With further cycling, the transition from elastic unloading to reversible plastic flow (non-elastic strain recovery) occurs at higher values of the applied compressive stress. The cyclic work hardening curves lie well above the corresponding tensile curves, as illustrated in Figure 2-6. For simple tension in this orientation, the region of low work-hardening (Stage I) extends to $\sim 130\%$ glide strain. The large difference in stress level for a given strain in the two conditions is explainable from a knowledge of the existing dislocation substructure and will be discussed in Section IV.

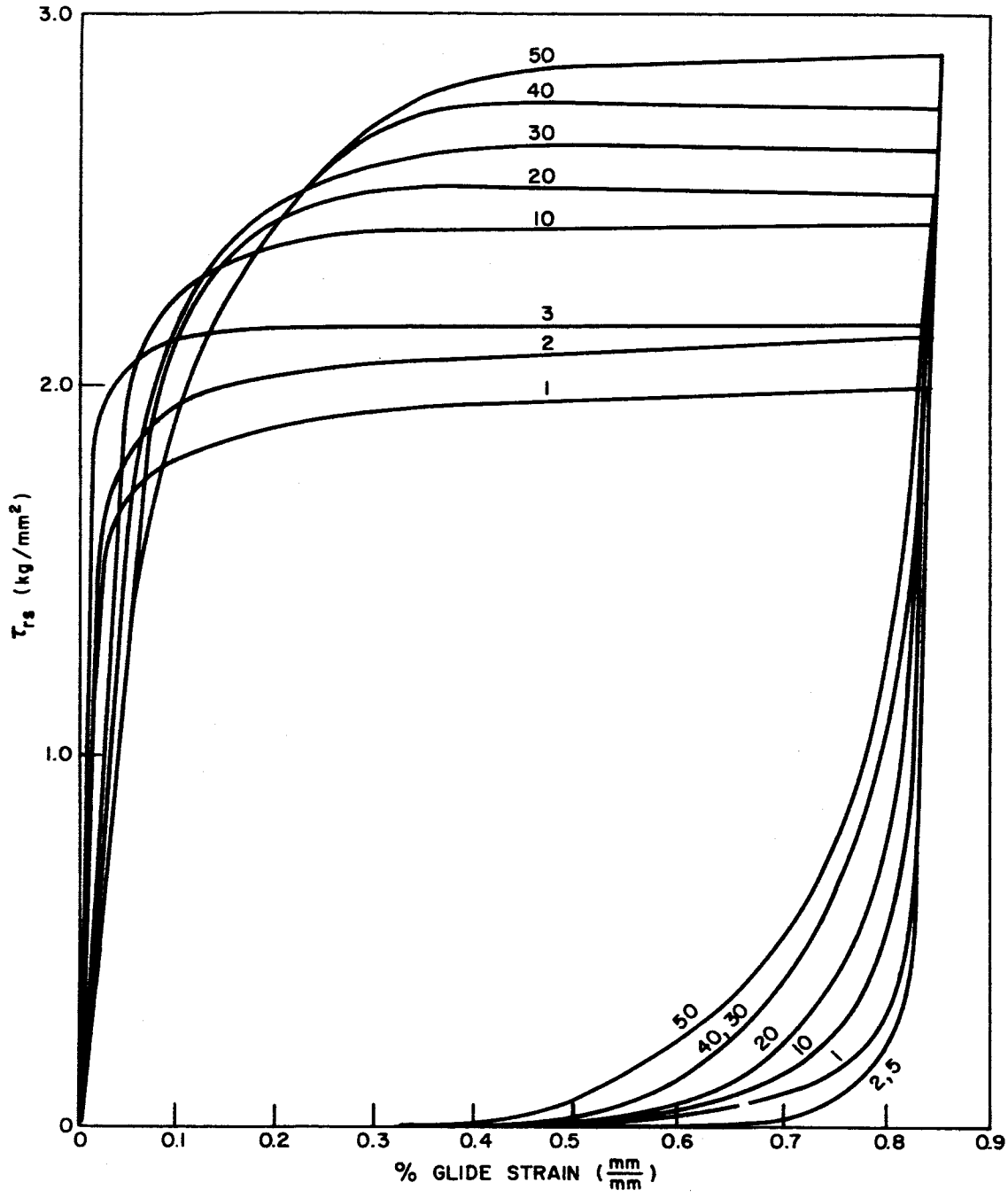

Fig. 2-5 - Cyclic Compression of Single Crystal at Constant Strain Amplitude. Numbers Refer to Order of Cycling.

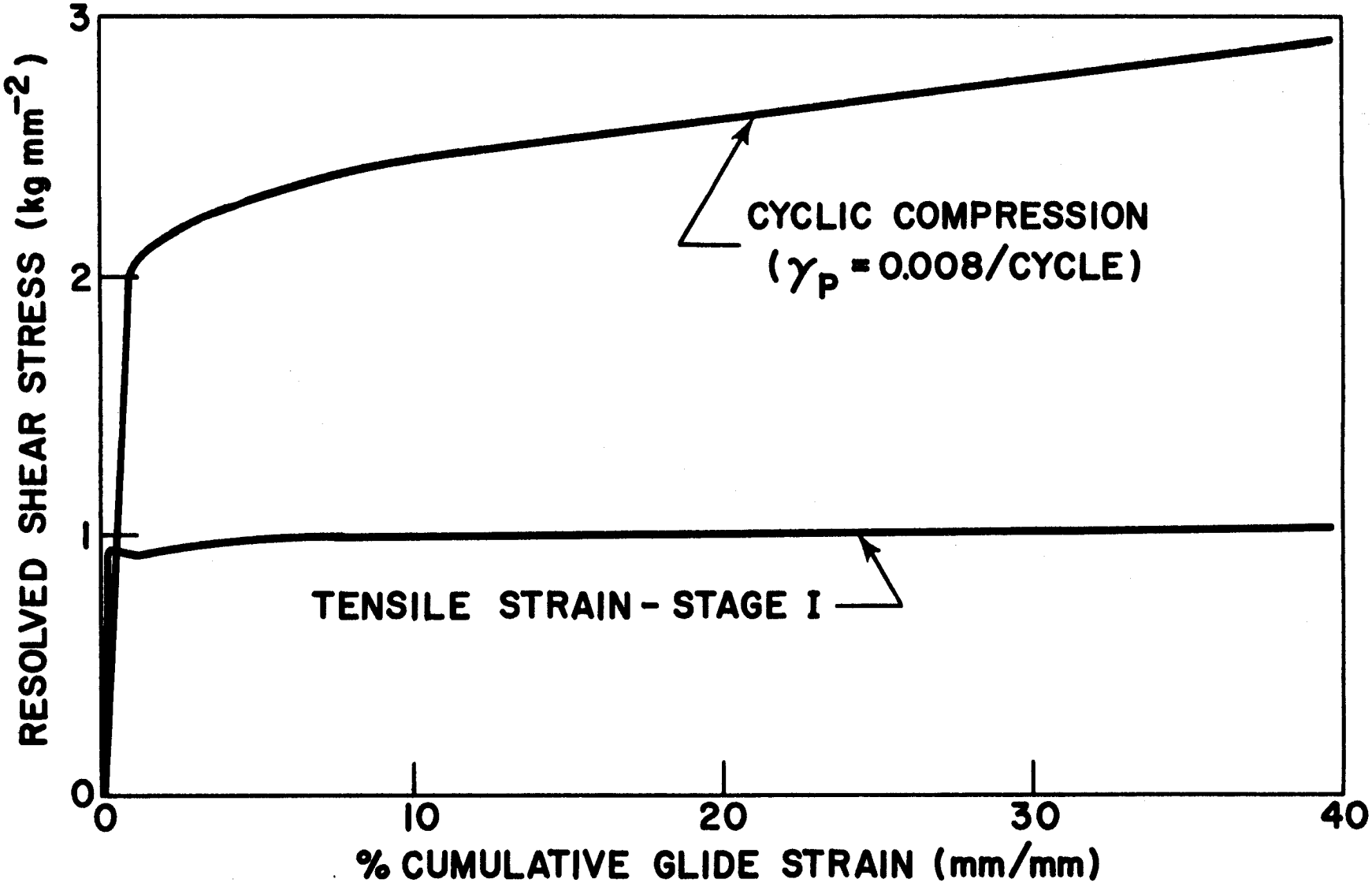

Fig. 2-6 - Cyclic Work-Hardening Curve and Tensile Curve, Versus Cumulative Glide Strain, for Basal Slip Orientation.

Anelastic hysteresis loops obtained after a cyclic pre-strain of 0.40 are illustrated in Figure 2-7. As in the case of tensile pre-strain, the loops remain closed at stress amplitudes (2.8 $Kg.mm^{-2}$ for loop #9) close to the macroscopic flow stress i.e. 2.92 $Kg.mm^{-2}$ (Figures 2-5 and 2-6). The corresponding plot of irreversible work against forward plastic strain, and stress amplitude, is given in Figure 2-8, and the friction stress (average value) listed in Table 2-1. As in the case of tensile deformation, the elastic modulus determined from the slope of the elastic line at stresses below that at which closed loops form is in good agreement with the calculated modulus.

(3) Dislocation Configurations

Interpretation of the results on anelastic behavior is considerably enhanced by a knowledge of the dislocation substructure present in the as-grown crystals, and after pre-straining. Damiano and Herman[15] have made a detailed examination of zone-melted single crystals in the as-grown condition and after tensile deformation of single slip orientations. In the as-grown crystals, most of the dislocations are arranged in networks and subboundaries with a mesh size in the range 0.1μ to ~ 1μ. The nets are planar and lie in the (0001) plane; dislocation contrast experiments show the nets to be made up of dislocations having 1/3 $\langle 11\bar{2}0\rangle$ Burgers vectors. Nodes are contracted suggesting that the stacking fault energy is > 30 $ergs.cm^{-2}$[7]. In Stage I of basal slip (which extends to ~ 120% glide strain) the dislocation structure consists mostly of edge pairs, indicating that the screws move more easily than the edges, contrary to what is generally found in FCC and BCC metals. The deformation is extremely inhomogeneous in that the edge dislocations are arranged in groups or pockets. These observations have been confirmed in the current program.

No electron microscope studies of this nature have been reported involving cyclic loading; consequently, as an integral part of the micro-strain study, thin foil observations were made parallel to the basal plane, and also parallel to the $(01\bar{1}0)$ prism plane containing the preferred $[\bar{2}110]$ shear direction. In contrast to tensile deformation, compressive cycling produces a uniform dislocation substructure on the (0001) slip plane with

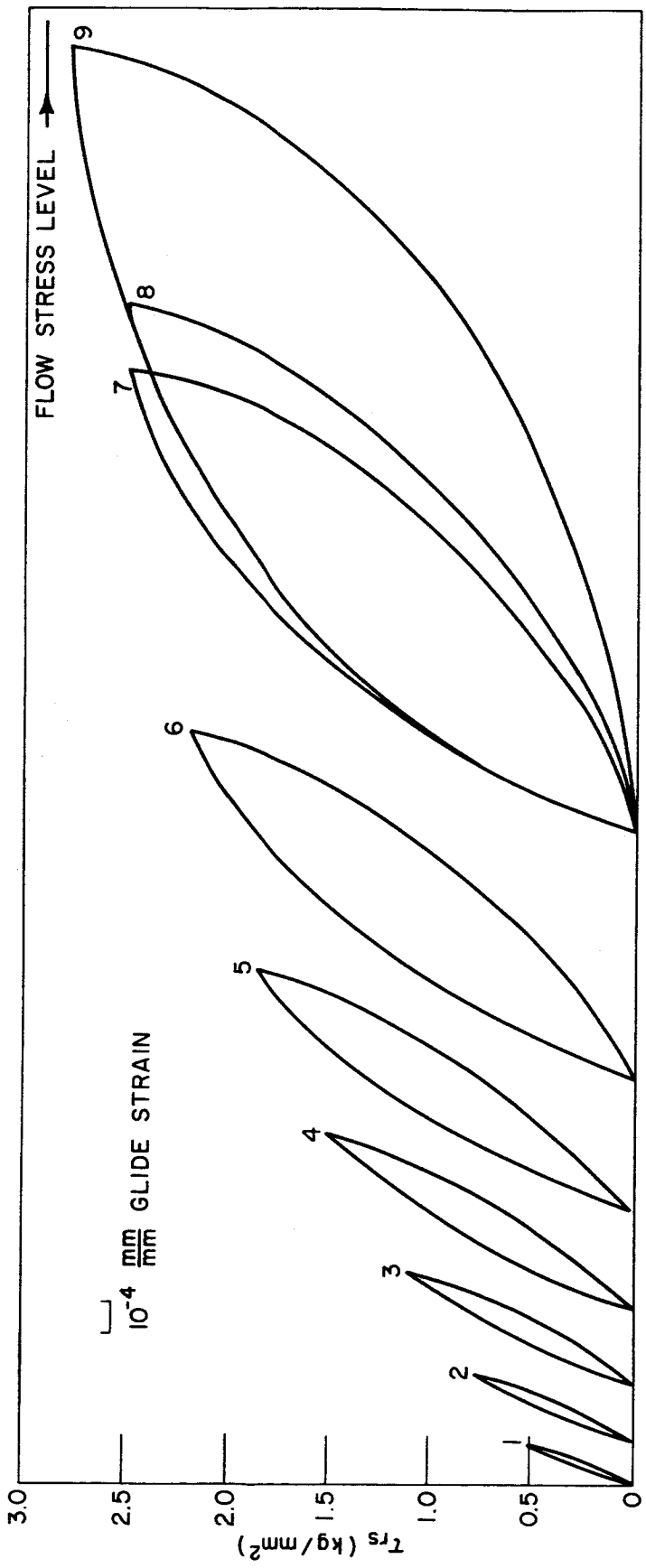

Fig. 2-7 - A Set of Closed Hysteresis Loops Obtained After a Total Pre-strain of 0.40 (shear) in Cyclic Compression.

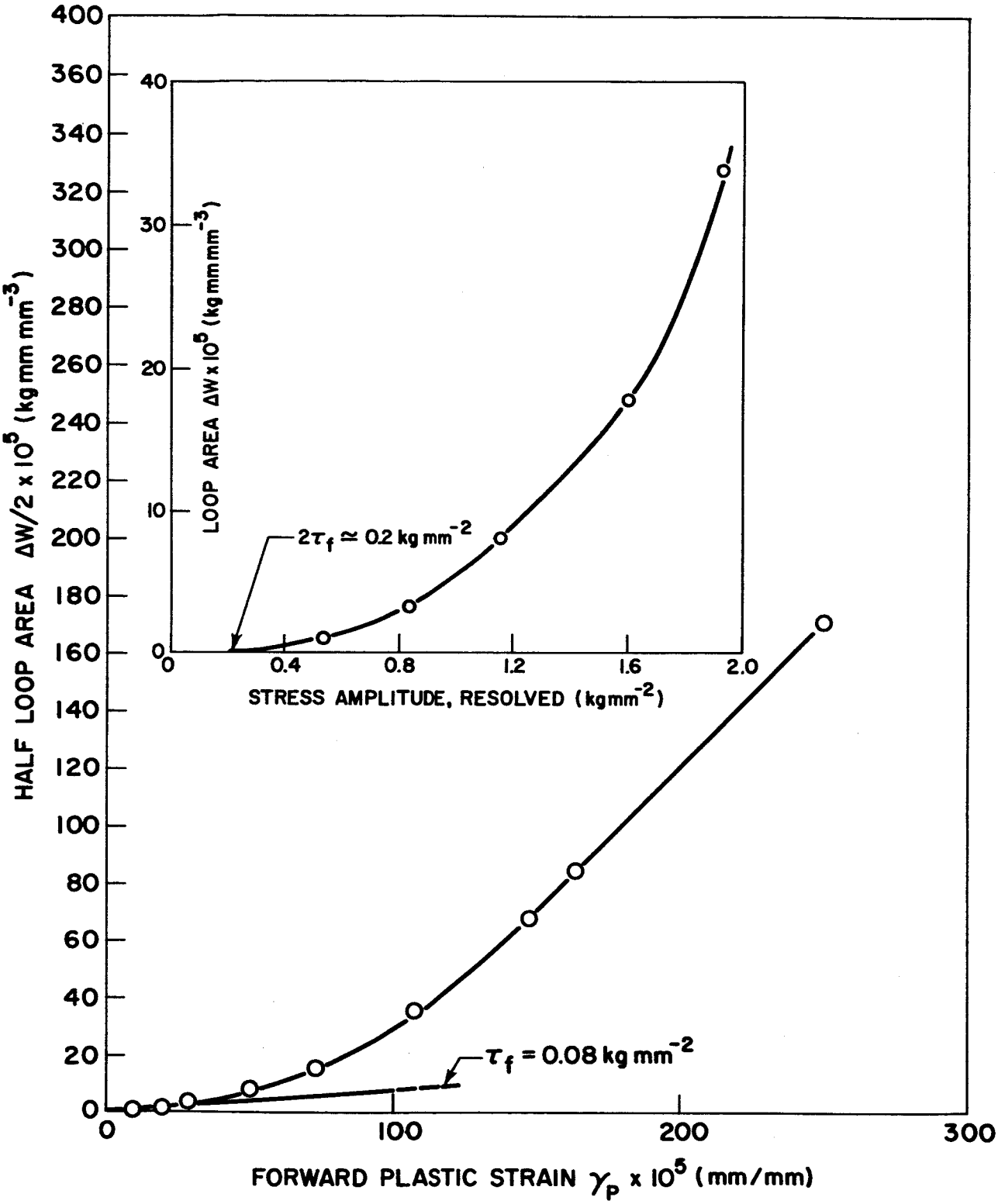

Fig. 2-8 - Plot of Irreversible Work Against Forward Plastic Strain, and Stress Amplitude. Crystal Prestrained 0.40 (shear) in Cyclic Compression.

no predominance of edge or screw component. The micrographs in Figure 2-9 illustrate the substructure after a glide strain 0.07. Characteristic features include: three-fold nodes, angular dislocations by virtue of pinning effects, and a broad spectrum of dislocation loop shapes and sizes. Elongated loops have a direction of elongation along one of the three possible $\langle 10\bar{1}0 \rangle$ directions in the basal plane normal to each of the three possible $1/2 \langle 11\bar{2}0 \rangle$ vectors. The operative reflection ($g \equiv 11\bar{2}0$) in Figure 2-9(a) gives rise to diffraction contrast for all dislocations having Burgers vectors of the form $1/3 \langle 11\bar{2}0 \rangle$; using each of the three $10\bar{1}0$ type reflections in turn, it is verified that all three Burgers vectors of the form $1/3 \langle 11\bar{2}0 \rangle$ are present. The prismatic dislocation loops which are clearly seen on the basal plane are not resolvable in the prism plane foils, indicating that the loops lie on the basal plane. Since the extinction distance in beryllium is of the same order of magnitude as the foil thickness, a change from bright field to dark field illumination gives rise to a reversal in dislocation contrast (black to white). The bands of high dislocation density in Figure 2-9(b) delineate the basal plane trace. However, these bands are not straight and precisely parallel to $[\bar{2}110]$ over long lengths but show a wavy character; this is interpreted as evidence of the cross slip of segments of screw component from the basal plane to the prism plane (the plane of the foil).

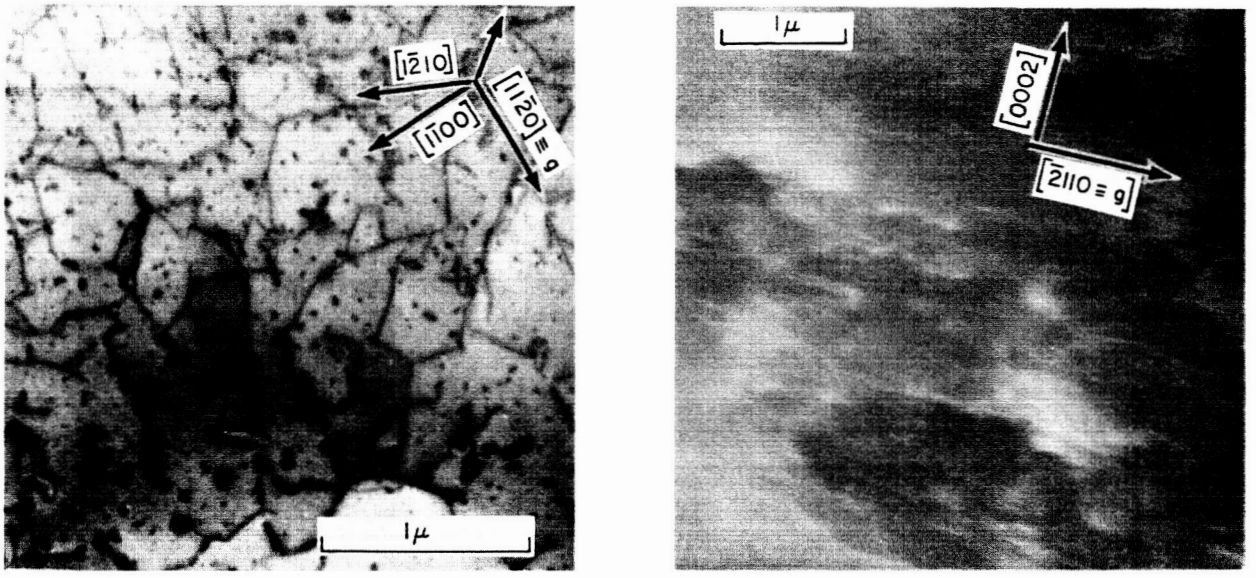

Fig. 2-9 - Dislocation Substructure Following Axial Cyclic Compression. Crystal Oriented for Basal Slip (a) Plane of Foil is (0001) with 11$\bar{2}$0 the Operative Reflection in Bright-Field. (b) Plane of Foil is (01$\bar{1}$0) with $\bar{2}$110 the Operative Reflection in Dark-Field.

IV. DISCUSSION

(1) The Initiation of Dislocation Motion

Contrary to earlier prediction[7], the friction stress in beryllium oriented for basal slip is low and in the range 0.02 to 0.13 $Kg.mm^{-2}$. This constitutes $\sim$ 10% of the flow stress. Note that this is the friction stress associated with closed hysteresis loops giving rise to forward plastic strain amplitudes $\lesssim 5 \times 10^{-5}$. In single crystals of zinc,[12] aluminum,[16] and copper,[17] the corresponding friction stresses are 0.004 $Kg.mm^{-2}$, 0.03 $Kg.mm^{-2}$, and $\sim$ 0.15 $Kg.mm^{-2}$ respectively; in each case, the friction stress constitutes a higher percentage of the flow stress ($\sim$ 20-30%) than in beryllium.

In the analysis of closed hysteresis loops, the friction stress τ_f is defined as the stress resisting the bowing of dislocation segments between pinning points. Major contributions to τ_f arise from the Peierls-Nabarro force of the lattice, and the interaction of dislocations with impurity solute atoms. Conrad[18] has shown that the strengthening in beryllium due to solid solution hardening can be approximated by:

$$\frac{\partial \tau}{\partial c} \simeq (\mu/10)$$

where c is the atom fraction of solute impurity, and μ is the shear modulus. A similar dependency exists in BCC and FCC metals,[19] for substitutional atoms. For the zone-refined beryllium, $c \simeq 30 \times 10^{-6}$, and taking $\mu = 16 \times 10^{11}$ $dynes.cm^{-2}$, $d\tau \simeq 0.04$ $Kg.mm^{-2}$. Although this value is only approximate, it does suggest that a large fraction of τ_f is due to dislocation-impurity interactions, and that the actual lattice friction stress <u>on the basal plane</u> is extremely small. From a consideration of the measured values of activation volume (V*), activation energy (H_o), and frequency factor (ν), in beryllium, Conrad[18] has concluded that the dislocation mechanism responsible for the effect of temperature and strain-rate <u>on basal slip</u> is the intersection of dislocations on non-basal planes; this implies the existence of a low friction stress τ_f on the basal plane, thereby eliminating the Peierls-Nabarro stress

as the controlling mechanism. It would be highly instructive to measure τ_f for prism slip since Conrad concludes that in this case the Peierls Nabarro stress is the controlling mechanism, and τ_f should be significantly higher.

A lack of any dependence of τ_f on pre-strain is in keeping with the observed dislocation substructures. By virtue of the closed loop analysis at forward plastic strain amplitudes $\lesssim 5 \times 10^{-5}$, the friction stress τ_f, measured at any prestrain, is that stress associated with the bowing of dislocations over small distances $\ll$ 1/10 micron. Consequently, with the form of substructure developed by prestraining in tension or cyclic compression (Section III (3)), increases in τ_f arising from dislocation intersections or elastic interaction with other dislocations are unlikely.

(2) Anelastic Behavior at High Forward Plastic Strain Amplitude

The microstrain behavior of single crystal beryllium oriented for basal slip is unusual in that closed hysteresis loops can be traced at stress amplitudes up to the macroscopic flow stress level (Figures 2-2 and 2-7); the corresponding plastic strain amplitudes are as high as 2×10^{-3}. In zinc[12], open loops are observed at stresses well below the flow stress, with corresponding strain amplitudes in the range 5×10^{-5} to 10^{-4} (max), depending on pre-strain. Copper[17] and aluminum,[16] show a similar behavior to zinc. In this respect, beryllium behaves like α-brass (Meakin and Wilsdorf[20]) in that closed hysteresis loops exist up to the flow stress, and reverse plastic flow occurs with a corresponding shear on the glide plane $\sim 10^{-3}$. The reversible behavior in α-brass is explainable in terms of the compression and relaxation of dislocation pile-ups.

It is important to point out that the friction stress associated with a reverse plastic strain $\sim 10^{-3}$ is significantly higher than that measured at the low strain amplitudes $\lesssim 5 \times 10^{-5}$. This is apparent from an examination of the plots of loop area versus forward plastic strain at the higher strain amplitudes (Figures 2-3 and 2-8). From the slope of the plot at $\gamma_p = 2 \times 10^{-3}$ in Figure 2-8, $\tau_{f(2)} \simeq 1$ Kg.mm^{-2}. Lawley and Meakin[6]

have shown that a positive intercept on the strain axis, and the correspondingly high friction stress are the result of the onset of a second mechanism controlling plastic flow. Although it might appear reasonable under these circumstances to expect a contribution to the friction stress from elastic interactions, it is not clear how the movement of dislocations against these internal stresses would contribute to the energy dissipated. Since the loops remain closed, the dislocation glide distances have to be shorter than the wavelength of the stress field, and complete recovery of the elastic strain energy should occur on closing the loop. The reversibility of dislocation motion, as evidenced by the closing of the loops, eliminates processes such as dislocation interaction, the dragging of jogs, and dislocation - cell boundary interactions. An increase in the effective friction stress with increasing strain amplitude may be related to a difference in the mobilities of edge and screw components. The predominance of edge pairs on the basal plane after simple tension indicates that the screws move more easily than the edge components.

(3) Tensile and Cyclic Hardening

Comparison of the stress-cumulative strain curves in Figure 2-6 makes it clear that cyclic loading effectively eliminates any region of easy glide (Stage I). It is interesting to note that the work-hardening slope in cyclic compression in the cumulative glide range 0.1 to 0.4 $\left(\frac{d\tau}{d\gamma} \simeq 1.5 \text{ Kg.mm}^{-2}\right)$ is the same as that for simple tension[15] in Stage II at glide strains in the range 1.6 to 2.

The existence of long edge dislocation pairs and edge dislocation dipoles in Stage I in simple tension may be explained[15] on the basis that screw dislocations gliding on the basal plane in the easy glide region have considerably more ductility than edge components, and can readily glide out of the crystal, leaving the edge dislocations. Dipole formation involves some form of cross-slip mechanism for the screw component; Damiano and Herman[15] consider the model proposed by Segall[21] to be applicable. At the limit of Stage I, the edge dislocations are arranged in groups or packets, and with further increase in density, interaction takes place between the gliding edge dislocations and there is an associated increase in the flow stress. Even at the limit of Stage I, the deformation is

extremely inhomogeneous. The dislocation density within the groups of edge dislocations approaches 10^{10} cm.cm^{-3}, but the spacing between individual groups is still several microns.

The elimination of Stage I of easy glide in cyclic compression, the higher flow stress, and the uniform dislocation substructure on the (0001) plane (Figure 9(a)) can be rationalized in terms of the behavior of the screw dislocations. On cycling at a glide strain amplitude 0.008, most of the mobile dislocations remain in the crystal; the successive forward and reverse motion enhances the probability of cross slip of the screw components. The continued forward-reverse motion of the screws then requires additional energy either to create point-defects in the case of small jogs, or in creating trails of edge dislocations behind large jogs. The substructure shown in Figure 9(a) is in accord with this proposed mechanism in that elongated dislocation loops are present having a direction of elongation along each of the three $\langle 10\bar{1}0\rangle$ direction in the basal plane normal to each of the three possible 1/3 $\langle 11\bar{2}0\rangle$ Burgers vectors. Also consistent is the form of the dislocation substructure seen on the $(01\bar{1}0)$ prism plane (Figure 9(b)) with the basal plane perpendicular to the plane of the foil. The wavy character of the screw dislocations running in the $[\bar{2}110]$ direction is a result of cross slip of screw segments to and from the basal plane onto the $(01\bar{1}0)$ prism plane.

V. SUMMARY

(i) The friction stress τ_f for basal slip in beryllium is low and in the range 0.02 to 0.13 $Kg.mm^{-2}$, with no dependence on prestrain. This is the stress associated with closed hysteresis loops giving rise to plastic strains amplitudes $\lesssim 5 \times 10^{-5}$.

(ii) A large fraction of τ_f is due to dislocation-impurity interactions so that the actual lattice friction on the basal plane is extremely low.

(iii) Closed hysteresis loops can be traced at stress amplitudes up to the macroscopic flow stress level; the corresponding plastic strain amplitudes are as high as 2×10^{-3}. The anelastic behavior at these strain amplitudes is associated with a second and higher friction stress $\tau_{f(2)} \sim 1$ $Kg.mm^{-2}$.

(iv) Cyclic hardening effectively eliminates any region of easy glide (Stage I) and gives a work-hardening rate comparable with that in Stage II under tensile deformation.

(v) The increase in stress level in cyclic compression, and the independence of τ_f on prestrain, can be understood from a study of the associated dislocation substructures.

REFERENCES

1. W. Bonfield, J. A. Sartell, and C. H. Li, Trans. AIME. 227, 669 (1963).

2. W. Bonfield and C. H. Li, Acta Met., 11, 585 (1963).

3. W. Bonfield and C. H. Li, Acta Met., 12, 577 (1964).

4. C. Ruckman and J. S. White, Int. Conference on the Metallurgy of Beryllium, Grenoble, France, May 1965.

5. W. Bonfield and C. H. Li, Acta Met., 13, 317 (1965).

6. A. Lawley and J. D. Meakin, Acta Met., in press.

7. H. G. F. Wilsdorf, and F. Wilhelm, Conference on Metallurgy of Beryllium, Inst. of Metals, London p. 68 (1961).

8. F. Wilhelm and H. G. F. Wilsdorf, ASD-TDR-509, 4, 1964.

9. G. E. Spangler, M. Herman, and E. J. Arndt, Bureau Naval Weapons, Contract Now 61-0221-d (1961).

10. J. F. Smith, and C. L. Arbogast, Journal Appl. Physics, 31, 99 (1960).

11. A. H. Cottrell, Dislocations and Plastic Flow in Crystals, Claredon Press, Oxford, p. 111 (1953).

12. J. M. Roberts, and N. Brown, Trans. AIME, 218, 454 (1960).

13. G. E. Spangler, M. Herman, E. J. Arndt, D. B. Hoover, V. V. Damiano, G. W. Tint, and C. H. Lee, Franklin Institute Final Report F-B1933, 1962.

14. G. J. London, and M. Herman, Int. Conference on the Metallurgy of Beryllium, Grenoble, France, May 1965.

15. V. V. Damiano and M. Herman, Int. Conference on Beryllium Tech., AIME, Phila., Pa., October (1964).

16. K. U. Snowden, Acta Met. 11, 675 (1963).

17. A. Lawley, J. D. Meakin, and K. U. Snowden, ARL 65-11, January (1965).

18. H. Conrad, Int. Conference on the Metallurgy of Beryllium Grenoble, France, May 1965.

19. R. L. Fleischer and W. R. Hibbard, Jr., NPL Conference on The Relation Between the Structure and Mechanical Properties of Metals, London HMSO. p. 262 (1963).

20. J. D. Meakin and H. G. F. Wilsdorf, Trans. AIME, 218, 745 (1960).

21. R. L. Segall, Electron Microscopy and Strength of Crystals (New York - Interscience) 515 (1963).

SECTION III

THE EFFECT OF THERMAL, MECHANICAL, AND SURFACE TREATMENTS ON THE FLOW AND FRACTURE OF BERYLLIUM

ABSTRACT

The tensile microstrain, macroscopic flow, and fracture characteristics of polycrystalline QMV-N50 hot-pressed beryllium have been studied after various thermal, mechanical, and surface treatments. Mechanical property data presented refer to the influence of: surface deformation produced by spraying with carborundum powder, strain cycling, grease-coatings. and evaporated or electrodeposited metal layers. In addition, the associated dislocation substructures have been characterized using transmission electron microscopy. These treatments do not give rise to any marked changes in strength or ductility relative to the annealed condition. Annealing in the range 750°C to 850°C increased the ductility by a factor of two compared with the as-received condition, with little detriment to the strength. The frictional stress resisting the movement of dislocations is $\simeq 1.2$ Kg mm^{-2}, and is relatively insensitive to prestrain or surface treatment. The microscopic yield stress (at a strain of 2×10^{-6}) decreases from 8 Kg mm^{-2} to 1.7 Kg mm^{-2} on annealing. Dislocations are present in both simple and complex arrangements. Prominent features include subboundaries, dipoles, groups of dislocations confined to one slip plane, heavily jogged dislocations, and dislocations anchored at inclusions.

I. INTRODUCTION

Under specific conditions of loading and orientation, beryllium may be considered as a ductile metal. In general, however, the use of beryllium as a structural material is severely limited by the brittleness problem. In much of the work on brittle materials, there is evidence to show that the operation of surface sources plays an important role in the deformation process leading to fracture[1]. A theoretical consideration of the constraints on dislocations at and near to the surface[2] suggests that the experimental observations may in some cases be accounted for by the ease of operation of dislocation sources near the specimen surface compared to those in the interior. Gilman and Johnson[3] found that LiF crystals sprinkled with 100 mesh carborandum particles could be bent more easily and uniformly than crystals in which the surface defects were removed by polishing. Similarly, Stokes, Johnson and Li[4], observed that the flow and fracture behavior of chemically polished MgO crystals were influenced strongly by the density and distribution of slip at the start of plastic flow. Very fine slip either stabilized cracks at a size below the limits of resolution of optical microscopy, or modified the usual crack nucleation process. It was found that when the density of slip was increased by injecting dislocation sources into the crystal by sprinkling with carborundum particles before loading, such crystals were always ductile in tension.

This phase of the program is concerned with a comparative evaluation of the microstrain, plastic flow, and fracture behavior of polycrystalline hot-pressed beryllium after various thermal, mechanical, and surface treatments. The latter include grease coatings, evaporated and electrodeposited metal films, surface deformation by particle spraying, strain cycling and fatigue cycling. As an integral part of the evaluation, the associated material substructures have been characterized by transmission electron microscopy. In the particular case of commercially pure and secondary refined beryllium, Morrow and Moore[5] obtained an enhancement in ductility from ~ 50% to > 110% by testing overaged material in Cerrobend* at temperatures

*An alloy of lead, tin, bismuth, and cadmium which melts at 80°C.

between 300°C and 450°C. Bonfield et al[6] have shown that the microstrain behavior of hot-pressed QMV material is particularly sensitive to surface condition; a removal of the worked surface layers by chemical polishing resulted in an appreciable increase in the microscopic yield stress. To date, however, there have been no extensive studies of the effect of surface condition on microstrain behavior, flow, and fracture.

II. EXPERIMENTAL PROCEDURE

(i) Material: The starting material was Brush Beryllium QMV-N50 nuclear grade, in the form of 0.250" diameter by 6" long hot-pressed polycrystalline rod. This has a purity ~ 99.3% by weight, with BeO ~ 0.77% by weight, and C ~ 0.10% by weight, as the principal impurities.

(ii) Specimen Preparation: Tensile specimens were cut and shaped from the 0.250" diameter rod by spark-machining. The rods were first cut to 0.140" diameter at the rate of 0.001" of radius per minute using a coarse spark discharge. A final gauge diameter of 0.113" was produced by three equal cuts of 0.009" using succeedingly finer capacitances in the discharge circuit. The final size of the specimens was 0.75" shoulder length and 0.70" gauge length. Specimens were polished electrolytically in a glycerol solution[7] to a depth ~ 0.002" from the outer surface; no twins or cracks were seen when examined at x 500 with an optical microscope.

The specimens were tested in the as-received condition, after vacuum annealing, annealing in argon, after particle spraying, metal-coating, grease-coating, and cyclic deformation. For the annealing treatments, the specimens were wrapped in tantalum foil and sealed in vycor tubes.

Specimens suitable for electron microscopy were prepared by spark-machining thin slices from the tensile specimens. The slices were then electropolished to obtain electron-transparent areas. Difficulties arise in the polishing of this form of beryllium due to the fine grain structure; since optimum conditions for polishing depend strongly on the crystallographic orientation of the beryllium, wide variations exist in

the final thickness of the thin foils. The foils were examined in a Philips 100B electron microscope at 80KV or 100KV.

(iii) Microstrain and Tensile Testing: Comparative microstrain and tensile tests were carried out in a straining jig mounted between the fixed and moving cross-heads of a standard Instron machine, Figure 3-1. This form of specimen holder ensures excellent alignment between the loading axis and the specimen axis, an essential requirement when recording strain to a sensitivity $\sim 2 \times 10^{-6}$. Differential transformers were used to measure the stress through the displacements across a proving ring, and the strain across the gauge length. The changes in output signals of the transformers, corresponding to displacements across the proving ring and the gauge length, were amplified and fed to a Moseley X-Y Recorder; this gave a continuous recording of the stress-strain behavior of the specimen to the point of fracture. A number of strain ranges were available so that the strain sensitivity could be increased to study anelastic effects at different stages of the tensile test.

III. EXPERIMENTAL RESULTS

(i) Microstrain Behavior

Stress-strain characteristics of the hot-pressed beryllium in the microstrain region following various pre-treatments are illustrated in Figure 3-2. The elastic contribution has been subtracted from the total strain in each case. The curves show that an anneal in vacuum at 750°C (2 hours) drastically reduced the micro-yield stress from 8 Kg mm^{-2} to 1.7 Kg mm^{-2}; the corresponding flow stresses at strains $\lesssim 3 \times 10^{-4}$ are also lower. With the sensitivity of strain measurement used in these experiments, the microscopic yield stress may be defined as the stress giving rise to a permanent strain of 2×10^{-6}. These values are in good agreement with those reported by Bonfield and Li[8] for as-received and annealed hot-pressed QMV- beryllium, namely ~ 7 Kg mm^{-2}, and ~ 2 Kg mm^{-2} respectively. Surface sprinkling of annealed material with carborundum powder (mean diameter $\sim 483\mu$) raises the flow stress above that of the as-annealed beryllium. Copper plating

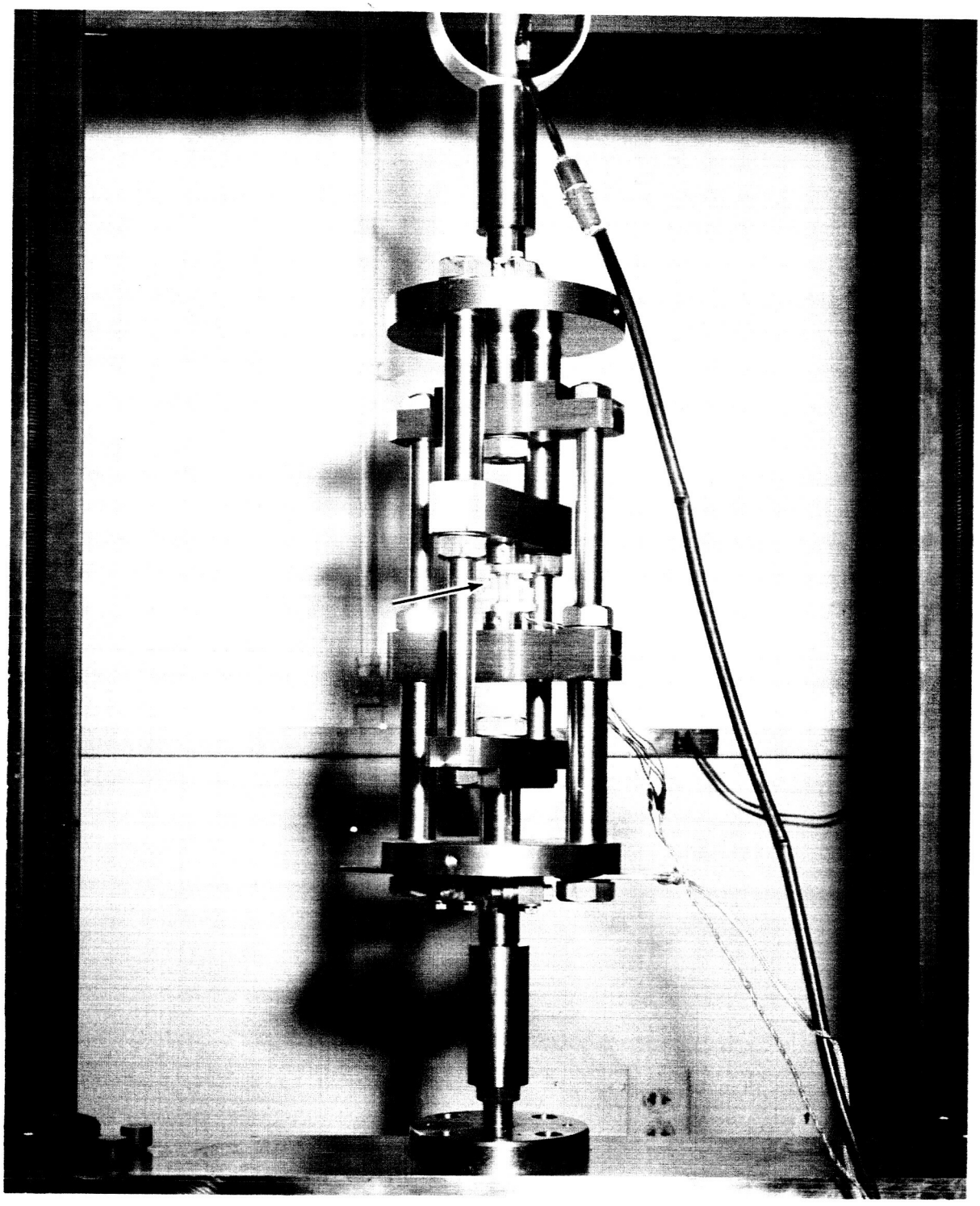

Fig. 3-1 Microstrain jig with specimen in position.

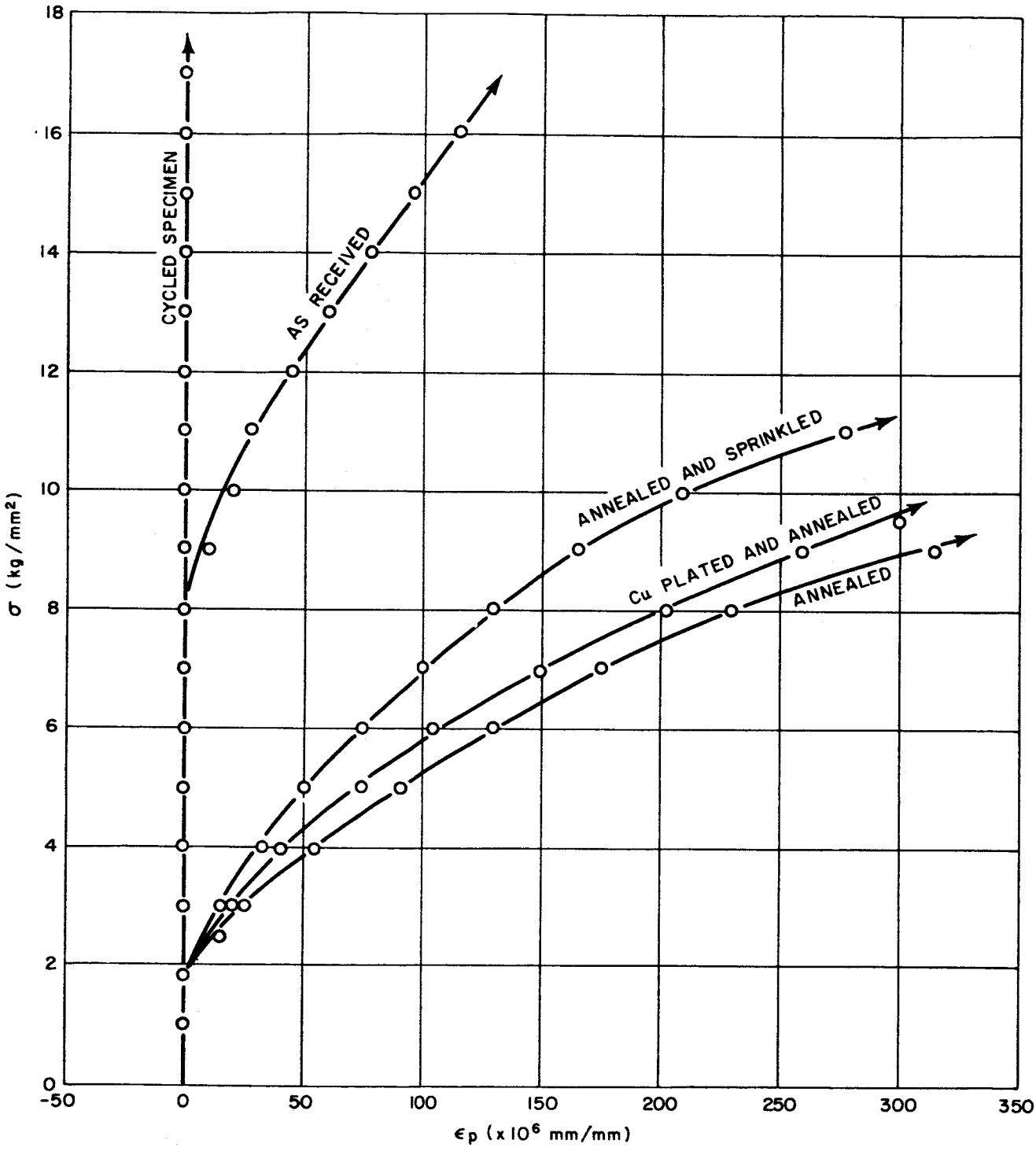

Fig. 3-2 Stress-strain behavior in the microstrain region for QMV-N50 beryllium in the conditions indicated.

has little effect on the stress-strain behavior of the annealed material. In contrast to the effects produced by annealing, sprinkling, or plating, cycling straining prior to tensile testing causes a significant increase in strain-hardening.

The apparent Young's Modulus was determined from the elastic portion of the stress-strain curves near zero stress. The value obtained was 30,000 Kg mm^{-2}, which is in good agreement with the dynamic modulus[9] of 30,100 Kg mm^{-2}.

Measurement of the frictional stress opposing the motion of dislocations is an important parameter, since such measurements provide valuable information on the deformation process, and also assist in the interpretation of transmission electron micrographs. The method of determining the frictional stress has been reported elsewhere[10]. The technique entails use of the microstrain apparatus to measure the irreversible work done in forming anelastic loops such as those shown in Figure 3-3a. These loops were obtained after 0.4% prestrain in a specimen annealed and sprayed with carborundum powder. From the analysis of a closed hysteresis loop, the frictional stress σ_f is given by $\Delta W/2\epsilon_p$ where ΔW is the irreversible work done during each cycle, and ϵ_p is the forward plastic strain. Such a plot is shown in Figure 3-3c. The analysis requires that the line go through the origin, since $\Delta W = 0$ when the forward plastic strain is zero. Thus, the frictional stress is determined from the slope of the straight line of best fit through the origin. Alternatively, the frictional force can be obtained from a plot of stress amplitude against ΔW. In this case, the line intercepts the stress axis at $2\sigma_f$. This represents the stress (σ_E) required to form the first loop, as opposed to an elastic line with $\Delta W = 0$; in the limit, as $\Delta W \rightarrow 0$, $\sigma \rightarrow \sigma_E$ ($\equiv 2\sigma_f$). It is advisable to use both plots; the corresponding stress amplitude - ΔW plot for the sprayed material is given in Figure 3-3b.

The frictional stress values from the plots of Figures 3-3b and 3-3c are 1.1 Kg mm^{-2} and 1.3 Kg mm^{-2} respectively. The various treatments do not give rise to any significant changes in the frictional stress. Pre-strains up to 2.5% do not affect the level of the frictional stress σ_f.

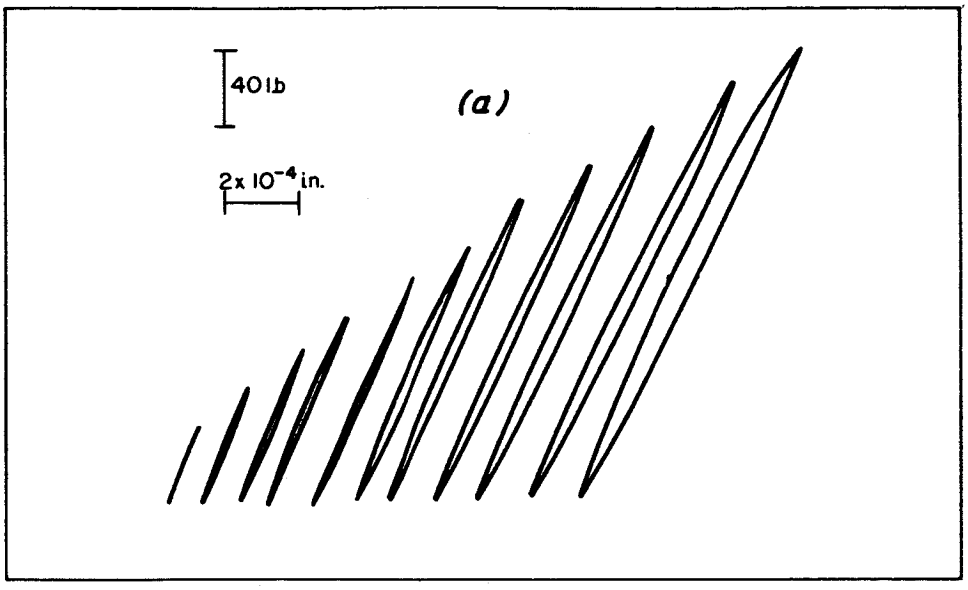

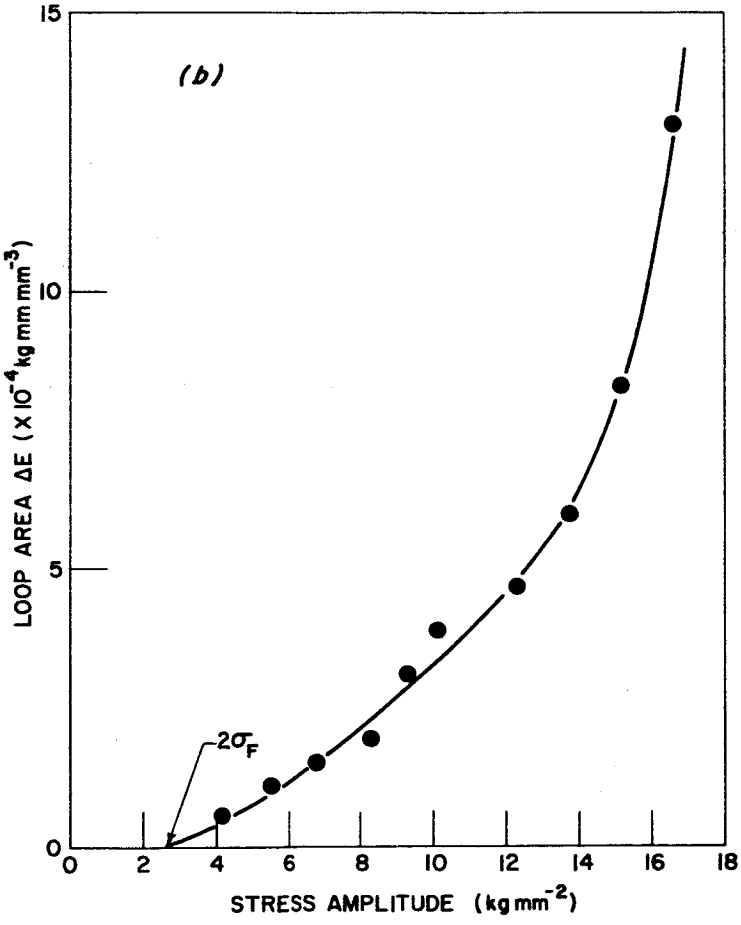

(a) a representative set of anelastic loops,
(b) the irreversible work done as a function of the stress amplitude,

Fig. 3-3 Measurement of the frictional stress σ_f.

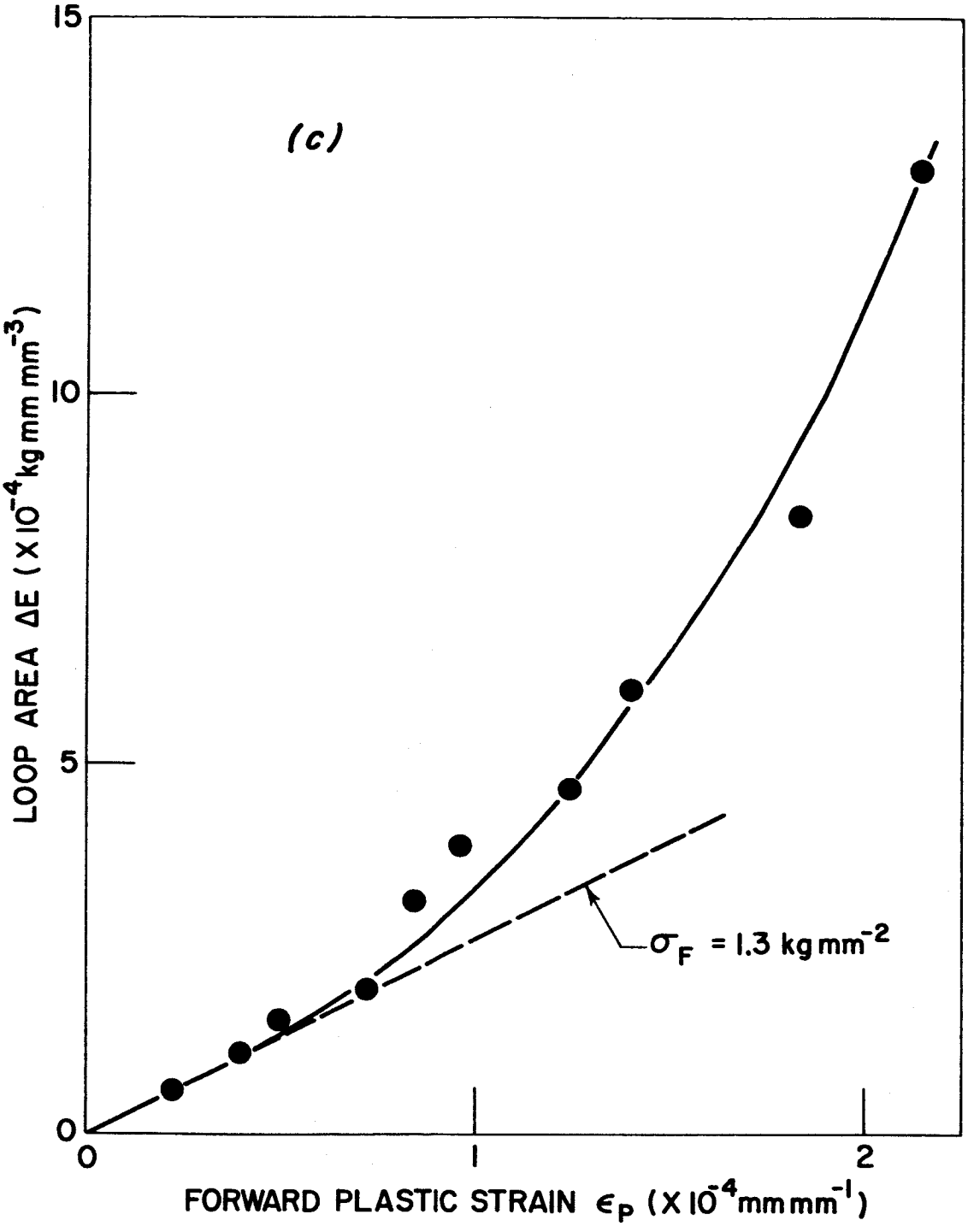

(c) the irreversible work done as a function of the forward plastic strain. Specimen annealed and sprayed with carborundum powder.

Fig. 3-3 Measurement of the frictional stress σ_f.

(ii) Macroscopic Flow and Fracture

In terms of strength and ductility the reasoning and objectives behind the various annealing and surface treatments can be summarized as follows: (a) the production of a uniform density of mobile dislocations (b) a strengthening of the specimen by 'straightening' the surface which is believed to provide most of the dislocations during the initial stages of deformation (c) protection of the surface from contamination by atmospheric gases during deformation.

The effect of specimen condition of the stress and strain at fracture is illustrated schematically in Figure 3-4. The data refer to two separate shipments (batches A and B) of hot-pressed QMV-N50 beryllium; for purposes of comparison, values are included for vacuum-annealed (900°C) secondary refined Pechiney beryllium. The specific treatments, and the corresponding levels of stress and strain at fracture, are compiled in Table 3-1. The data in Table 3-1 and Figure 3-4 show that the fracture stress of specimens prepared from batch B tended to be systematically higher than that of the corresponding specimens from batch A.

The general form of the stress-strain curves to fracture in each of the various conditions is given in Figures 3-5 to 3-8. It is clear that annealing the as-received beryllium either in argon or in vacuum in the range 750 to 850°C doubles the ductility with only a small reduction in the stress at fracture. The stress-strain curves for the specimen annealed in argon closely follows that for the specimen annealed in vacuum. Examination of the fractured specimens by optical microscopy revealed the presence of a large number of cracks, such as shown in Figures 3-9 and 3-10 for the as-received and the strain cycled specimens, respectively. The influence of the various treatments is now considered in more detail.

(a) Cyclic Straining: Alden[11] has suggested that the mechanical properties of MgO crystals, which have been hardened progressively by cyclic straining, are greatly superior to those of the as-received material. It therefore appeared warranted to apply similar cyclic loading increments to beryllium. An annealed polycrystalline specimen was subjected to slow cycles ($\sim$ 1 cycle min^{-1}) of constant plastic strain increasing from

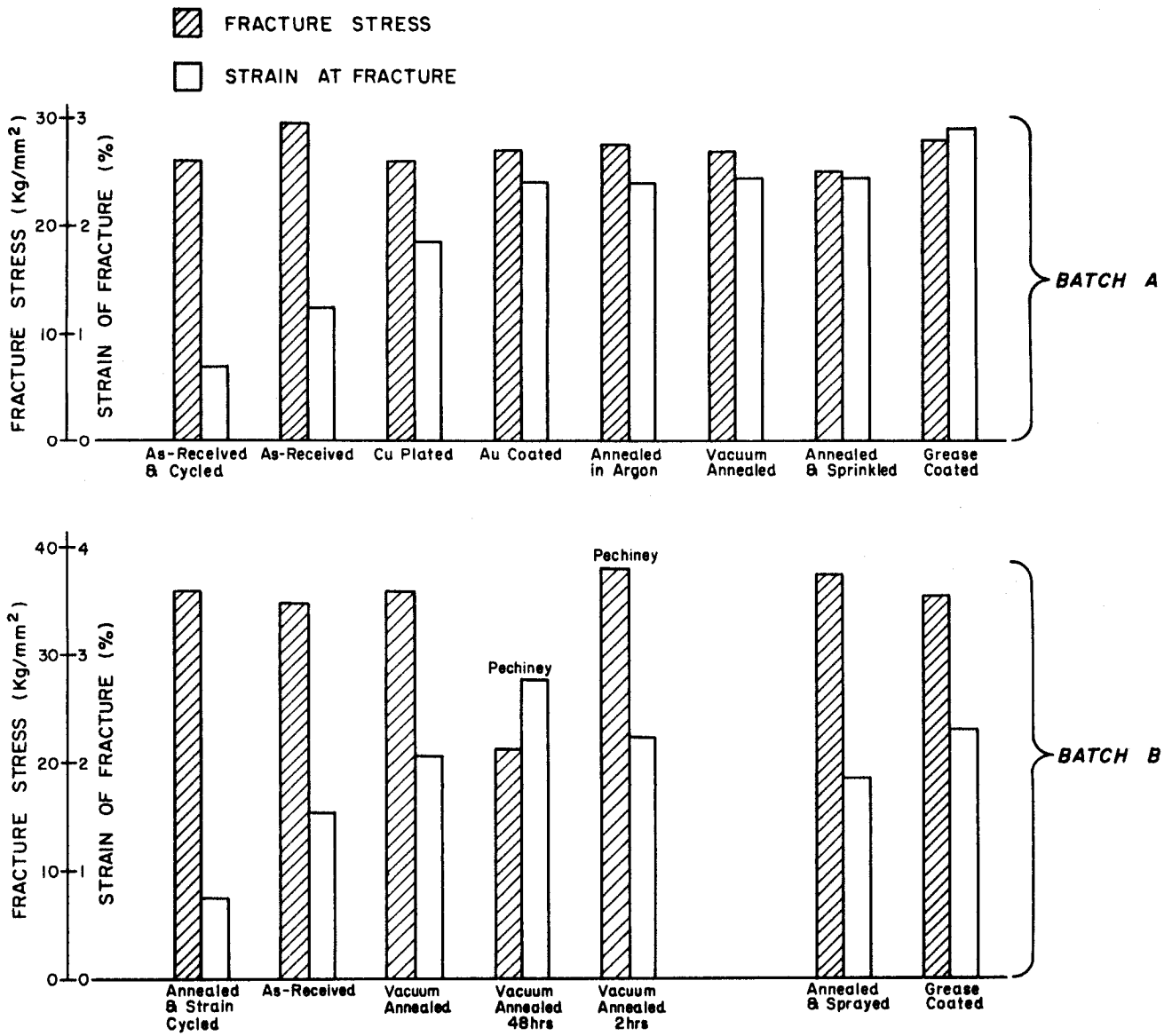

Fig. 3-4 Effect of specimen condition on the stress and strain at fracture of two batches of hot-pressed QMV-N50, and secondary refined Pechiney beryllium.

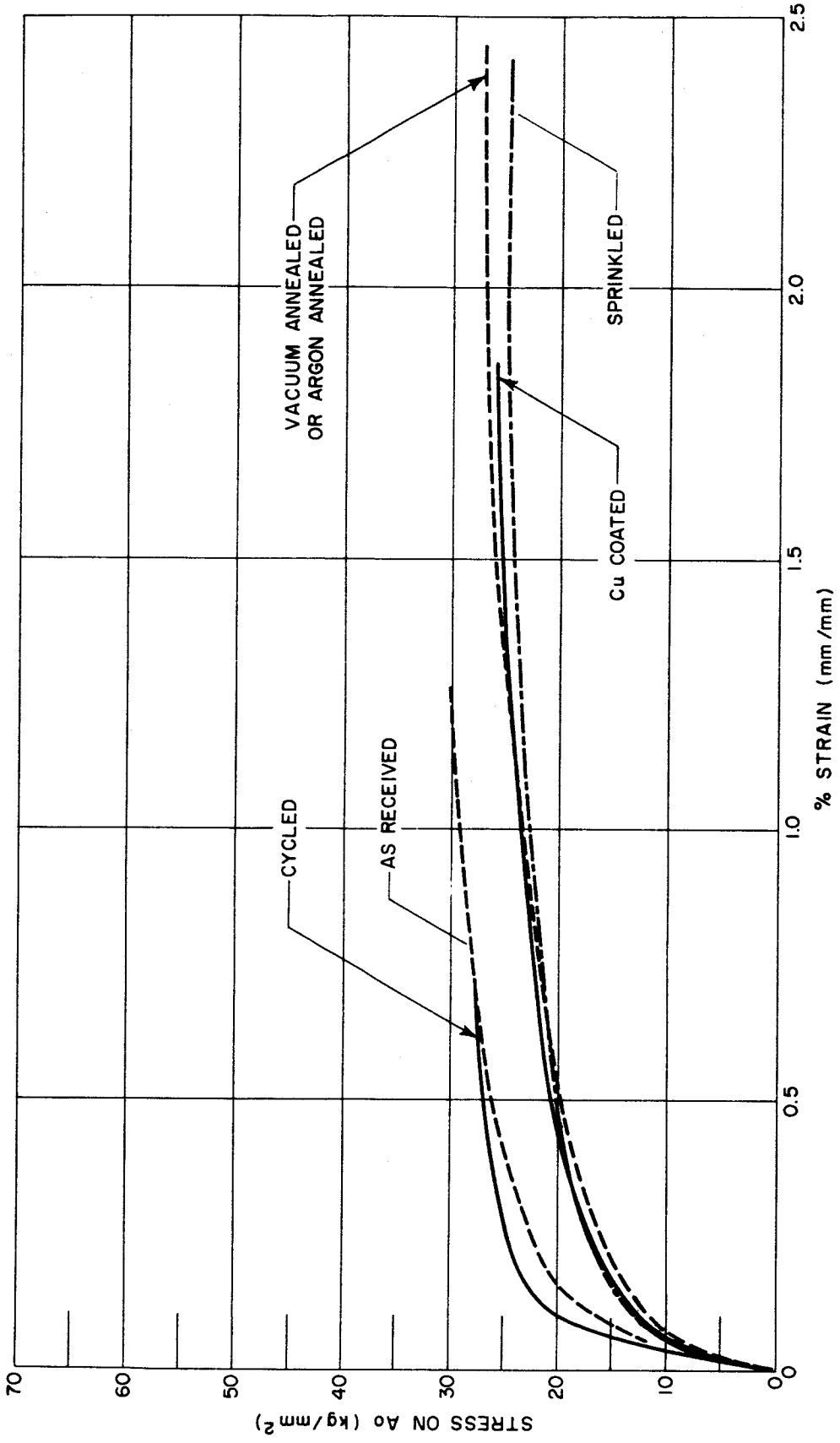

Fig. 3-5 Stress-strain curves to fracture for material in the conditions indicated.

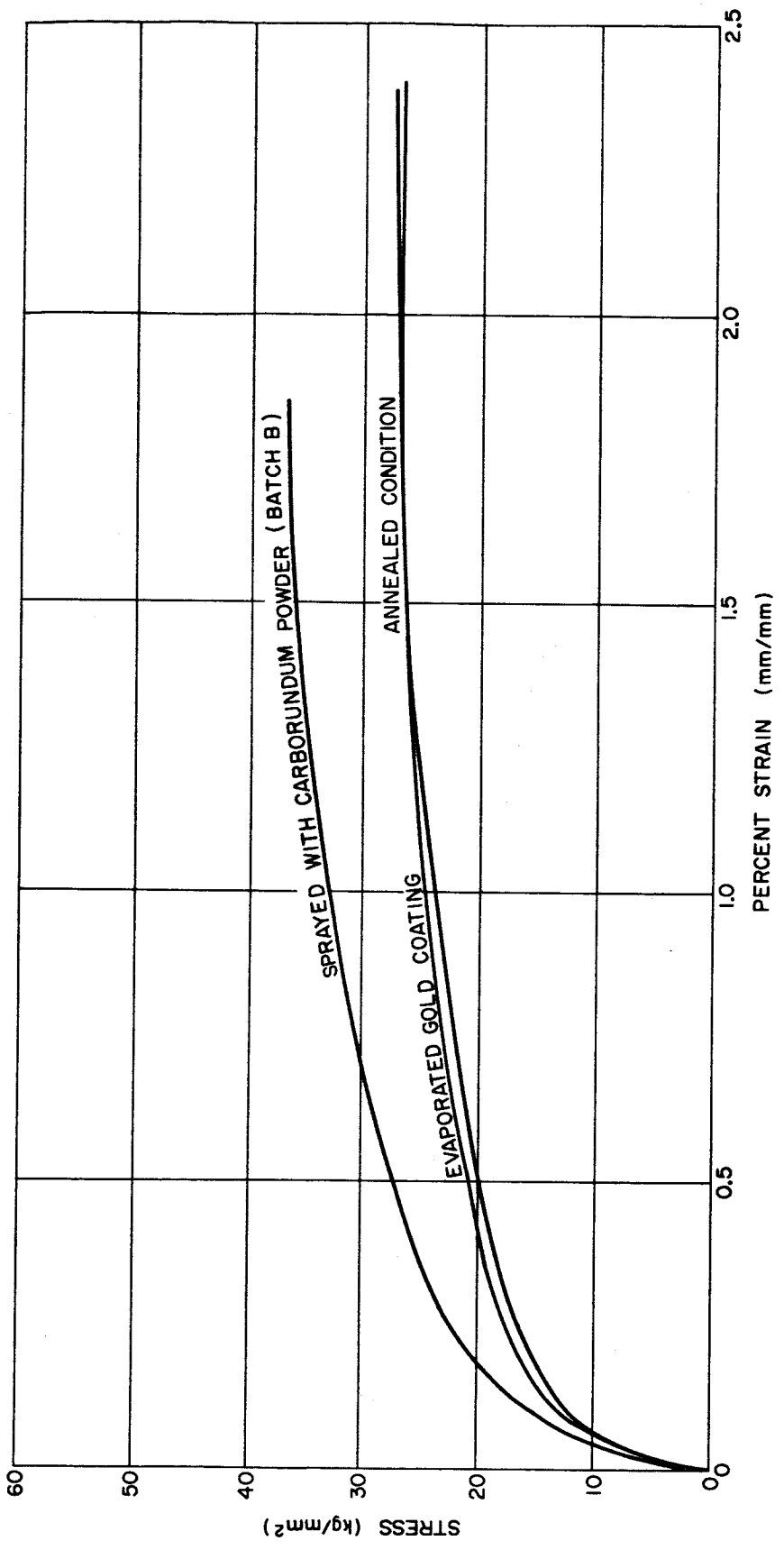

Fig. 3-6 Stress-strain curves to fracture for material in the conditions indicated.

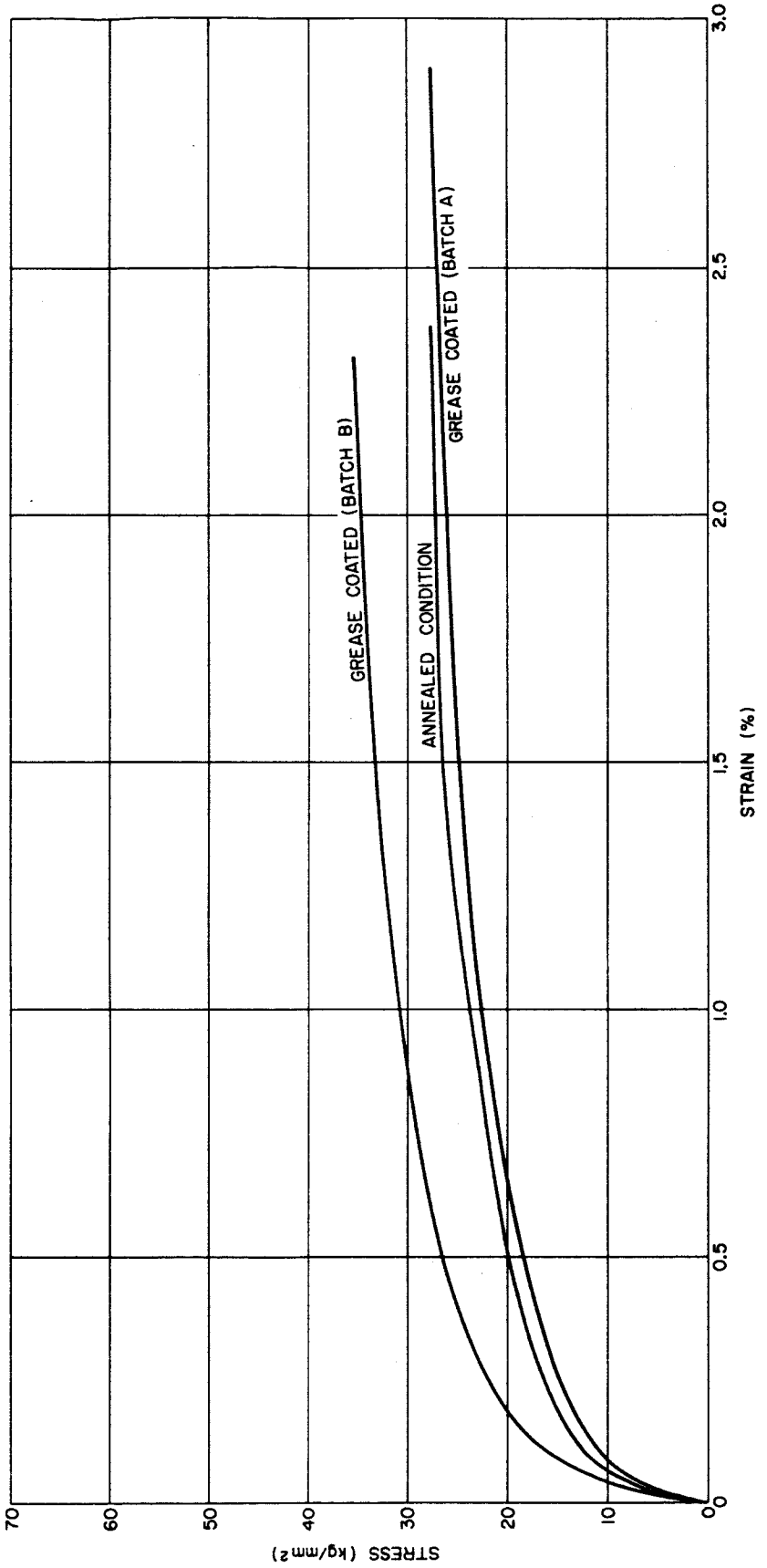

Fig. 3-7 Effect of grease coating on the stress-strain curve to fracture.

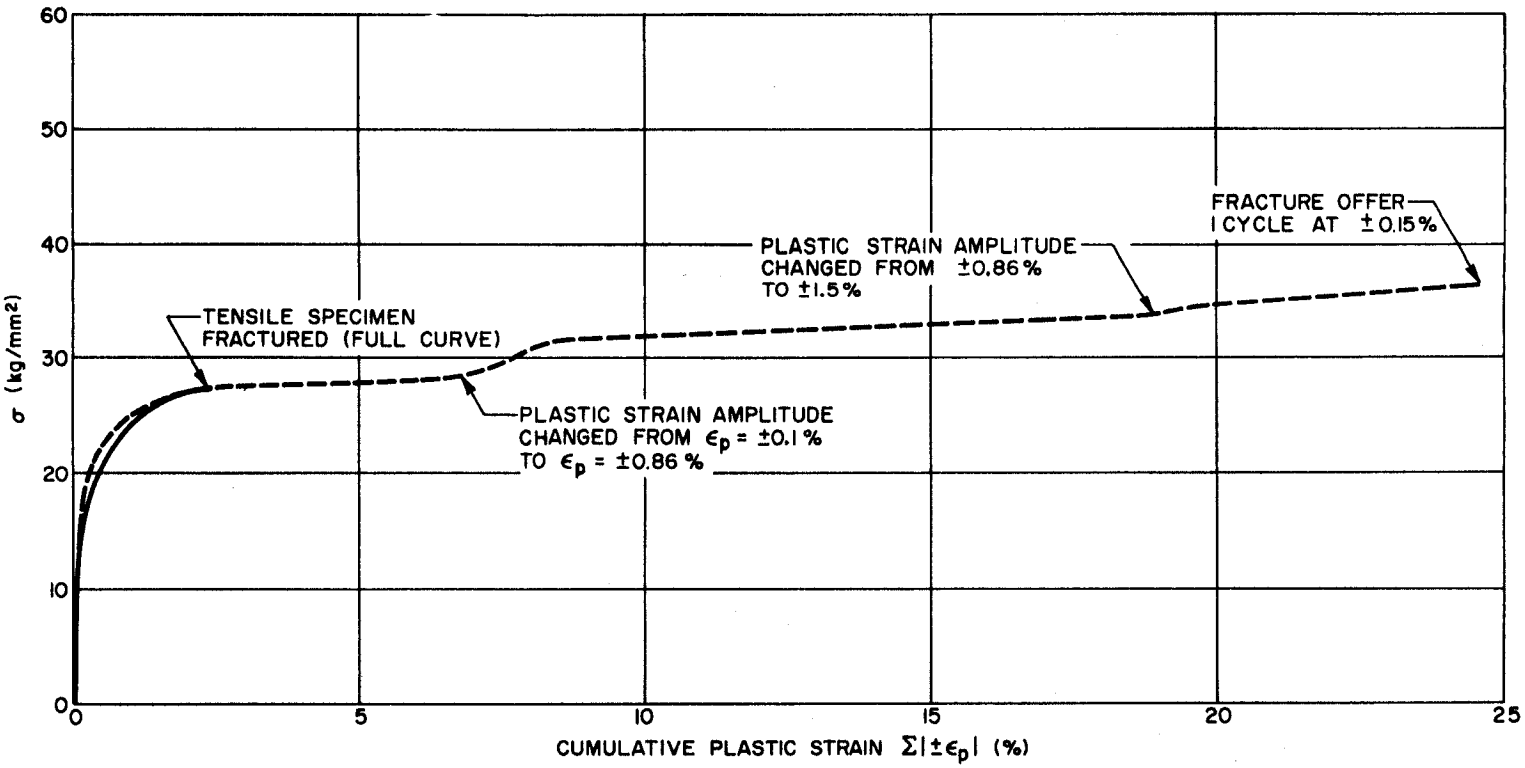

Fig. 3-8 Tensile and cyclic hardening curves for specimens in the annealed condition.

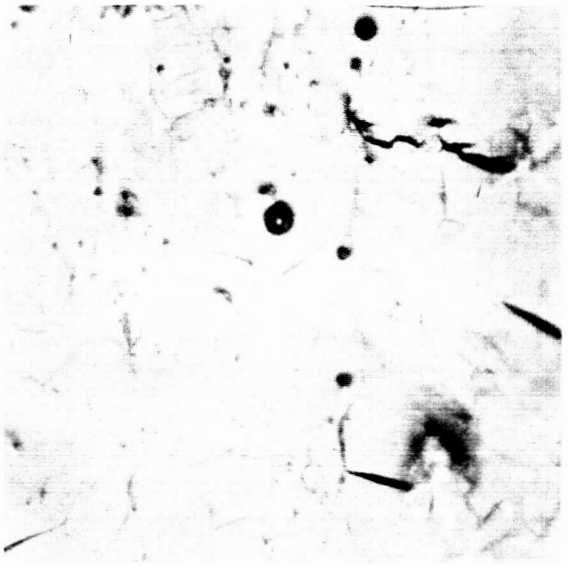

Fig. 3-9 The fracture surface of the as-received material. X250.

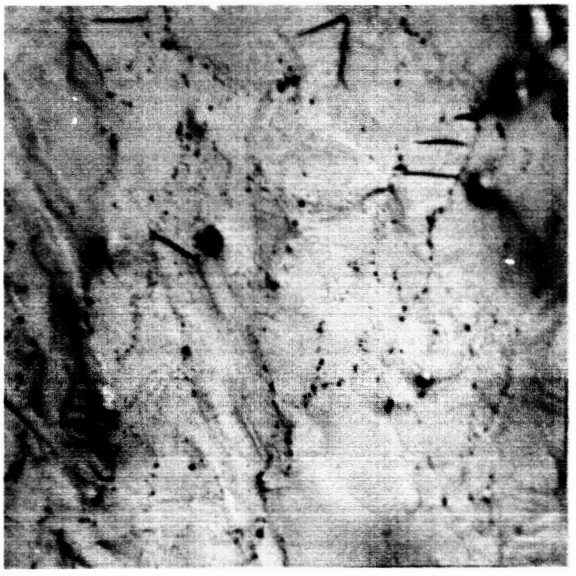

Fig. 3-10 The fracture surface of the material which had been strain cycled prior to testing. X500.

Table 3-1

THE EFFECT OF SPECIMEN CONDITION ON THE STRESS AND STRAIN AT FRACTURE

Specimen Condition	Stress at Fracture Kg mm^{-2}	Strain at Fracture Kg mm^{-2}
As-received	29.5	1.25
Vacuum annealed at 750°C	27.0	2.45
Annealed in argon at 850°C	27.5	2.40
Vacuum annealed and sprayed with carborundum powder	25.0 Batch A 37.0 Batch B	2.45 1.85
Annealed in argon, copper plated, and re-annealed in argon at 850°C	26.0	1.85
Annealed in Argon, gold film evaporated, re-annealed in argon at 850°C	27.0	2.4
As-received, then strain-cycled successively at plastic strain amplitudes of $\pm$ 0.10%, $\pm$ 0.86%, and $\pm$ 1.5%	26.5	0.70
Annealed in argon at 850°C, then strain cycled as above	36.0	0.75
Annealed in argon at 850°C, and coated with 'vaseline'	28.0 Batch A 36.5 Batch B	2.90 2.30

$\epsilon_p = \pm$ 0.1% to $\pm$ 1.5% with an intermediate strain-amplitude change at ϵ_p = 0.86%, Figure 3-8. In the subsequent tensile test, the specimens exhibited a high initial rate of hardening which then dropped to a low value. Each change in strain amplitude produced a sharp increase in peak stress which was followed rapidly by a saturation in the hardening rate. The fracture stress was not significantly different to that of the other specimens of the same batch, while the strain at fracture of 0.75% was smaller than that of the specimens which had not been cycled. Strain cycling of the as-received beryllium produced similar effects, Figure 3-5.

(b) Surface Spraying with Carborundum Particles: In the first experiment, the specimen was annealed in vacuum at 850°C and then sprayed with carborundum powder (average particle size 483μ) from a height of 1". The overall effect on the stress-strain curve, compared with the annealed condition, was small, Figure 3-5. On the assumption that this treatment produced only a small change in the number of mobile dislocations at the surface, a second annealed specimen (batch B) was sprayed with carborundum powder (average particle size 483μ) from a gun using compressed argon.

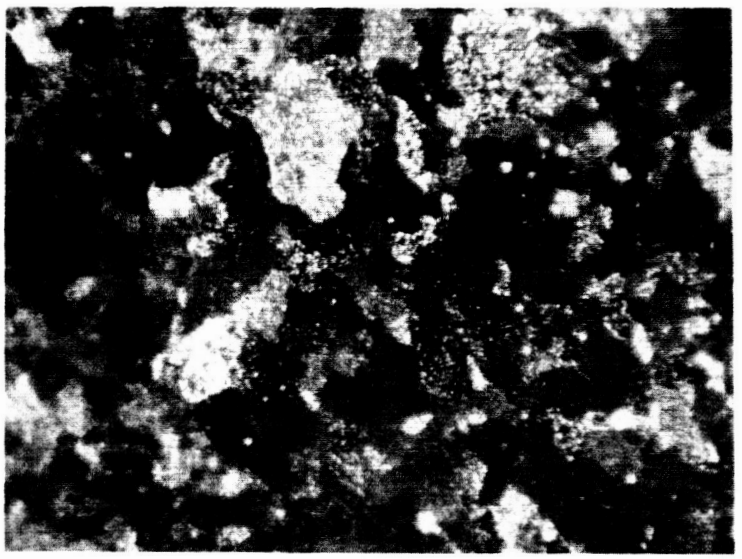

Fig. 3-11 Surface of specimen sprayed with carborundum particles under pressure. X375.

This treatment was sufficient to produce fine surface indentations, Figure 3-11; although the flow stress was significantly greater than that of the annealed material, the strain at fracture decreased from 2.45% to 1.85%, Figure 3-6.

(c) Grease Coatings: In order to determine whether beryllium is susceptible to atmospheric corrosion during deformation, two annealed specimens (from batches A and B) were coated with 'vaseline' grease and pulled to fracture. According to Snowden[12], this form of coating is expected to reduce the partial pressure of oxygen at the surface of the metal to less than 10^{-3} torr; in turn, this will affect the rate of propagation of small cracks during the time of test, provided the metal is prone to corrosion by atmospheric gases.

The stress-strain curves to fracture are given in Figure 3-7. Strain at fracture for the grease coated specimen from batch A was 20% higher than that of uncoated annealed material. The coated specimen from batch B had a ductility less than the specimen from batch A, but was appreciably more ductile than the other specimens from the same batch.

(d) Metal Coatings: The stress-strain curve for the copper-plated specimen followed closely that of the as-annealed material except that fracture occurred at a lower strain, Figure 3-5. The influence of an evaporated gold film on the stress and strain at fracture was determined after the coated specimen had been annealed at 850°C. As in the case of electrodeposited copper, the stress-strain curve was very similar to that of uncoated beryllium in the annealed condition, Figure 3-6.

(iii) Electron Microscope Observations of Dislocations and Precipitates

Micrographs of the tensile strained as-received beryllium reveal numerous precipitates of irregular and sometimes hexagonal shape, with an average diameter $\sim$ 2000Å. These precipitates tend to lie along grain or subgrain boundaries. The dislocation substructure is markedly irregular, but is characterized by small regions $\lesssim 1\mu$ in diameter which give rise to phase contrast with respect to the grain lattice, Figure 3-12. These regions are often seen to be bordered by bands of irregular dislocations. Dislocation tangling is observed, and in some areas, long straight dislocations are seen to terminate at grain boundaries, Figure 3-13. Sharp kinks and dislocations drawn out into dipoles are also visible.

A similar dislocation substructure and distribution of precipitates is observed in the specimen which had been strain-cycled before tensile straining. Low angle boundaries are present where dislocations appear in sharp contrast at specific areas of the micrograph, but which fade out at others, Figure 3-14. Regions with tangled dislocations and prismatic loops are present as well as areas showing only short isolated dislocations, Figures 3-15 and 3-16.

The dislocation configuration in annealed and deformed beryllium is illustrated in Figure 3-17. In the micrograph, the plane of the transmission foil is perpendicular to the tensile axis. Many parallel dislocations appear in pairs of opposite sign, a fact deduced from their contrast effects. On the basis of comparison with observations on single crystals, it is assumed that these dislocations have a predominantly edge character. In areas such as that illustrated in Figure 3-17, the dislocation density approaches 1.5×10^{10} cm.cm^{-3}. The appearance of long parallel dislocations is restricted

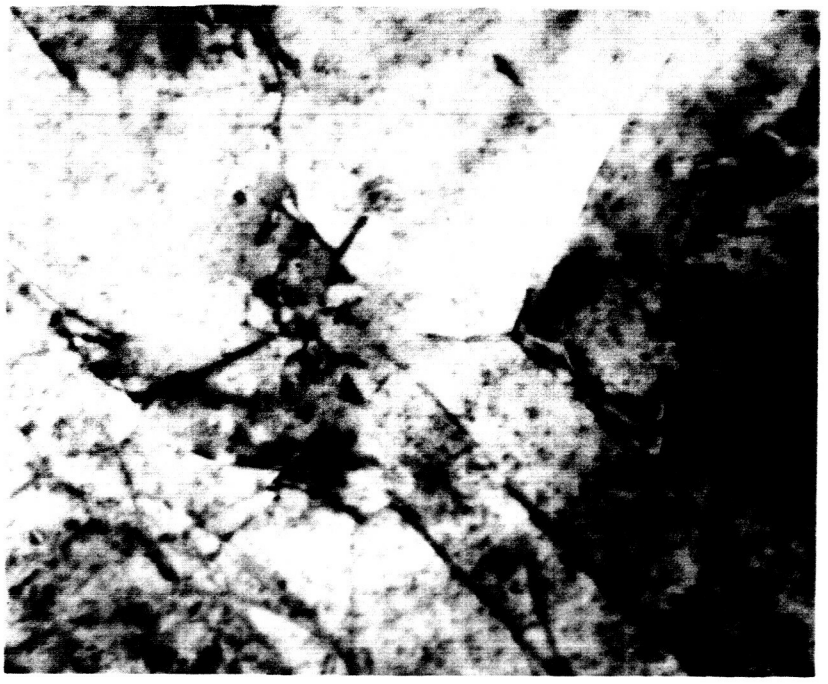

Fig. 3-12 Dislocation configurations in tensile strained as-received beryllium, 40,000: 1

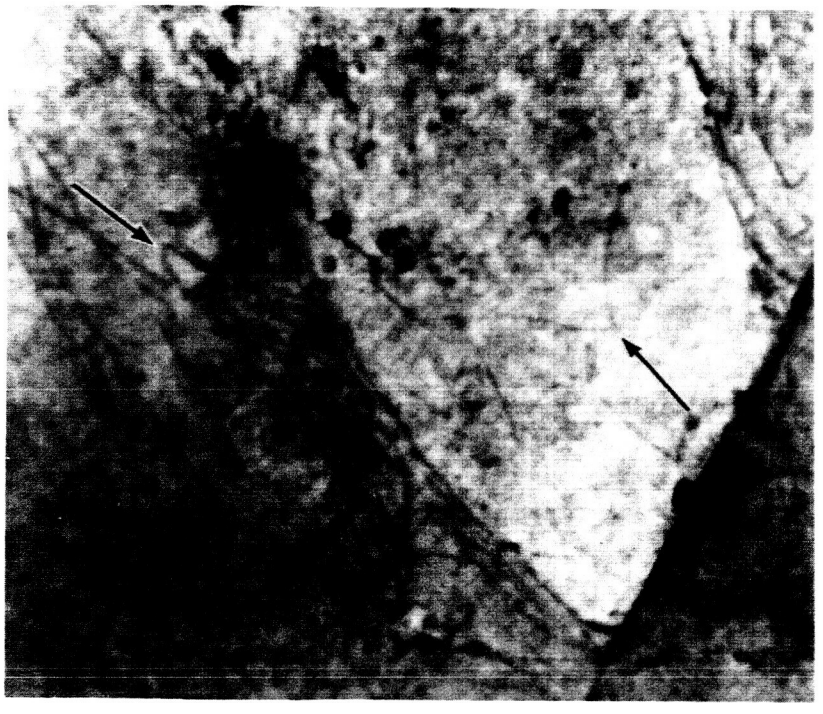

Fig. 3-13 Tensile strained as-received beryllium. Long straight dislocations terminating at a subboundary. Kinked dislocations are arrowed. 40,000: 1

Fig. 3-14 Low angle boundaries (arrowed) and small regions giving rise to contrast effects. Specimen strain-cycled prior to tensile straining. 40,000: 1

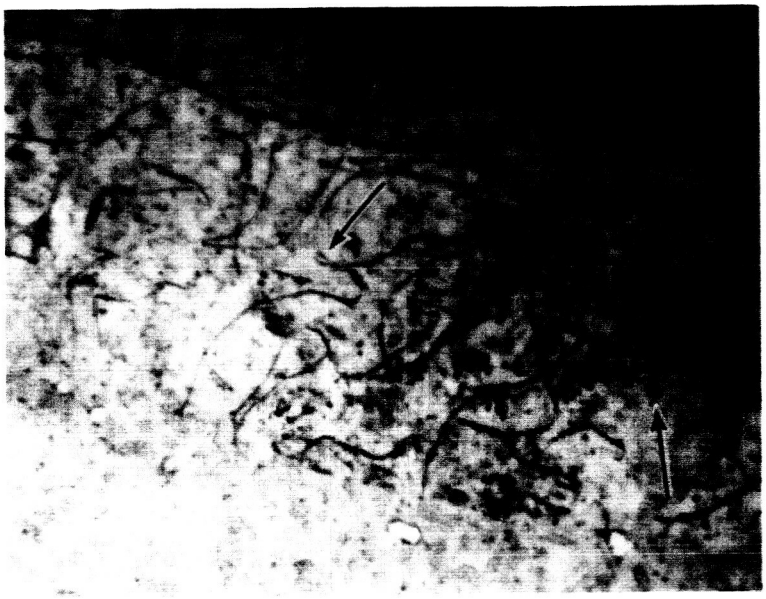

Fig. 3-15 Dislocation tangles and dislocation loops (arrowed). Specimen strain-cycled prior to tensile straining. 40,000: 1

Fig. 3-16 Short isolated dislocations in specimen strain-cycled prior to tensile straining. 40,000: 1

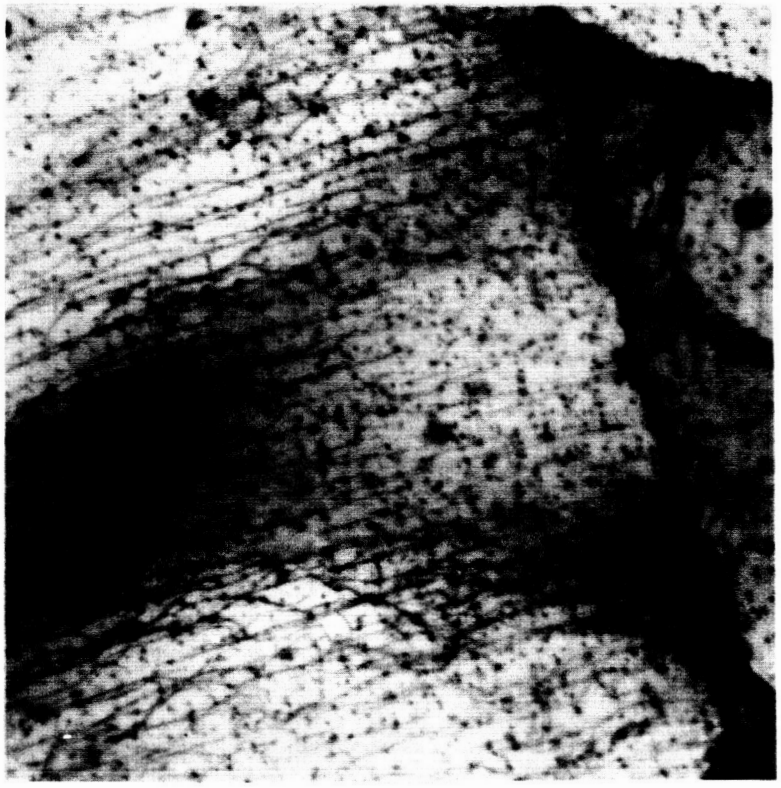

Fig. 3-17 Long parallel dislocation-pairs in annealed and deformed beryllium. 40,000: 1

to specimens having had a prior anneal. The pinning of dislocations (and the associated increase in flow stress) appears to be less effective in these areas. Low angle boundaries are present in the annealed beryllium, Figure 3-18; these may have formed during the annealing process. Tilting of the foil to operate various reflections serves to identify all three Burgers vectors of the type $\langle 11\bar{2}0 \rangle$. The dislocation substructure in the deformed copper-plated and annealed specimen was similar to that of the deformed unplated and annealed specimen.

Fig. 3-18 Rows of dislocations making low angle boundaries (arrowed) in annealed beryllium. 40,000: 1

DISCUSSION

(i) Surface Treatment and Mechanical Properties

The primary concern in this study has been with the influence of the surface condition on the bulk mechanical properties of beryllium. From the initial series of experiments, it would appear that no marked changes in mechanical behavior are brought about, relative to that of the annealed polycrystalline QMV-N50 beryllium. However, any interpretation

of the present results must, of necessity, be of a tentative nature since a minimum number of specimens was tested in each condition. Further, the many variables associated with each surface treatment have not been examined in detail. For example, the effectiveness of an evaporated or electro-deposited layer is dependent on the surface preparation and the degree of cleanliness; it may also be necessary to produce a solid solution alloy with the metal layer at the specimen surface by the appropriate annealing treatments. The twofold increase in ductility brought about by annealing of the hot-pressed beryllium is ascribed to a rearrangement and a decrease in the number of dislocations.

The most significant change in behavior is brought about by a 'vaseline' grease coating. The presence of such a surface coating on annealed QMV-N50 beryllium increased the ductility by a factor ~ 2.3 compared with the uncoated as-received condition. This is considered to be an area worthy of further examination.

(ii) Microstrain Behavior

The frictional stress σ_f resisting the motion of dislocations in the annealed material is $\simeq 1.2$ Kg mm^{-2}, and is relatively insensitive to prestrain and prior surface treatment. This level of frictional stress is in reasonable agreement with that recently reported by Bonfield and Li[13] for annealed QMV-N50 Beryllium, namely σ_f in the range 0.3 Kg mm^{-2} to 1.1 Kg mm^{-2} for prestrains up to 5×10^{-5}. It is impossible to say if the current frictional stress values are significantly higher than those of Bonfield and Li. On the one hand, differences in heat treatment will affect the frictional stress through differences in dislocation substructure and/or impurity distribution. However, it has to be remembered that significant variations in mechanical behavior are found from batch to batch of QMV-N50 Beryllium, and these may be sufficiently large as to mask any true effect.

These levels for the frictional stress in polycrystalline beryllium are comparable with those reported for several other metals. Typical frictional stresses for single crystal copper[14], aluminum[10], and molybdenum[15] are 0.10 Kg mm^{-2}, 0.035 Kg mm^{-2}, and 0.2 Kg mm^{-2} respectively; for polycrystalline zone-refined iron[16] the value is 2.1 Kg mm^{-2}.

Whereas the frictional stress relates to the initiation of dislocation motion, the microscopic yield stress represents a later stage of deformation at which some dislocations have moved relatively large distances within grains, in order to produce strains $\gtrsim 2 \times 10^{-6}$. In the annealed beryllium, the frictional stress is ~ 1.2 Kg mm^{-2} while the microscopic yield stress (at a strain of 2×10^{-6}) is ~ 1.7 Kg mm^{-2}. The microscopic yield stress of the as-received hot pressed beryllium is 8 Kg mm^{-2}, the higher stress level being attributed to the higher background density of dislocations which cause an increased resistance to the motion of glide dislocations.

(iii) Transmission Electron Microscopy

From the limited number of observations made it is difficult to draw conclusions as to the specific dislocation pattern characteristic of a given treatment. These and earlier investigations on beryllium serve to show that the distribution of dislocations is extremely inhomogeneous. Furthermore, since electron diffraction patterns were not available for the foils studied, the crystallographic orientation of the individual grains is not known. The marked differences in dislocations substructure from grain to grain may simply be due to differences in orientation. The long straight dislocations are attributed to a/3 $[11\bar{2}0]$ (0001) glide systems; a series of short isolated dislocations lying in one main direction would correspond to an equivalent glide system, with the basal slip plane and slip direction inclined to the plane of the foil. Brittle fracture in beryllium is believed to be associated with basal plane cleavage due to bend plane splitting[17]. The presence of groups of relatively long dislocation segments, and their interaction with sub-boundaries and inclusions, may be a manifestation of the initiation of bend plane splitting.

SUMMARY

(a) Surface damage introduced by sprinkling or cyclic loading, and surface coatings of grease, electroplated or evaporated metal, produce only slight changes in the stress-strain curve relative to that of the annealed material.

(b) The frictional stress resisting the movement of dislocations is 1.2 kg. mm^{-2}. Prestrain and surface treatment do not affect the level of the frictional stress.

(c) The distribution of the dislocations is extremely inhomogeneous. Prominent features include subboundaries, dipoles, groups of dislocations confined to one slip plane, heavily jogged dislocations, and dislocations anchored at inclusions in the matrix.

REFERENCES

1. T. Suzuki, Dislocations and Mechanical Properties of Crystals, John Wiley and Sons, New York, P. 215 (1957)

2. K. Sumino, J. Phys. Soc. Japan, 17, 454 (1962).

3. J. J. Gilman, and W. G. Johnston, Dislocations and Mechanical Properties Of Crystals, John Wiley and Sons, New York, p. 116 (1957).

4. R. J. Stokes, T. L. Johnston, and C. H. Li, Phil. Mag., 6, 9 (1961)

5. F. Morrow and A. Moore, Increased Ductility of Polycrystalline Beryllium Above 300°C Related to Test Environment. UKAEA - AWRE Rep. No. 0-97/63

6. W. Bonfield, J. A. Sartell, and C. H. Li, Trans AIME, 227, 669 (1963).

7. P. Jacquet, Met. Reviews, 1, 2 (1956).

8. W. Bonfield and C. H. Li, Acta Met. 11, 585 (1963).

9. Beryllium in Aerospace Structures, Brush Beryllium Corp., Cleveland, Ohio

10. K. U. Snowden, Acta, Met., 11, 675 (1963)

11. T. Alden, General Elec., Res. Lab. Rep., No. 63-RL-3227M (1963).

12. K. U. Snowden, J. Appl. Phys., 34, 3150 (1963).

13. W. Bonfield and C. H. Li, Acta Met., 13, 317 (1965).

14. K. U. Snowden and H. G. F. Wilsdorf, ARL Report, 63-114, July 1963.

15. A. Lawley and J. D. Meakin, Microstrain in Refractory Metals, Research in Progress, Franklin Inst., 1965.

16. N. Brown and R. A. Ekvall, Acta Met., 10, 1101 (1962).

17. F. Wilhelm and H. G. F. Wilsdorf, ASD - TDR-62-509, July 1964.

APPENDIX A

GROWTH OF BERYLLIUM SINGLE CRYSTALS

The apparatus used to produce single crystals of beryllium (Spangler et al)[1] is shown in Figure A1. The beryllium bar to be made into a single crystal is gripped by a titanium chuck below a beryllium gettering bar, and the assembly is suspended from a hook at the top of the inner vycor or quartz enclosure tube. The entire assembly is supported at the bottom by a freely moving carriage held in place with a permanent magnet. A pyrex water jacket surrounds the quartz tube. Melting is accomplished in a pure argon atmosphere by induction heating: a narrow molten zone is carried along the bar at a rate of 1/2" per hour by moving the apparatus shown in Figure A1 while the induction coil remains stationary. The direction of travel of the molten zone is from top to bottom to take advantage of gravity segregation, since almost all impurities in beryllium, including BeO, are more dense than beryllium. Directed gas flow is necessary within the loop to maintain visibility of the molten zone. This is achieved in this system by cooling the gas in the down-leg by a dry ice and alcohol mixture.

The system pictured in Figure A1 was evacuated to a pressure of approximately 10^{-6} mm Hg, and filled with argon to slightly less than one atmosphere and hermetically sealed. The argon atmosphere within the glass enclosure was purified by first heating the central titanium chuck to about 900°C, and by then maintaining a molten zone in the beryllium gettering bar. Normally, the orientations of single crystals grown from the melt are such that the (0001) plane is closely parallel with the growth direction. Specific orientations are obtained by mounting a seed single crystal having the desired orientation at the top chuck.

---

[1] G.E. Spangler, M. Herman, and E. J. Arndt, Dept. of Navy, Bureau of Naval Weapons, Contract W61-0221-d(1961).

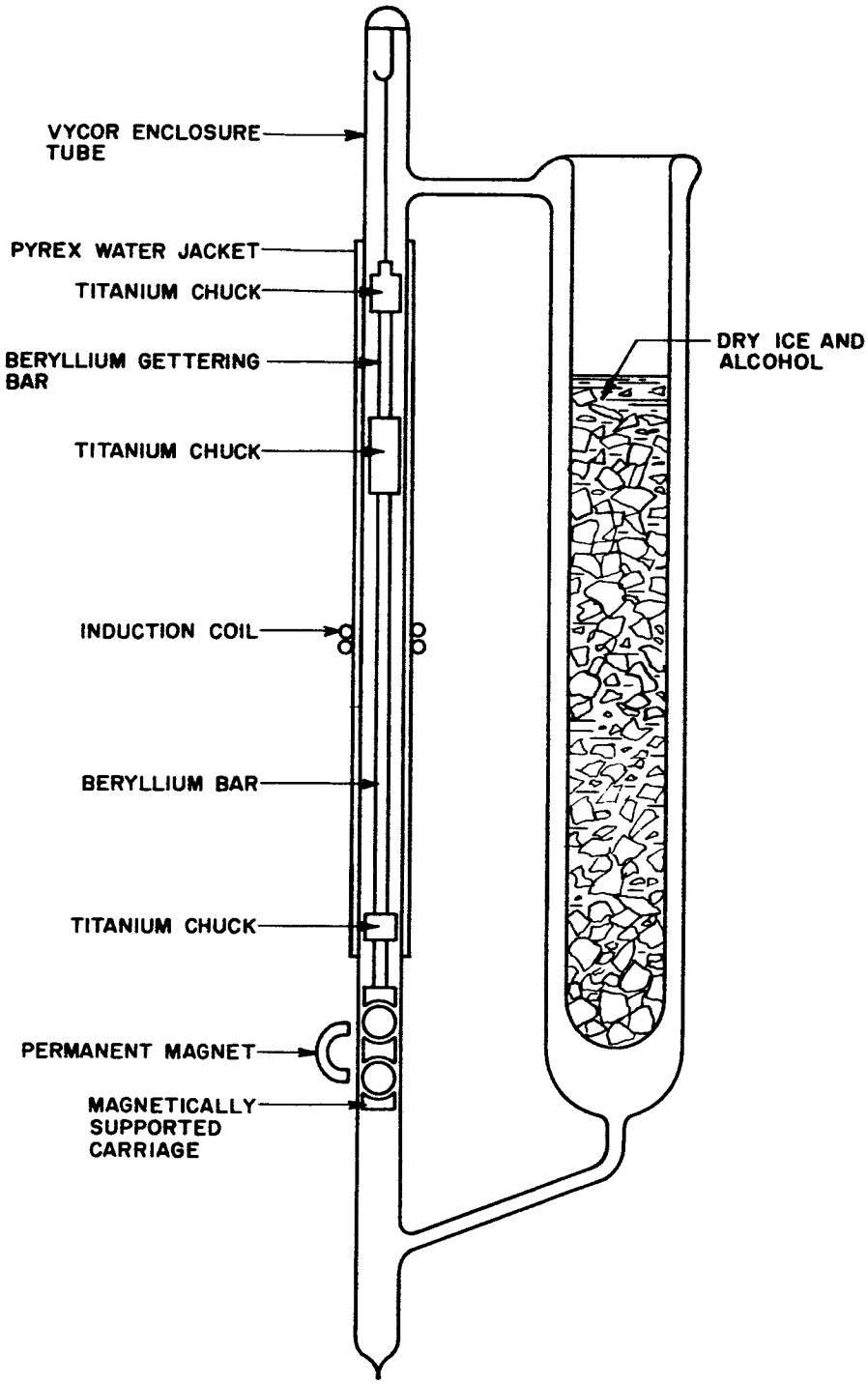

Fig. A1 - Schematic Representation of the Apparatus used to Grow Beryllium Single Crystals by the Vertical Floating-Zone Technique.

APPENDIX B

PREPARATION OF ELECTRON MICROSCOPE SPECIMENS

Thin foils of beryllium suitable for observation in transmission in the electron microscope must contain an area whose thickness is less than 4000Å. The thickness of sections cut by spark machining from polycrystalline and single crystal material was reduced from 0.5 mm by electro-polishing, using the techniques developed by Wilhelm[1], Strutt[2], and Meakin[3]. The Knuth system of electro-polishing[1] is depicted by Figure B1. The specimen is mounted in the plastic shield having a 1 mm diameter central hole. Fresh electrolyte is supplied to the surface being polished by the pump. The specimen is first polished on one side to create an indentation at its center. The specimen is then inverted and electro-polishing is continued until a perforation is observed under low magnification at the base of the depression. The polishing current is turned off and the specimen is removed from the apparatus and washed. The thin area examined in transmission is around the edge of this perforation. The composition of the electro-polishing solution used is:

300 g Cupric nitrate
900 ml Methanol
30 ml Nitric acid

Either a copper or stainless steel cathode is used at 50 volts potential.

More recently, an electrolyte consisting of 50 parts ethylene glycol, 5 parts concentrated nitric acid, 1 part concentrated sulphuric acid, and 1 part concentrated hydrochloric acid has been used. This results in a shorter preparation time, and it is not necessary to use the Knuth arrangement. Details of the mode of electrothinning are given by Strutt[2] and Meakin[3].

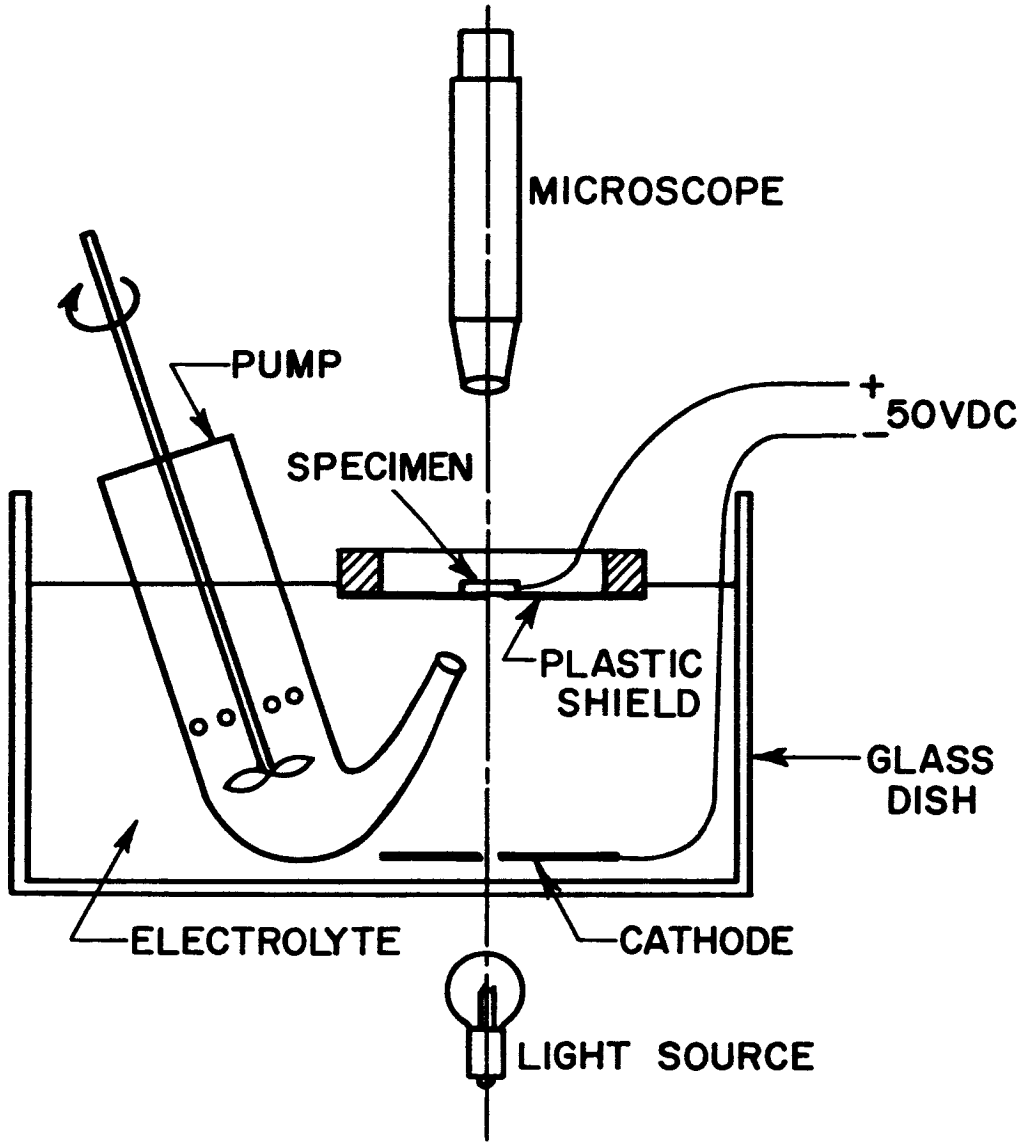

ELECTROPOLISHING APPARATUS

Fig. B1 - Schematic Representation of the Knuth System of Electro-polishing for Beryllium

REFERENCES

1. F. J. Wilhelm, J. Sci. Inst. 41, 343 (1964)

2. P. R. Strutt, Rev. Sci. Inst. 32, 411 (1961)

3. J. D. Meakin, Rev. Sci. Inst. 35, 763 (1964)

APPENDIX C

HIGH RESOLUTION DARK FIELD MICROSCOPY USING A PHILIPS 100B ELECTRON MICROSCOPE*

ABSTRACT

A simple modification to a Philips 100B electron microscope makes possible the production of dark field images without any loss of resolution. The method utilizes electrical tilting of the primary beam and permits rapid alteration between bright and dark field viewing.

INTRODUCTION

The full application of the kinematic and dynamic theories of electron diffraction to thin foil microscopy is only possible if high resolution dark field micrographs are available. Dark field imaging without loss of resolution is accomplished[1] by inclining the illuminating beam so that a particular transmitted diffracted beam is parallel to the optical axis of the microscope. Dark field images can be produced by displacing the objective aperture but the image quality is poor due to the aberations produced by using off-axis beams.

The Philips 100 series microscopes contain a focusing aid known as a "wobbler". This unit consists of a pair of coils located immediately behind the back objective pole piece. The coil nearest to the electron source bends the beam away from the optic axis and the second coil deflects the beam back onto the specimen thus providing an inclined illuminating beam. When used as a wobbler the coils are activated by an A.C. current and so the specimen is viewed using an oscillating beam. Clearly a restricted amount of dark field operation would be possible by merely rectifying the supply to the wobbler coils. To be able to produce a dark field image from any given diffracted beam however, it must be possible to select as tilt axis any direction perpendicular to the optic axis. This is accomplished by having two sets of tilt coils mounted at right angles in place of the uniaxial wobbler coils.

*The high resolution dark field device was designed and constructed by J. D. Meakin and L. Cinquina, published in Rev. Sci. Inst. 36, 654, 1965.

CONSTRUCTION

The wobbler coils are outside the vacuum and are mounted on a plastic former which slides inside the rear section of the objective lens. Access to the coils is gained by splitting the column between the gun chamber and the condenser lens. A new former for the tilt coils was machined from brass as it was thought desirable to improve the heat dissipation from the windings. The critical dimensions of the former are as shown in Figure C-1a. Each coil consists of two poles located on opposite sides of the electron beam and these were wound with #35 formvar coated wire as shown in Figure C-1b. The former and completed windings were lacquered with transformer dope to minimize the risk of grounding the wires to the brass. It was determined that the coils nearest to the specimen need to be stronger than the leading coils and the coils were therefore wound with 110 and 70 turns/pole respectively.

The completed former is inserted into the microscope and the necessary electrical connections made to the terminal block located underneath the condenser lens. There is ample room to add the extra two terminal points required. It is particularly convenient when using the attachment if the coils cause the center spot to remove along horizontal and vertical directions on the viewing screen. With the 100B microscope set to image the diffraction pattern there is a net 30° clockwise rotation between the specimen plane and the screen. By positioning the axis of one set of coils 30° anticlockwise from the vertical axis, as seen by the operator, the apparent axes of the tilt are vertical and horizontal as desired.

The resistance of each coil is about 5 ohms and the maximum current necessary to produce tilts of about 6° is 1 amp/coil. Various power supplies were tried and the most satisfactory proved to be a highly filtered transisterized D.C. supply. The supply and associated switching is shown in Figure C-2. The amount of tilt is fixed by R_1 and R_2 which control the voltage applied to the coils. The beam is made to impinge on the visible region of the specimen by adjusting the relative strength of the leading and following coils using the potentiometer R_3 and R_4. Resistances R_5 and R_6 permit critical adjustment of the illumination particularly when

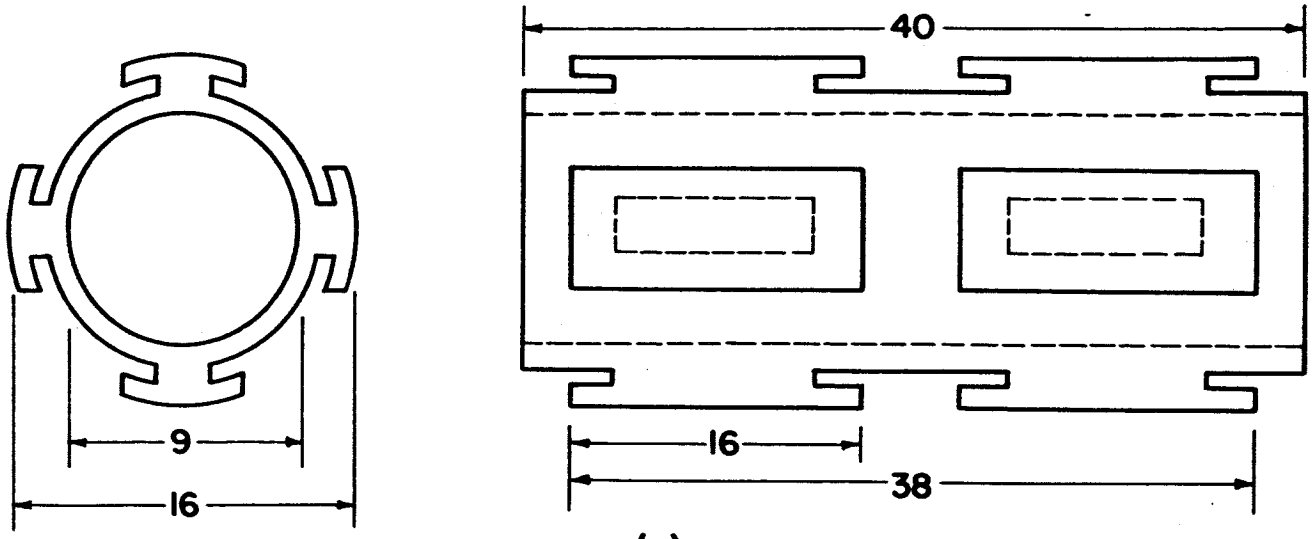

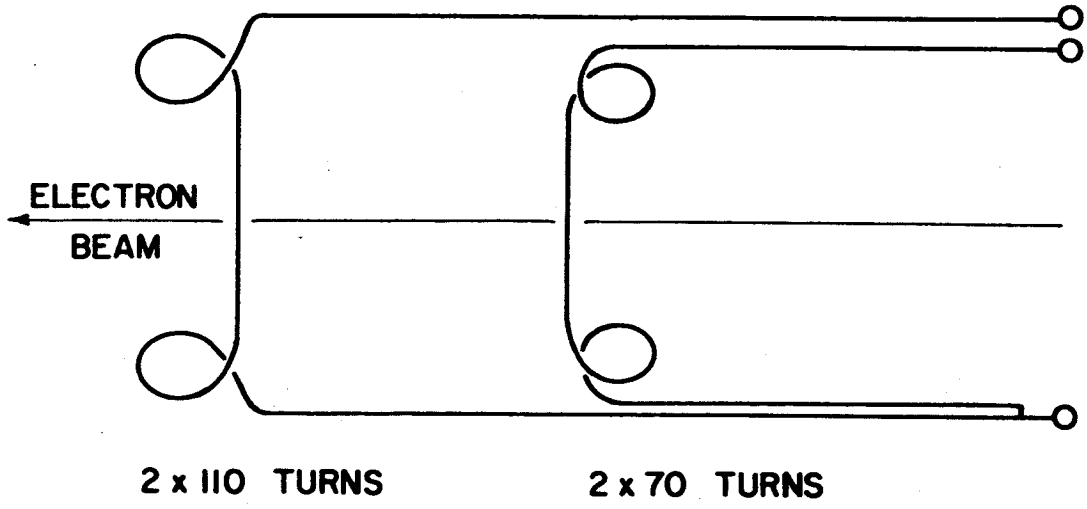

Fig. C-1 - (a) Construction of Brass Former for Tilt Coils. Dimensions in Millimeters. (b) Winding for Vertical or Horizontal Coils.

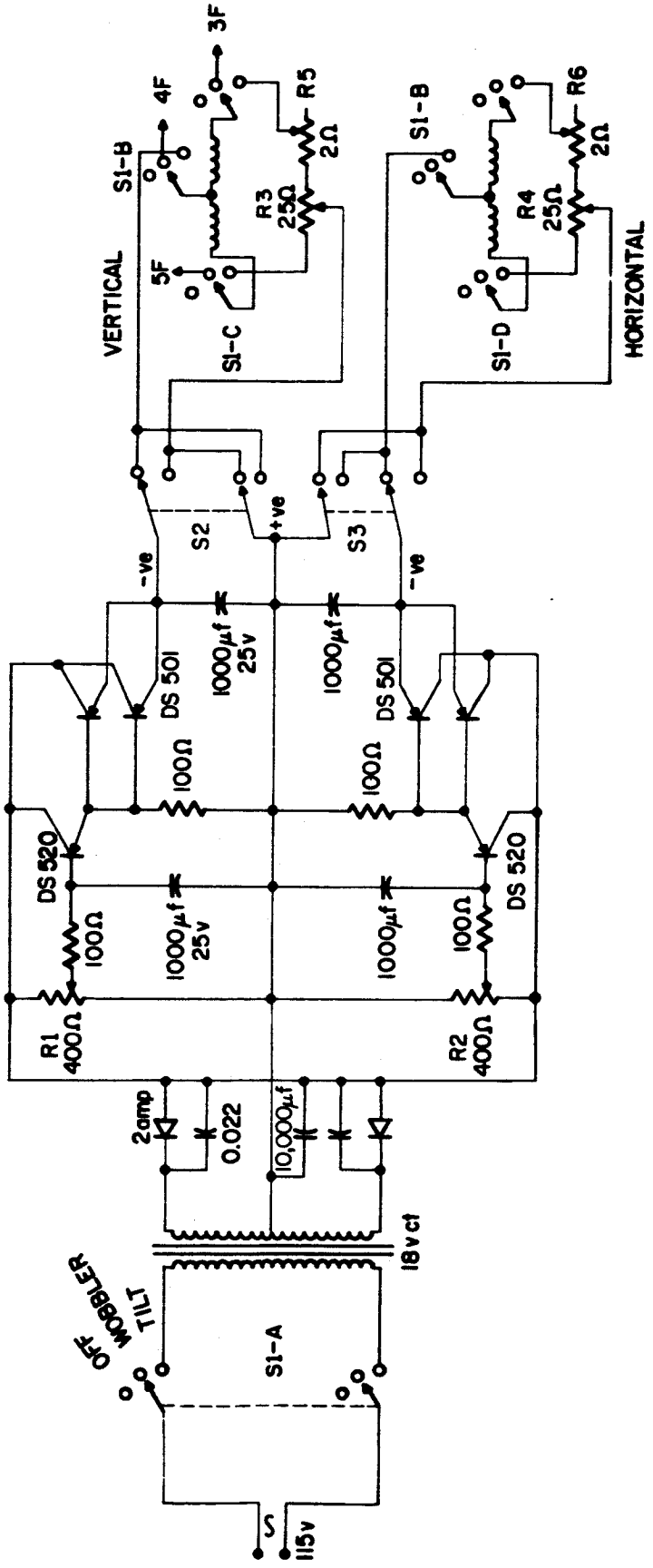

Fig. C-2 - Wiring Diagram for Power Supply and Tilt Coils

working with the minimum diameter beam. The reversing switches S_2 and S_3 enable the sense of the beam tilt to be changed. Finally it should be noted that the wobbler is still available to aid in focusing. With the selector switch in position 2, one set of coils is connected to the wobbler power supply through the terminals 3, 4 and 5 in the 'F' plug. This is the standard position for S_1 when using the microscope for bright field work.

OPERATION

The microscope is assumed to be aligned for bright field viewing with the intermediate lens set for imaging the diffraction pattern. A particular diffraction spot, g, is selected for providing the dark field image. The conversion to dark field operation is now rapidly accomplished as follows:

1) Withdraw the objective aperture. Note location of the center spot on the screen. Set the condenser lens for low intensity and turn the beam tilt controls R_1 and R_2 to minimum position. Set R_3 and R_4 at an approximately mid-point position.

2) Turn on tilt power supply using S_1. Increase beam tilt controls, R_1 and R_2, until spot g has moved to original center spot position. If necessary reverse direction of tilt using S_2 and/or S_3. Maintain uniform illumination of the screen using R_3 and R_4. Do not adjust the beam using the normal beam alignment controls. Note: as the primary beam is tilted the intensity of the diffraction spot g may diminish. To maintain the specimen in the Bragg condition it is necessary to tilt both the specimen and the beam around the same axis. In general a two axis goniometer stage will be required to accomplish this.

3) To achieve critical alignment - switch off the tilt power using S_1. Replace the objective aperture and accurately align it with respect to the center spot. Switch on the tilt supply and allow a few seconds to stabilize. Accurately center the spot 'g' in the objective aperture using the tilt controls. Gradually bring the condenser lens to cross-over while maintaining equal illumination using the balance controls. If necessary

adjust the tilt to keep 'g' centered. The microscope can now be operated at any magnification to give a dark field image using the selected diffraction condition.

As dark field is achieved using entirely electrical means the instrument can be instantly restored to bright field viewing and there is no associated shift in the area imaged when making the change. This is of particular benefit when working at high magnifications. Once the tilt and balance controls have been set for a particular diffraction spot, it is possible to alternate between bright and dark field viewing with a few seconds delay and only the most minor adjustments of the balance controls. The angle of tilt available is about 6°. This amount of tilt, for instance, permits dark field viewing using the first eight orders of diffraction from molybdenum.

finally it is worth noting a specific relation between the bright and dark field image produced by the device described. In general dark field images will be produced with the specimen exactly in the Bragg condition as the diffracted intensity is then a maximum. For this condition the primary beam is inclined by 2θ and the diffracting planes by θ to the optic axis, where θ is the Bragg angle. Call this operating reflection $+g$. If the beam tilt is now switched off and the specimen not rotated the primary beam now makes an angle $-\theta$ to the diffracting planes, i.e., the operating condition can now be characterized by $-g$. A dark field-bright field pair of micrographs can thus readily and quickly be obtained even at very high magnifications. Interpretation of any contrast effects must of course take note of the change in sign of the operating reflection when going from bright to dark field. Our experience with this device is confined to a Philips 100B microscope but it seems very likely that a similar conversion could be readily accomplished with the more refined Philips EM-200 which also contains the wobbler focusing system.

An example of the capability of the device is given in Figure C-3 which shows stacking faults in stainless steel photographed in (a) bright-field and (b) dark-field.

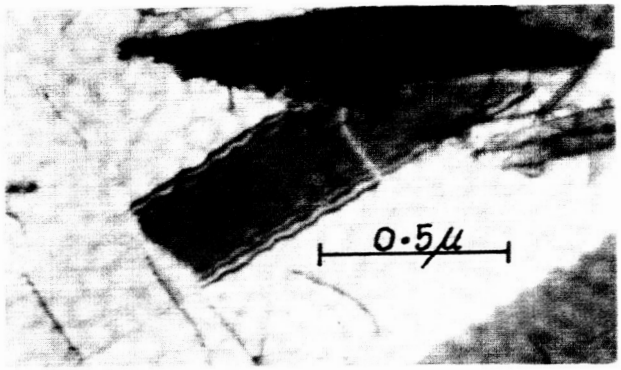

(a)

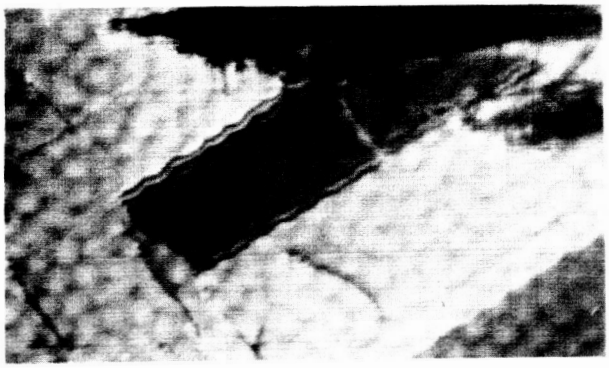

(b)

Fig. C-3 - Stacking Faults in Stainless Steel. (a) Bright Field. (b) Dark Field. Original Magnification x 40,000.

REFERENCE

1. D. Kay, Techniques for Electron Microscopy, p. 24, Blackwell (1961).

APPENDIX D

THE EFFECT OF CONCURRENT AND INDEPENDENT YIELDING MECHANISMS ON ANELASTIC BEHAVIOR*

In calculating the friction stress from a plot of loop area against forward plastic strain, the theory requires that extrapolation of the best line fit at low strains ($\lesssim 5 \times 10^{-5}$) passes through the origin. The analysis presented here shows that a high measured value of the friction stress and a positive intercept on the strain amplitude plot are related.

Suppose that there are two independent yielding mechanisms controlled by frictional stresses τ_1 and τ_2 where $\tau_2 > \tau_1$. The motion of pre-existing edges and screws would serve as a plausible example. Hysteresis loops generated in the stress interval $2\tau_1 < \tau < 2\tau_2$ lead to an energy-plastic strain plot that extrapolates through the origin. If the stress $2\tau_2$ is exceeded, then energy dissipation takes place against τ_2 as well as τ_1. The situation is illustrated in Figure D-1; it is of course likely that dissipation against τ_1 will continue at the higher stresses so that the energy balance during the forward (or reverse) half cycle is given by:

$$\Delta W/2 = \tau_1 \gamma_1 + \tau_2 \gamma_2 \qquad \text{(D-1)}$$

γ_1 is the plastic strain contribution from the first process which, as stated, is assumed to be independent of the plastic strain γ_2 from the second process. For simplicity in this model we assume linear hardening of slope m_1 between $2\tau_1$ and $2\tau_2$, and slope m_2 at stresses above $2\tau_2$. The strain contribution of the first process is taken to be controlled by m_1 at stresses $> 2\tau_1$, where $m_1 > m_2$.

*This analysis forms part of a communication prepared by A. Lawley and J. D. Meakin, which has been accepted for publication in Acta Metallurgica.

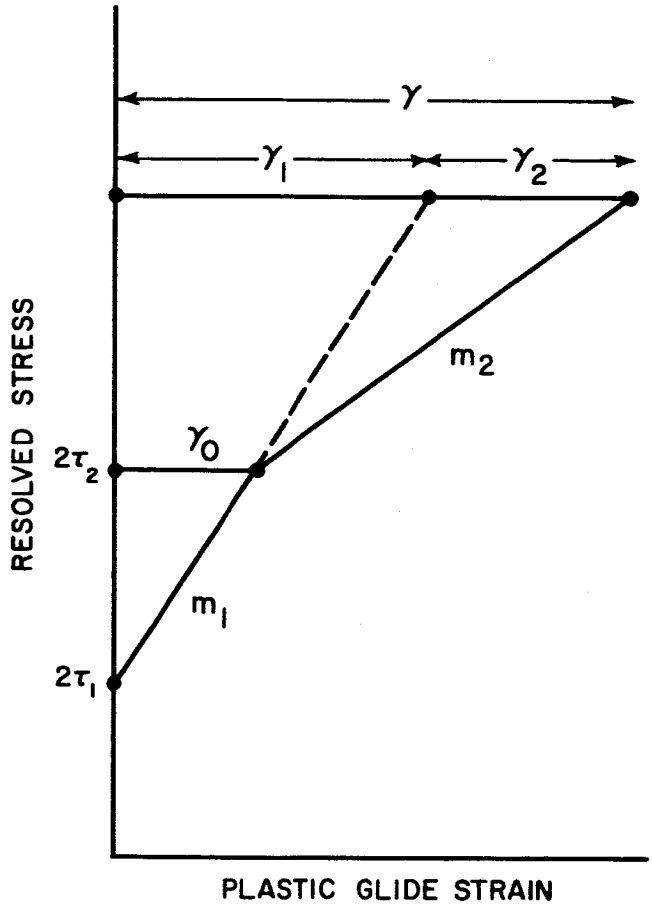

Fig. D-1 - Schematic Representation of Two Independent Yielding Mechanisms Controlled by Frictional Stresses τ_1 and τ_2.

Under these conditions:

$$\frac{\gamma_1 + \gamma_2 - \gamma_o}{\gamma_1 - \gamma_o} = \frac{m_1}{m_2} = \frac{1}{\alpha} > 1 \qquad \text{(D-2)}$$

$$\gamma = \gamma_1 + \gamma_2 \qquad \text{(D-3)}$$

$$\gamma_1 = \gamma_o + \alpha\,(\gamma - \gamma_o) \qquad \text{(D-4)}$$

$$\gamma_o = 2\,(\tau_2 - \tau_1)/m_1 \qquad \text{(D-5)}$$

Equation (D-1) can be written:

$$\Delta W/2 = \{\tau_2 - \alpha\,(\tau_2 - \tau_1)\}\,\gamma - (1 - \alpha)\,(\tau_2 - \tau_1)\,\gamma_o \qquad \text{(D-6)}$$

or $$\Delta W/2 = \{\tau_2 - \alpha\,(\tau_2 - \tau_1)\}\,\gamma - (2/m_1)\,(1 - \alpha)\,(\tau_2 - \tau_1)^2 \qquad \text{(D-7)}$$

A positive intercept on the strain axis, and the correspondingly higher friction stress, can now be seen to be the result of the onset of a second plastic flow process. From Equation (D-7), the experimentally determined friction stress will always be less than τ_2 and, depending on the value of α, could be near to either τ_1 or τ_2. If α is small, there is a significant change in strain hardening when the second process is initiated; under these conditions, reasonable estimates of τ_2 should be obtained experimentally. Note that for a single process, $\alpha = 1$ and Equation (D-7) reduces to

$$\Delta W = 2\tau_f\,\gamma_p \qquad \text{(D-8)}$$